Interannual Variability and Long-term Change of Global Ozone Distribution: Roles of Transport and Chemical Processes

(全球オゾン分布の年々変動と長期変化： 輸送・化学過程の役割)

SEKIYA, Takashi

(関谷　高志)

Doctor of Science

Department of Earth and Environmental Sciences

Graduate School of Environmental Studies, Nagoya University

（名古屋大学　大学院環境学研究科　地球環境科学専攻　博士（理学））

2014

要旨

オゾンは、大気環境、気候にとって重要な大気微量成分のひとつであり、その変化は大気中の複雑な輸送、化学過程によって引き起こされている。オゾン変化に対する輸送、化学過程の寄与は、日周変化や季節変化、成層圏の年々変動については、先行研究によって定量的に調査されてきた。しかし、対流圏オゾンの年々変動、成層圏・対流圏オゾンの長期変化に対する輸送、化学過程の寄与については、ほとんど調査されてこなかった。そこで本研究では、（1） 1970 年から 2008 年までの気象場変動に伴う全球対流圏オゾンの年々変動、（2）2000 年代から 2100 年代の全球オゾンの長期変化における、輸送、化学過程の寄与を調べた。

まず、気象場変動に伴う対流圏オゾンの年々変動と、それに対する輸送、化学過程の寄与を調査した。気象場変動として、エルニーニョ南方振動（El Niño Southern Oscillation; ENSO）、インド洋ダイポール（Indian Ocean Dipole; IOD）変動、ハドレー循環の年々変動、アジアモンスーン循環の年々変動、北極振動（Arctic Oscillation; AO）の 5 つに着目した。本研究では、全球化学輸送モデル CHASER による、1970 年から 2008 年までの 39 年間の過去再現シミュレーションを解析した。シミュレーション中の気象場は、NCEP/NCAR 再解析データに緩和（ナッジング）させることにより、気象場の年々変動を再現した。10 月から 12 月の全球対流圏カラムオゾン（Tropospheric Column Ozone; TCO）分布に対して経験的直交関数（EOF）解析を行った結果、ENSO に伴う変動成分が最も支配的であり、その成分は全分散の 33% に寄与していた。領域スケールでは、他の 4 つの気象場変動も無視できない影響を与えていた。特に、AO に伴う TCO 変動は、北半球高緯度域における 12 月から 2 月の TCO 変動の分散に対して 72% 寄与していた。また、IOD 変動に伴う TCO 変動も、アフリカ・西インド洋域における 10 月から 12 月の TCO 変動に対し 36% 寄与していた。これらの TCO の年々変動は、亜熱帯域、北半球高緯度域では、輸送過程に大きく影響されていた。しかし、熱帯域の東太平洋、西インド洋においては、化学過程も TCO の年々変動に寄与していた。化学過程による TCO の変動は、主に気象場変動に伴う気温、水蒸気、雲、雷の変動の複合的な影響によって、引き起こされたと考えられる。

次に、全球オゾンの将来変化について調査する前に、将来予測に用いる化学気候モデルの検証のため、ENSO に伴うオゾン変化、1980 年代から 2000 年代までのオゾン変化の再現性を評価した。全球化学気候モデルは気象場をモデル内で計算するため、モデル内の気象場の変動に伴うオゾンの変動を検証する必要がある。そこで、化学輸送モデルによる解析において、全球 TCO 分布への影響が最大であった ENSO を対象に、化学気候モデルの検証を行った。2004 年から 2009 年までの ENSO に伴う成層圏・対流圏オゾンの変動について、観測データと化学気候モデルによる再現実験を比較した結果、モデルは観測されたオゾン変動を概ね再現していた。さらに、オゾン前駆物質、オゾン破壊物質の排出量の変化に伴う、オゾン分

布の変化の再現性を評価した。評価は、排出量の変化が大きい 1980 年代から 2000 年代までのオゾンの変化を対象に行った。その結果、モデルは、衛星観測と同様、総カラムオゾンの減少（全球・年平均値：−0.47±0.16％/10 年）を計算した。しかし、モデルの結果は、観測された減少（−1.27±0.60％/10 年）を過小評価していた。

最後に、2000 年代から 2100 年代までの全球オゾンの将来変化と、それに対する輸送、化学過程の影響を調べた。将来の境界条件には、IPCC 第５次評価報告書に向けて提供された、中間的なシナリオのひとつ（RCP6）を用いた。モデルによる将来変化予測は、全球成層圏オゾン総量の増加（0.24±0.01％/10 年）、全球対流圏オゾン総量の減少（−0.82±0.04％/10 年）を予測した。成層圏オゾンの変化は、輸送過程（ブリューワードブソン循環の強化）より化学過程に影響されていた。化学過程による成層圏オゾンの変化については、気温の低下、オゾン破壊物質の排出量の減少の複合影響と考えられる。対流圏においても、化学過程が大きく全球対流圏オゾン総量を減少させる（−1.07％/10 年）。しかし、輸送過程（成層圏–対流圏間交換の増加と対流圏大気循環の変化）による総量の増加も無視できない（0.25％/10 年）。化学過程による対流圏オゾンの変化には、気温の上昇、水蒸気の増加、雲・雷の変化、オゾン前駆物質の排出量の減少が複合的に影響していると考えられる。また、輸送過程による増加については、対流圏起源オゾン、成層圏起源オゾンの両方が寄与していた。これは、対流圏オゾンの将来変化にとっては、成層圏–対流圏間交換の増加だけでなく、対流圏の大気循環の変化も重要であることを示唆している。

以上のように、本研究は数年から百年までの時間スケールのオゾン変化における輸送、化学過程の役割を定量的に調べた。対流圏オゾン分布の年々変動については、全球スケールでは ENSO に伴う変動が支配的であるが、領域スケールでは IOD 変動、AO の影響も無視できなかった。さらに、それらの変動に対しては、熱帯域の東太平洋、西インド洋では輸送・化学過程の両方が寄与していたが、亜熱帯、北半球高緯度域では輸送過程の影響が大きかった。成層圏・対流圏オゾンの将来変化に関しては、化学過程の影響が大きかった。しかし、対流圏オゾンの将来変化に対しては、輸送過程が無視できない影響を与えていた。

Abstract

Ozone is one of important atmospheric constituents for atmospheric environment and climate. Changes in ozone are caused by a combination of complex atmospheric transport and chemical processes. A number of previous studies investigated the individual contributions of transport and chemistry to the diurnal and seasonal cycles of ozone quantitatively, and examined the contributions to the interannual variation in stratospheric ozone. However, the contributions to the long-term changes in stratospheric and tropospheric ozone were hardly examined. This dissertation investigates the respective impacts of transport and chemical processes on (1) interannual variation in tropospheric ozone associated with meteorological variability during 1970–2008, (2) long-term changes in global ozone during the 2000s and 2100s.

We investigate interannual variations in global tropospheric ozone associated with five types of meteorological variability: El Niño Southern Oscillation (ENSO), Indian Ocean Dipole (IOD) variability, interannual variation in Hadley circulation, interannual variation in Asian monsoon circulation, and Arctic Oscillation (AO). We also examine respective impacts of transport and chemical processes on them. In this chapter, we performed the simulation for 39 years from 1970 to 2008 using CHASER global chemical transport model (CTM), in which meteorology was nudged to NCEP/NCAR re-analysis data.

The Empirical Orthogonal Function (EOF) analysis suggests that ENSO is a dominant mode of the variation in global TCO distribution (the contribution rate: 33%) in October–November–December (OND). On regional scale, the other meteorological variability also has non-negligible impacts. AO explains 72% of the variance of TCO in the high northern latitudes in December–January–February (DJF). IOD variability explains 36% of the variance in the equatorial Africa and the western Indian Ocean in OND. The interannual variations of TCO are significantly controlled by transport process in the subtropics and the high northern latitudes. However, both transport and chemical processes contribute to the TCO interannual variation in the eastern Pacific and the western Indian Ocean over the tropics. TCO variation because of chemical process could be caused by variations in temperature, water vapor, cloud, and lightning associated with meteorological variability.

Before investigating the future change in global ozone during the 2000s and 2100s, we evaluate the ENSO-related ozone variation and the ozone change for the 1980s and 2000s in the MIROC-ESM-CHEM global chemistry–climate model (CCM). Because CCM calculates meteorological and chemical fields, we focus on the ENSO-related variation to validate the ozone response to CCM-driven meteorological variability. The model generally reproduces the observed ENSO-

related variation of ozone distribution derived from satellite instruments. Additionally, we focus on the change during the 1980s and 2000s to evaluate the ozone response to a change in the emissions of tropospheric ozone precursors and ozone-depleting substances (ODSs). The model simulates a decrease in global and annual mean of total column ozone (about $-0.47\pm0.16\%$/decade) during the 1980s and 2000s, although the model underestimates the observed decrease ($-1.27\pm0.60\%$/decade).

We investigate the individual impacts of transport and chemical processes on the future long-term change in global ozone during the 2000s and 2100s which mean ????. We assumed one of the medium stabilization emission scenarios for IPCC fifth assessment report (RCP6) in 2100 as the boundary conditions for the 2100s. Global simulation of ozone concentration for the 2100s predicts an increase in global stratospheric ozone burden ($0.24\pm0.01\%$/decade), and a decrease in global tropospheric ozone burden ($-0.82\pm0.04\%$/decade). Chemical process contributes largely to the long-term change in stratospheric ozone. The change in ozone due to chemical process is probably attributed by the temperature decrease and the reduced emission of ODSs. In the troposphere, chemical process largely reduces the global tropospheric ozone burden (-1.07%/decade). Transport process (i.e. stratosphere–troposphere exchange (STE) and tropospheric circulation), however, causes an increase in the burden (0.25%/decade). The decrease in tropospheric ozone due to chemical process could be influenced by the changes in temperature, water vapor, cloud, and lightning as well as the reduced emission of tropospheric ozone precursors. Transport of ozone of both stratospheric and tropospheric origin comparably contributes the increase because of transport, suggesting that not only STE but also tropospheric circulation is important.

This dissertation examines roles of transport and chemical processes in interannual variation and long-term change in global ozone using a global chemistry model. As for interannual variation in tropospheric ozone, we show that ENSO is the most dominant mode of interannual variation in global tropospheric ozone. On regional scale, AO and IOD variability have non-negligible impacts. The model also shows that transport process have a significant impact on the variations in the subtropics and the high northern latitude. Both of transport and chemical processes are important in the tropical eastern Pacific and western Indian Ocean. The future change in tropospheric and stratospheric ozone during the 2000s and 2100s is influenced by chemical process rather than transport process. However, transport process has a non-negligible impact on the future change in tropospheric ozone.

Contents

Chapter 1

Introduction

1.1 Impact of ozone on atmospheric environment and climate

Ozone (O_3) is one of important atmospheric constituents for atmospheric environment and climate. Stratospheric ozone protects living things by absorbing harmful ultraviolet radiation (UV). UV-B (280–315 nm wave length) radiation, which ozone absorbs efficiently, increases the risks of skin cancer, cataract, and suppressed immune system [WMO, 2011]. Results from ground-based reconstruction and satellite retrieval data suggests that UV-B radiation has increased since the late 1970s [WMO, 2011]. Ozone near the surface is harmful for human health and plant. Ozone damages pulmonary and cardiovascular system of human [WHO, 2006]. Surface ozone levels in the 2000s could result in substantial crop production losses [e.g. Avnery et al., 2011].

Ozone in the stratosphere and troposphere is also important for the Earth's radiation budget because ozone absorbs ultraviolet and infrared radiation. Radiative forcing (RF) due to stratospheric ozone change from the pre-industrial era to the present (i.e. radiative forcing) is estimated to be -0.05 ± 0.10 Wm^{-2}, and RF due to tropospheric ozone change is estimated to be 0.40 ± 0.20 Wm^{-2} [Myhre et al., 2014]. Their contribution to global warming during the period is regarded as the third most important, following those of carbon dioxide (CO_2) and methane (CH_4) (Figure 1.1).

Additionally, ozone partly affects changes in tropospheric circulation. Stratospheric ozone changes in the lower stratosphere over the Antarctic plays a crucial role in change of tropospheric jet and associated climate change in the southern hemisphere [e.g. Son et al., 2008; Kang et al., 2011; Thompson et al., 2012]. Spatially heterogeneous heating attributable to tropospheric ozone and black carbon caused an expansion of the tropics in the northern hemisphere during the last three decades [Allen et al., 2012].

Stratospheric and tropospheric ozone also have an impact on oxidizing capacity of the atmo-

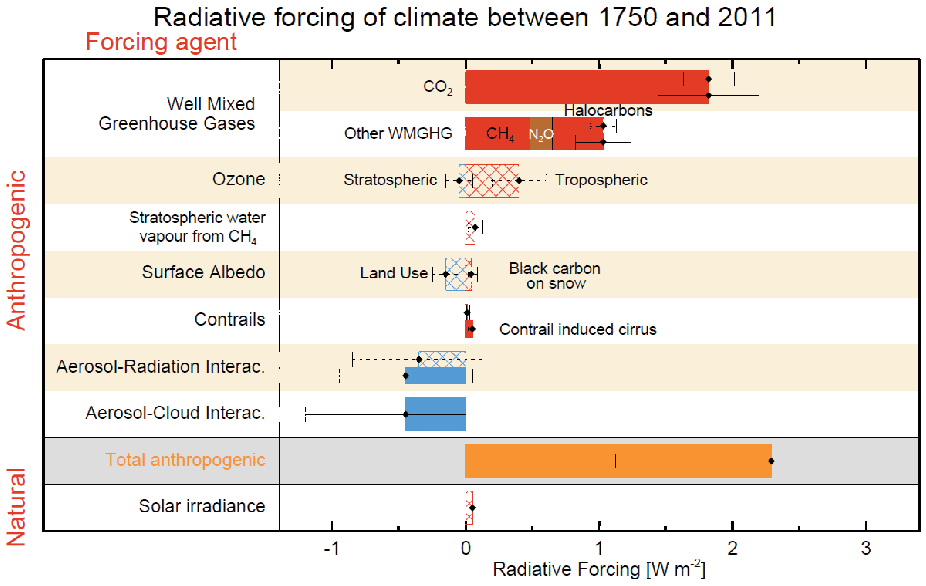

Figure 1.1. Bar chart for Radiative Forcing (RF) and Effective Radiative Forcing (ERF) for the period 1750–2011 taken from Myhre et al. [2014]. Hatched and Solid bars are respectively RF and ERF. Uncertainties (5–95% confidence range) are given for RF (dotted lines) and ERF (solid lines).

sphere, which is represented by hydroxyl radical (OH). Modeling studies [e.g. Naik et al., 2013; Voulgarakis et al., 2013] suggested that OH concentration is influenced by stratospheric ozone, NO_x emission, and CH_4 emission. Change in OH affects the oxidation processes of sulfur dioxide (SO_2) to sulfate (SO_4^{2-}). OH also controls the chemical lifetime of pollutants (NO_x, CO, and NMVOCs) and greenhouse gases (CH_4 and HFCs) other than ozone.

1.2 Chemistry and transport processes related to ozone

As described in section 1.1, ozone has impacts on atmospheric environment and climate. Ozone concentrations are controlled by a combination of complex transport and chemical processes. Near the surface, dry deposition is also important. In this section, we provide an overview of these processes in the stratosphere (1.2.1) and the troposphere (1.2.2).

1.2.1 Stratosphere

Stratospheric ozone is produced by the photo dissociation of oxygen molecule (O_2) and subsequent chemical reaction,

$$O_2 + h\nu \rightarrow O + O \tag{1.1}$$

$$O_2 + O \rightarrow O_3 \tag{1.2}$$

and ozone is lost by the reaction with oxygen atom (O),

$$O_3 + h\nu \rightarrow O_2 + O \tag{1.3}$$

$$O_3 + O \rightarrow 2O_2. \tag{1.4}$$

These chemical reactions are called “Chapman mechanism”. Stratospheric ozone is also lost by cycles with HO_x, NO_x, ClO_x, and BrO_x radicals. For example, a catalytic loss mechanism of ozone involving ClO_x is

$$Cl + O_3 \rightarrow ClO + O_2 \tag{1.5}$$

$$ClO + O \rightarrow Cl + O_2. \tag{1.6}$$

Large loss of ozone over the Antarctic in austral spring was discovered by Farman et al. [1985]. The loss is essentially caused by heterogeneous reactions on ice-like polar stratospheric clouds (PSCs), transforming chlorine and bromine reservoir (e.g. HCl and $ClONO_2$) to reactive chlorine and bromine (e.g. Cl_2, $HOCl$, etc.). Additionally, catalytic cycles of ozone with ClO dimer and ClO–BrO play an important role in ozone destruction over the Antarctic. For example, the cycle with ClO dimer is

$$ClO + ClO + M \rightarrow Cl_2O_2 + M \tag{1.7}$$

$$Cl_2O_2 + h\nu \rightarrow Cl + Cl + O_2 \tag{1.8}$$

$$2\left[Cl + O_3 \rightarrow ClO + O2\right]. \tag{1.9}$$

The greatest production of ozone occurs in the tropical stratosphere because of the most intense sunlight. However, the highest amount of ozone is found in the mid and high latitudes. This results from mean poleward transport of ozone due to the stratospheric meridional circulation (so-called “Brewer–Dobson circulation”). Moreover, eddy transport of ozone is also caused by planetary

wave breaking in the winter hemisphere [Miyazaki and Iwasaki, 2005].

1.2.2 Troposphere

In the troposphere, ozone is produced by cycling NO_x involving the reaction of NO with peroxy radicals (e.g. HO_2 and CH_2O) and the subsequent photo dissociation of NO_2:

$$\mathrm{HO_2 + NO \rightarrow NO_2 + OH} \tag{1.10}$$

$$\mathrm{NO_2} + h\nu \rightarrow \mathrm{NO + O} \tag{1.11}$$

$$\mathrm{O + O_2 + M \rightarrow O_3 + M.} \tag{1.12}$$

The peroxy radicals are produced by the oxidations of carbon monoxide (CO) and volatile organic carbons (VOCs) with OH. A major sink of tropospheric ozone is chemical loss. One of its pathway is photo dissociation of $\mathrm{O_3}$ to $\mathrm{O(^1D)}$ followed by the reaction of $\mathrm{O(^1D)}$ with water vapor:

$$\mathrm{O_3} + h\nu \rightarrow \mathrm{O_2 + O\left(^1D\right)} \tag{1.13}$$

$$\mathrm{O\left(^1D\right) + H_2O \rightarrow 2OH.} \tag{1.14}$$

Ozone loss reactions with OH and $\mathrm{HO_2}$ are also important in clean condition.

Global budget of tropospheric ozone is estimated by a number of global chemistry models [Myhre et al., 2014]. Chemical production is a primary source. The global amount is estimated to be 4877 $\pm$ 853 Tg/year. Another source of tropospheric ozone is transport of ozone from the stratosphere to the troposphere (477 $\pm$ 96 Tg/year). A major sink of tropospheric ozone is chemical loss (4260 $\pm$ 645 Tg/year). Dry deposition is also another sink (1094 $\pm$ 264 Tg/year).

In addition, tropospheric transport plays an important role in determining a spatial distribution of tropospheric ozone, because the average lifetime of tropospheric ozone (23.4 $\pm$ 2.2 days) is comparable to the time scale of transport within the troposphere (several weeks to months on hemispheric scale). For instance, Hadley and Walker circulation can contribute to the formation of wave-one pattern of tropical tropospheric ozone [Wang et al., 2006]. In the northern midlatitudes, inter-boundary and inter-continental transport have an impact on surface ozone distribution [e.g. Sudo and Akimoto, 2007; Fiore et al., 2009; Nagashima et al., 2010].

1.3 Roles of transport and chemistry in global ozone changes

Ozone changes are caused by a combination of complex transport and chemical processes, although it is difficult to quantify respective contributions of the processes from only observation. Therefore, a numerical model is needed to elucidate the contributions to the ozone changes. In this section, we review previous modeling studies which focused on the contributions to the ozone changes.

1.3.1 Diurnal and seasonal scale

In regard to diurnal and seasonal cycles of ozone, the individual contributions of transport and chemical processes were examined using a chemical transport model. For example, Sakazaki et al. [2013] examined the global pattern of diurnal cycle throughout the stratosphere, and the respective impacts of photochemistry and dynamics on it. Li et al. [2008] performed a process analysis for the diurnal behaviors of surface ozone at mountainous sites in Japan and China.

As for the seasonal cycle, transport (Brewer–Dobson circulation and eddy transport) and photochemistry contribute to the seasonal variation of total ozone column [Miyazaki et al., 2005]. Seasonal cycles of surface ozone at mountainous sites in China are caused by insitu photochemical production, transport, and dry deposition [Li et al., 2007].

Overall results of these studies suggested that the respective impacts of transport and chemical processes on the diurnal and seasonal cycles of ozone are non-negligible. However, the relative contributions varied among different regions (e.g. latitude, altitude, polluted/clean condition, etc.).

1.3.2 Interannual scale

In the stratosphere, ozone is known to vary associated with meteorological variability: quasi-biannual oscillation (QBO) [e.g. Baldwin et al., 2001], El Niño Southern Oscillation (ENSO) [e.g. Randel et al., 2009], and wave activity over the polar region [e.g. Randel et al., 2002]. QBO and ENSO have impacts on ozone advection via change in Brewer–Dobson circulation [Jones et al., 1998; Calvo et al., 2010]. QBO-induced variations in NO_y (the total reactive nitrogen reservoir) affects chemical ozone source and sink in the middle stratosphere [e.g. Jones et al., 1998; Baldwin et al., 2001]. The simulation without the variations in NO_y implied that ozone transport is an important forcing term for the QBO-induced ozone variation in the stratosphere [Butchart et al., 2003]. Stratospheric ozone is also influenced by changes in sulfate aerosol from episodic volcanic eruptions [e.g. Randel et al., 1995]. The Pinatubo eruptions in 1991 caused a change in stratospheric

ozone through dynamics and heterogeneous chemistry [Telford et al., 2009; Aquila et al., 2012].

Meteorological variability also plays an essential role in interannual variability of ozone in the troposphere [e.g. Kurokawa et al., 2009; Pozzoli et al., 2011]. In particular, ENSO is a dominant mode with respect to the interannual variation in tropospheric ozone (Figure 1.2) [Peters et al., 2001; Doherty et al., 2006; Hess and Mahowald, 2009]. Key meteorological factors of the variation associated with ENSO are upward–downward motion, enhanced–suppressed convection (transport process), and associated water vapor changes (chemical process) [Sudo and Takahashi, 2001]. Arctic Oscillation (AO) also affects tropospheric ozone over North America and Europe in boreal spring [Lamarque and Hess, 2004; Creilson et al., 2005; Hess and Lamarque, 2007].

Additionally, Natural source of tropospheric ozone precursors (e.g. lightning, wildfire, and soil) is also important factor affecting the interannual variation in tropospheric ozone through chemical process [e.g. Hudman et al., 2010; Murray et al., 2013]. Some of changes in the natural emissions could be linked to ENSO [e.g. Nassar et al., 2009].

The previous studies show the individual impacts of transport and chemical processes on the interannual variation in stratospheric ozone quantitatively. However, the impacts on the interannual variation in tropospheric ozone are unclear. Additionally, an impact of other meteorological variability on tropospheric ozone have been examined hardly.

1.3.3 Decadal and centurial scale

On a longer time scale (i.e. decadal and centurial scale), human activity play an important role in global ozone changes. In the stratosphere, ozone is depleted for the last three decades (Figure 1.3a) [e.g. Randel and Wu, 2007]. For the next century, future projections show a recovery of stratospheric ozone except in the tropical lower stratosphere, where ozone decrease is expected to continue (Figure 1.3b) [e.g. Cionni et al., 2011]. The depletion and recovery of stratospheric ozone are primarily caused by changes in chemical ozone loss with chlorine and bromine released from ozone depleting substances (ODSs) [e.g. Gillett et al., 2011; Eyring et al., 2010b]. Climate change can also have a significant impact on the future change in stratospheric ozone. For example, lower temperature prevents the chemical ozone destruction of O_3 and O, and an intensified stratospheric meridional circulation (i.e. Brewer–Dobson circulation) enhances transport of ozone from the tropics to the extratropics [e.g. Li et al., 2009; Eyring et al., 2010b]. N_2O and CH_4 have an impact not only on climate but also on stratospheric chemistry [Ravishankara et al., 2009; Revell et al., 2012].

In the troposphere, ozone concentration was raised during the period from the pre-industrial era to the present, and is expected to decline for the next century (Figure 1.3) [e.g. Cionni et al., 2011;

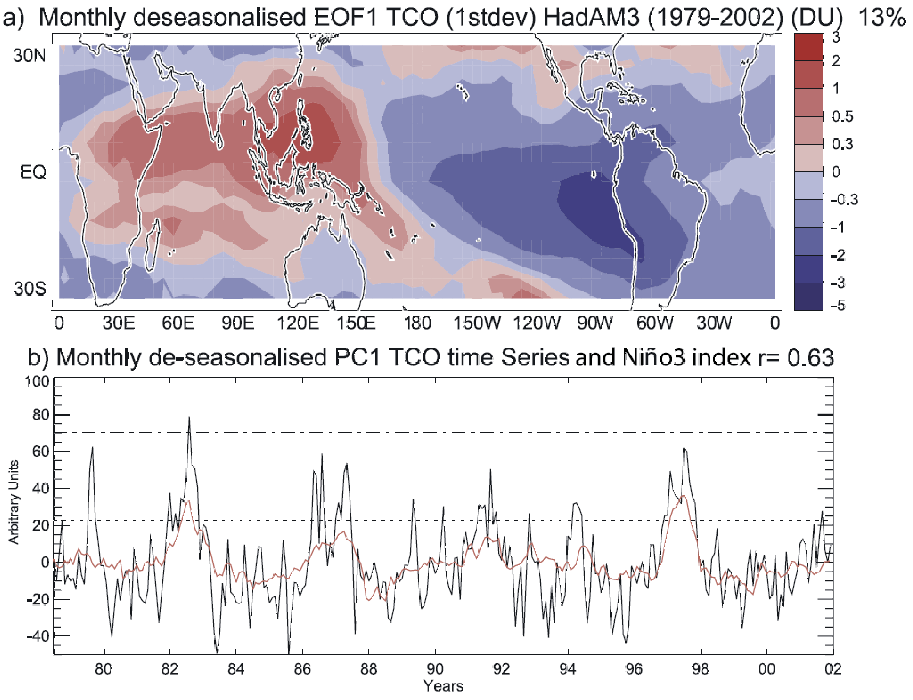

Figure 1.2. Monthly deseasonalized (a) empirical orthogonal function first mode (EOF1) coefficients of tropospheric column ozone (TCO); (b) first mode principal component (PC1) time series of TCO (black) and scaled Niño3 index(red), with +1 standard deviation indicated by dotted line and peak value indicated by dot-dashed line. EOF1 coefficients are scaled by +1 standard deviation of the PC1 time series. These figures were taken from Doherty et al. [2006].

Young et al., 2013]. The chemical ozone production from tropospheric ozone precursors (NO_x, CO, VOCs) [Fusco and Logan, 2003; Stevenson et al., 2013] and CH_4 [e.g. Fiore et al., 2008; Lang et al., 2012] is considered as a major process of the change in tropospheric ozone. Climate change is also expected to alter future change in tropospheric ozone. Higher water vapor facilitates the chemical destruction of ozone with water vapor [Johnson et al., 2001]. Higher temperature stimulates the decomposition of a nitrogen reservoir (per acetyl nitrate; PAN) into NO_x, which produces ozone through chemical reactions [e.g. Doherty et al., 2013]. Moreover, the intensified stratospheric meridional circulation is expected to enhance tropospheric ozone through stratosphere–troposphere exchange (STE) of ozone [e.g. Collins et al., 2003; Sudo et al., 2003; Zeng and Pyle, 2003].

The previous studies examined the individual impacts of external forcing (i.e. ODSs, greenhouse gases, tropospheric ozone precursors) on the long-term ozone changes. However, no research has performed a process analysis for stratospheric and tropospheric ozone changes quantitatively.

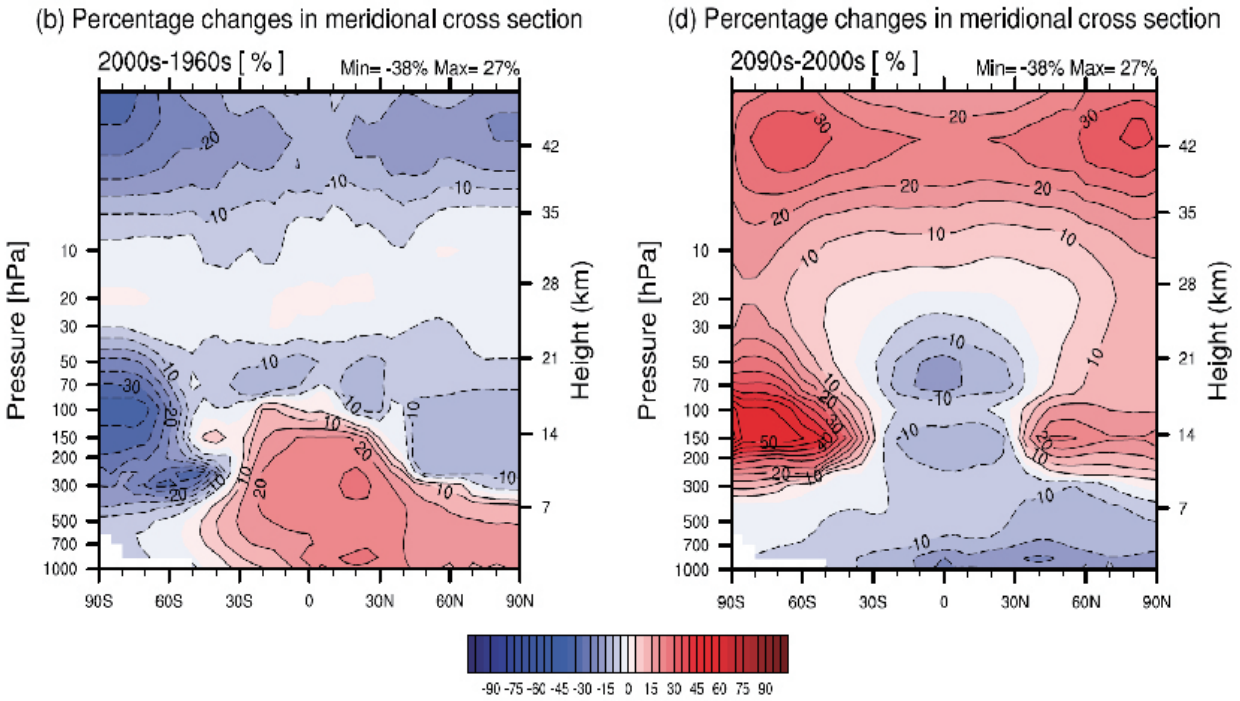

Figure 1.3. Meridional cross-section of the percentage differences in ozone between the 1960s and 2000s (left) and between the 2000s and 2090s (right) taken from Cionni et al. [2011].

1.3.4 Objective

The previous studies investigated the individual contributions of transport and chemistry to the diurnal and seasonal cycles of ozone quantitatively (section 1.3.1), and examined the contributions to the interannual variation in stratospheric ozone (section 1.3.2). However, the contributions to the long-term changes in stratospheric and tropospheric ozone were hardly examined (section 1.3.2 and 1.3.3). This dissertation investigates the respective impacts of transport and chemical processes on the interannual variation in tropospheric ozone and the long-term change in stratospheric and tropospheric ozone. We particularly focus on the following:

(1) Interannual variation of global tropospheric ozone during 1970–2008,

(2) Long-term future change in global ozone during the 2000s and 2100s.

In the first part of this dissertation, we examine interannual variation of tropospheric ozone during 1970–2008 in the simulation with CHASER global chemical transport model (CTM). This CTM is driven by NCEP/NCAR re-analysis meteorology and simulates tropospheric ozone and related species in this study. We focus on the interannual variation associated with five meteorological variability: ENSO, Indian Ocean Dipole (IOD) variability, interannual variation of Hadley circulation, interannual variation of Asian monsoon circulation, and AO. However, this dissertation

does not investigate the impacts of natural source, because we focus on the meteorological impacts apart from the impacts of natural source.

In the second part, we examine the respective impacts of transport and chemical processes on long-term changes in stratospheric and tropospheric ozone during the 2000s and 2100s. This study used a MIROC-ESM-CHEM chemistry–climate model (CCM) to simulates meteorology, ozone, and related species in the troposphere and stratosphere. We assumed one of the medium stabilization scenarios for the IPCC fifth assessment report (RCP6) as a future scenario in the next century [Masui et al., 2011]. Before investigating the future changes, we evaluate the interannual variation and decadal change in stratospheric and tropospheric ozone in the CCM. This study validates the ozone response to meteorological variability related to ENSO during 2004–2009. We also evaluate the ozone response to the change in anthropogenic emissions of tropospheric ozone precursors, ODSs, and greenhouse gases during the 1980s and 2000s.

The dissertation is organized follows. Chapter 2 describes a CHASER global CTM and a MIROC-ESM-CHEM global CCM. Chapter 3 targets the interannual variation in tropospheric ozone associated with the five meteorological variability. In chapter 4, we evaluate the ENSO-related ozone variation and the change in ozone during the 1980s and 2000s in the CCM, before investigating the future change in ozone. Chapter 5 focused on the long-term future change in global ozone during the 2000s and 2100s. Chapter 6 summarizes the overall results of this dissertation, and presents our conclusion and remaining problems.

Chapter 2

Global chemistry model

In this study, we used two different global chemistry models for investigating (1) interannual variation of tropospheric ozone during 1970–2008 and (2) long-term ozone changes during the 2000s and 2100s, respectively. One is CHASER version 3 (CHASER-V3) global chemical transport model, which calculates tropospheric chemistry and related processes. In chapter 3, the simulated meteorology is nudged to NCEP/NCAR re-analysis (see section 3.2). Another is MIROC-ESM-CHEM global chemistry–climate model (CCM). To simulate future ozone changes in the troposphere and stratosphere, the model resolves stratosphere, and includes tropospheric and stratospheric chemistry.

2.1 Global chemical transport model

We employ the CHASER-V3 global CTM [Sudo et al., 2002], which was developed in the framework of the Center of Climate System Research (CCSR)/ National Institute of Environmental Studies (NIES)/ Frontier Research Center of Global Change (FRCGC) AGCM version 5.7 [K-1 model developers, 2004; Nozawa et al., 2007]. This study adopts a horizontal resolution of T42 (about $2.8^\circ \times 2.8^\circ$) with 32 vertical layers from the surface to about 40 km altitude. Advective transport is calculated using a fourth-order flux-form advection scheme of the monotonic Van Leer [van Leer, 1977] and flux-form semi-Lagrangian scheme [Lin and Rood, 1996]. Convective transport is also simulated in the framework of the cumulus convection scheme (prognostic Arakawa–Schubert scheme).

CHASER-V3 calculates the photolysis reactions and the gas-phase, liquid-phase, and heterogeneous kinetic reactions (53 species and 154 reactions). Photolysis rate is calculated on-line using temperature and actinic flux computed in the AGCM. The kinetic reactions include the O_3-

HO_x-NO_x-CH_4-CO system and oxidation of non-methane volatile organic carbons (NMVOCs). For NMVOCs, the model includes oxidation of ethane (C_2H_6), ethene (C_2H_4), propane (C_3H_8), propene (C_3H_6), butane (C_4H_{10}), acetone (CH_3COCH_3), methanol (CH_3OH), isoprene (C_5H_8), and terpenes ($C_{10}H_{16}$). SO_2 oxidation with gas-phase and liquid-phase reactions are considered. The liquid-phase oxidations consider dependency on pH, which is computed using SO_4^{2-} and NO_3^- in the model. Dry deposition [Wesely, 1989] and wet deposition (cloud-out and rain-out) processes are also included. Lightning NO_x production is simulated in the framework of cumulus convection scheme according to Price and Rind [1992].

To extract the impact of interannual variation in transport on tropospheric ozone, we also use the framework of a tagged ozone simulation [Sudo and Akimoto, 2007]. The tagged ozone simulation calculates the temporal evolution of a hypothetical ozone tracer using the archived three-hourly production rate and loss frequency of the odd oxygen family (O_y = O_3 + O + O(^{1}D) + NO_2 + 2NO_3 + 3N_2O_5 + PANs + HNO_3 + other nitrates). Ozone accounts for more than 95% of O_y family in remote regions, although it accounts for 70–90% in the polluted regions. The difference between ozone and O_y induces error, because dry and wet depositions of tagged tracer are calculated as ozone. For example, HNO_3 which is counted as O_y induces error through wet deposition process. Therefore, the production rate in the boundary layers is scaled according to ratio of ozone to O_y for reducing the difference. By contrast loss rate in the boundary layer is not scaled, because most of O_y chemical loss are occupied by three reactions; O(^{1}D) + H_2O, O_3 + HO_2, and O_3 + OH.

2.2 Global chemistry–climate model

An atmospheric general circulation model (AGCM) version of MIROC-ESM-CHEM [Watanabe et al., 2011b] is applied to obtain production rate (P) and loss rate (β) of O_x, which is defined as a sum of O_3, O(^{1}D), and O in sections 4 and 5. The original version of MIROC-ESM-CHEM is an earth system model, which includes atmosphere, ocean, and land surface models. The model used for this study consists only of AGCM coupled with a CHASER atmospheric chemistry model [Sudo et al., 2002; Sudo and Akimoto, 2007] and a SPRINTARS aerosol model [Takemura et al., 2000; 2002; 2005; 2009].

The AGCM is based on CCSR/NIES/FRCGC AGCM version 5.7 [K-1 model developers, 2004; Nozawa et al., 2007]. The radiative transfer scheme is an updated version of the *k*-distribution scheme following [Sekiguchi and Nakajima, 2008]. Tracer advection on grid scale is also updated. This model adopts the piecewise parabolic method [Colella and Woodward, 1984] and a flux-form

semi-Lagrangian scheme [Lin and Rood, 1996]. In this mode, the sea surface temperature (SST) and sea ice concentration (SIC) in the model are prescribed as boundary conditions. We adopt a horizontal resolutions of T42 (about $2.8^\circ \times 2.8^\circ$) with 57 vertical layers from the surface to about 52 km altitude. The vertical resolution increases to 1000 m per level from the surface to 5 km, decreases again to 680 m per level from 5 km to 8 km, remains constant (680 m per level) for 8–35 km, and increases to 3500 m per level above 35 km. The hybrid σ (terrain following)–pressure vertical coordinate system is used in the model.

Because this model resolves the stratosphere, it needs to represent deceleration of wind near the model top reasonably. The model uses fourth order ($\bigtriangledown^4$) horizontal hyper-viscosity diffusion. The e-folding time of the smallest resolved wave is 1.3 days for the T42 simulation. Although the model incorporates the McFarlane [1987] orographic gravity wave parameterization, no non-orographic gravity wave parameterization is included.

CHASER simulates details of photochemistry in the troposphere and the stratosphere, chemical tracer transport, wet and dry deposition, and emissions. In this study, the model incorporates 93 species and 263 reactions (58 photolytic, 184 kinetic, and 21 heterogeneous reactions). The chemistry, dry deposition, wet deposition, and emission processes in the troposphere are following CHASER-V3. This model also includes detailed stratospheric chemistry involving ClO_x, HCl, HOCl, BrO_x, HBr, HOBr, Cl_2, Br_2, BrCl, $ClONO_2$, $BrONO_2$, CFCs, HFCs, and OCS. The all chemical reactions are calculated in the troposphere and the stratosphere. In the stratosphere, the model also simulates formation of the polar stratospheric cloud (PSC), its gravitational settling, and heterogeneous reactions (13 reactions for halogen species and N_2O_5) on it. The model used the scheme which is adopted in the Center of Climate System Research (CCSR)/National Institute of Environmental Studies (NIES) stratospheric chemistry–climate model [Nagashima et al., 2002; Akiyoshi et al., 2004]. The scheme consider liquid binary aerosol (LBA), nitric acid trihydrate (NAT), and ice PSCs assuming thermodynamic equilibrium. The scheme also includes gravitational settling of LBA, NAT, and ice to represent irreversible removal of HNO_3 and H_2O (i.e. de-nitrification and de-hydration processes, respectively) from the stratosphere. Additional information of MIROC-ESM-CHEM can be found in Watanabe et al. [2011b].

SPRINTARS calculates mass mixing ratios of the aerosols: carbonaceous (BC and organic matter; OM), soil dust, and sea salt. The model includes emission, advection, diffusion, wet deposition, dry deposition, and gravitational settling. Emissions of soil dust and sea salt are calculated in the model. SPRINTARS is coupled with the radiation scheme and the cloud/precipitation schemes direct, semi-direct, and indirect effects of aerosols. Detailed descriptions can be found in Takemura

et al. [2002] for the aerosol direct effect, Takemura et al. [2005; 2009] for the aerosol indirect effect.

We also used an O_3-tracer-transport (tagged tracer) version of MIROC-ESM-CHEM [Sudo and Akimoto, 2007]. Atmospheric dynamical and physical processes in the model are identical to those in the original version of MIROC-ESM-CHEM. The ozone tendency at each grid is written as

$$\frac{dC}{dt} = \left(\frac{dC}{dt}\right)_{transport} + \left(\frac{dC}{dt}\right)_{drydeposition} + P - \beta C, \tag{2.1}$$

where C stands for the ozone concentration, and where subscripts denote processes. The model calculates the ozone tendency attributable to transport and dry deposition processes (first and second term) in the same way as the original version, although P and β are prescribed by the output obtained from the AGCM version of MIROC-ESM-CHEM. The P and β at each time step are linearly interpolated from the three hourly mean outputs of P and β. Using the model with T42 ($2.8^\circ \times 2.8^\circ$) and T106 ($1.1^\circ \times 1.1^\circ$) horizontal resolutions, we test the sensitivity of change in stratospheric and tropospheric ozone to change in horizontal resolution. For the T106 model, the e-folding time of the smallest resolved wave is 0.9 days. The P and β for the T106 model are linearly interpolated from the P and β for the T42 model. To test an impact of the interpolation method, we compare the T106 simulations in which two types of P and β are prescribed. One is linearly interpolated, and another is calculated by the area-weighted interpolation. The comparison suggests that the difference of ozone attributable to the interpolation method is less than that attributable to the meteorological field (see the supporting material). This study does not consider an impact of horizontal resolution on ozone chemistry in the stratosphere and the troposphere, because the P and β for the T106 model is calculated from those for the T42 model. We also used the model to perform the simulation which quantifies the individual contributions of transport and chemical processes.

Chapter 3

Interannual variation of global tropospheric ozone

3.1 Introduction

Meteorological variability, biomass burning, and other natural sources of NO_x, CO, and VOCs could affect interannual ozone variation. Results of earlier studies suggested that interannual ozone variation is controlled substantially by meteorological variability [Kurokawa et al., 2009; Hess and Mahowald, 2009; Pozzoli et al., 2011], such as that attributable to El Niño Southern Oscillation (ENSO) and Arctic Oscillation (AO) [e.g. Lamarque and Hess, 2004; Doherty et al., 2006].

Interannual variation of ozone induced by ENSO has been studied using both satellite observation and global models. The earliest work studied changes in tropospheric column ozone derived from satellite observations during 1997 El Niño [Chandra et al., 1998]. Several modeling studies simulated changes in tropospheric ozone in 1997 to quantify the impacts of Indonesian wildfires and meteorological changes [Sudo and Takahashi, 2001; Chandra et al., 2002]. Recently, changes in tropospheric ozone and carbon monoxide during the 2006 El Niño and the positive phase of Indian Ocean Dipole (IOD) were examined by combining measurements and model simulations [Chandra et al., 2009; Nassar et al., 2009; Zhang et al., 2011]. Other studies characterized the response of ozone to ENSO using long-term observations and simulations [Ziemke and Chandra, 1999; Peters et al., 2001; Doherty et al., 2006; Koumoutsaris et al., 2008; Ziemke et al., 2010; Oman et al., 2011; 2013; Randel and Thompson, 2011]. Results obtained from these studies suggest that changes in tropospheric ozone associated with ENSO were caused not only by extensive forest fires throughout Indonesia, but also by marked changes in meteorological conditions.

Some studies have examined the impact of AO on interannual variation in ozone in the northern

midlatitudes to high latitudes. Lamarque and Hess [2004] described that AO can explain up to 50% of the ozone variation observed by ozonesonde below 500 hPa over the North American continent in spring. Creilson et al. [2005] found that AO correlates with the tropospheric ozone residual derived from satellites over Europe in springtime. Hess and Lamarque [2007] attributed changes in ozone associated with AO to four source regions: Europe, North America, Asia, and the stratosphere. They asserted that the change in ozone from the stratosphere decreases ozone throughout the troposphere over northern Canada and the Arctic, and that the regional changes in surface ozone around Europe, United States, Siberia, and East Asia are governed by changes in the transport of ozone produced in the troposphere.

Effect of interannual variation in the Hadley circulation and effect of interannual variation in Asian monsoon circulation on tropospheric ozone have been examined only cursorily. Liu et al. [2011] described that the Asian ozone anomaly over the Middle East correlates with two independent summer monsoon indices, suggesting that intensified Asian summer monsoon circulation also enhances the transport of Asian ozone to the Middle East. However, the impact of Asian winter monsoons on TCO has not been investigated.

As described above, researchers have examined the impact of individual meteorological variability, in particular ENSO and AO, on ozone. However, interannual variation in the global distribution of tropospheric ozone is not understood comprehensively. In this study, we investigate interannual changes in global tropospheric ozone associated with meteorological variability, and quantify the contribution of meteorological variability to total interannual variation in global and regional tropospheric ozone.

Additionally, Sudo and Takahashi [2001] reported that key meteorological factors of the ozone changes are upward-downward motion, suppressed–enhanced convection, and their associated water vapor changes. However, the respective contributions of factors are not understood quantitatively. This study assesses individual impacts of transport process (advection via large-scale circulation and cumulus convection, and vertical diffusion) and chemical process (temperature, water vapor, cloud, and lightning).

Section 3.2 described the experimental settings, observational data, and analytical methods. We investigated the impacts of ENSO, IOD variability, interannual variation in Hadley circulation, interannual variation in Asian monsoon circulation, and AO on tropospheric column ozone (TCO), and discussed their mechanisms in section 3.3. Their contributions to interannual variation in regional ozone are quantified in section 3.4. Finally, in section 3.5, we summarize the results and present our conclusions.

3.2 Methodology

3.2.1 Full-chemistry simulation during 1970–2008

We performed simulations for the 39 years of 1970–2008 (hereinafter S1). Meteorological fields (horizontal wind and temperature) in CHASER are relaxed to 12 hourly National Center of Environmental Prediction/National Center of Atmospheric Research (NCEP/NCAR) reanalysis data [Kalnay et al., 1996]. The simulation uses the Hadley Centrefs Sea Ice and Sea Surface Temperature data set (HadISST) [Rayner et al., 2003].

In the simulation, emissions of ozone precursors do not vary year to year (except lightning NO_x), which facilitates evaluation of the impact of year-to-year variation in meteorology on tropospheric ozone apart from that of year-to-year variation in emissions. However, anthropogenic and biomass burning emissions include only decadal changes. Anthropogenic emissions are based on EDGAR HYDE [van Aardenne et al., 2001] and 3.2 FT2000 [Olivier et al., 2005]. Biomass burning emissions are from GFED ver. 2 [van der Werf et al., 2006]. We constructed biomass burning emission assuming that (1) its annual amount has decadal variation in proportion to the population in the corresponding region, (2) its burned location and timing are maintained at 2001 levels. Our constructed CO emission shows positive trend slightly larger than RETRO emission in the tropics where biomass burning occupy a half of total emission. We chose 2001 as the base year of timing and location, because biomass burning in Indonesia was not influenced by ENSO. However, global total emission from biomass burning in 2001 was larger than average during 1997–2004 [van der Werf et al., 2006]. The larger emission was mainly responsible for emissions in Africa and Australia. Therefore, we need to interpret our model result with caution. The simulation includes natural sources of NO_x from soil (5 Tg N/yr) and lightning (about 5 Tg N/yr). The amount derived from lightning varies from year to year because it is parameterized in the framework of cumulus convection scheme according to Price and Rind [1992]. Biogenic emissions of isoprene (400 Tg C/yr) and terpenes (100 Tg C/yr) are calculated according to Sudo and Akimoto [2007]. Because we focus on direct impact of meteorological variability on transport and chemistry processes, we adopted monthly mean climatology of biogenic emission.

The ozone concentration above 20 km is relaxed to the prescribed data at each grid. The data is based on monthly climatological distribution of Halogen Occultation Experiment project (HALOE) and decadal change estimated from equivalent effective stratospheric chlorine (EESC). Therefore, the ozone above 20 km does not include interannual variation due to meteorological variability. Additionally, zonal mean ozone between tropopause and 20 km is relaxed to that of the data. The

prescribed NO_y data are output from a three-dimensional stratospheric chemistry model [Takigawa et al., 1999].

3.2.2 Simulation fixed to chemical field in 1990

Interannual variation in meteorology influences the tropospheric ozone distribution through both transport (advection, convection, and diffusion) and chemical (production and loss) processes. To isolate the impact of interannual variation in transport on ozone, we performed a simulation fixed to the 1990 chemical field (chemical production and loss rate of O_y) for 39 years (hereinafter S2). The chemical field in 1990 is not largely influenced by meteorological variability, because all indices for 1990 do not exceed to one standard deviation (Figure 1). The ozone tendency at each grid is written as

$$\frac{dC}{dt} = \left(\frac{dC}{dt}\right)_{transport} + \left(\frac{dC}{dt}\right)_{drydeposition} + P - \beta C \tag{3.1}$$

where C stands for the ozone concentration, P denotes the ozone production rate, β signifies the ozone loss rate, and subscripts denote processes. In this simulation, we maintained the chemical production rate (P) and loss rate (β), and allowed the other tendencies (first and second term) to vary among years. A similar approach was used by Liu et al. [2011].

We simultaneously calculated separate ozone tracers from 23 regions using the 1990 chemical field. Although chemical loss of each tracer is calculated using archived loss rate everywhere in the model domain, chemical production of each tracer is calculated only inside its corresponding region. The regions were defined following asSudo and Akimoto [2007] (Figure 3.1); 14 planetary boundary regions (defined as lowermost 7 model layers), 9 free troposphere regions. Additionally, ozone tracer of stratospheric origin was calculated by setting it equal to ozone (ozone from all regions) in the stratosphere at each time step. For simplicity, we present contributions of 10 source regions to the ozone variability; Stratosphere (STR), North America (AMN = BL-AMN + BL-AMM + FT-AMN), South America (AMS = BL-AMS + FT-AMS), Europe (EUR = BL-EUR + FT-EUR), North Africa (AFN = BL-AFN + FT-AFN), South Africa (AFS = BL-AFS + FT-AFS), Asia (ASA = BL-CHN + BL-IND + BL-JPN + BL-TLD + FT-EAE + FT-EAW), Indonesia (IDN = BL-IDN + FT-IDN), Australia (ARL = BL-ARL + FT-ARL), and rest of the world (RMT).

3.2.3 Obaservational data

We evaluate the performance of CHASER with satellite and ozonesonde observations. Interannual variation in global tropospheric column ozone distribution is evaluated using satellite observa-

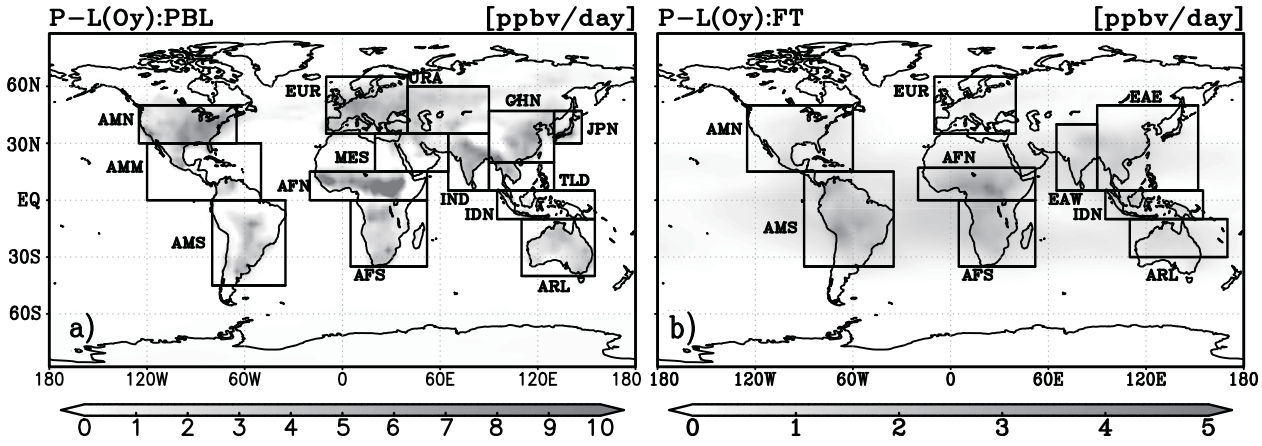

Figure 3.1. Definition of source regions for tagged tracer simulation for O_3 performed in this study. (a) Definition of planetary boundary layer (below about 3 km), (b) definition of free troposphere. Shade depicts annual mean production rate of O_y (ppbv/day) in 1990.

tions from the Tropospheric Emission Spectrometer (TES). TES is a Fourier transform IR emission spectrometer [Beer et al., 2001] on Aura. TES retrieval is based on the optimal estimation approach [Rodgers, 2000]. Details are described by Bowman et al. [2006] and Kulawik et al. [2006]. The prior profile is taken from monthly mean ozone in blocks of $10^\circ \times 60^\circ$ simulated by MOZART model. We use the TES ver. 3 nadir-viewing measurement of ozone. We map TES swath data, which have a 5×8 km^2 footprint, to the T42 grid. TES vertical sensitivity depends on altitude. Therefore, the model results were adjusted for the sensitivity by application of the averaging kernel and constraint vector (a priori profile). The modeled ozone profile was sampled at the closest grid box and time to the measurement. Data screening criteria are given following Zhang et al. [2010].

We also used tropospheric column ozone (TCO) data derived from the Total Ozone Mapping Spectrometer (TOMS) to evaluate the interannual variation of TCO in the tropics. The TCO is calculated using the convective cloud differential (CCD) method [Ziemke et al., 1998]. In the CCD method, TCO is computed by subtracting stratospheric column ozone (SCO) from total column ozone. SCO and total column ozone were derived, respectively, from high and low reflectivity measurements. We used data for the 25 years of 1979–2005 derived from TOMS on Nimbus7 and Earth Probe.

We evaluate interannual variation of TCO in North America and the northern high latitude with ozonesonde observation data. The data are from the World Ozone and Ultraviolet Data Center (WOUDC). We use data obtained from eight sites: Boulder, Huntsville, and Wallops for North America, and Resolute, Thule, Ny-Alesund, Eureka, and Alert for the high northern latitudes. In the two regions, interannual variation in ozone is largely influenced by ENSO, AO, and Hadley circulation (see section 3.4.2).

3.2.4 Analytical method

This study investigates the impacts of meteorological variability on the interannual variation in global TCO. To quantify the impact, we calculated the linear regression and correlation coefficient of TCO with respect to index of climate variability. The regression and correlation coefficients are calculated against each index separately, because Niño3.4 index correlates with DMI significantly (r = 0.7). We multiplied the regression coefficient by the standard deviation of each index to express physical magnitude of change for a gtypicalh event. We used the Niño3.4 index and dipole mode index (DMI) [Saji et al., 1999], respectively, as the ENSO and IOD index. The AO index is defined as the empirical orthogonal function (EOF) first mode of sea level pressure field in the model. The indices of Hadley and Asian monsoon circulations were constructed following Tanaka et al. [2004]. The indices are calculated from the velocity potential at 200 hPa. The velocity potential is defined as

$$\nabla \cdot \mathbf{V_H} = -\nabla\chi \tag{3.2}$$

where $\mathbf{V_H}$ is the horizontal wind vector, and χ denotes the velocity potential. At each grid we decompose the velocity potential into three components as,

$$\chi = [\chi] + \overline{\langle\chi\rangle} + \langle\chi\rangle' \tag{3.3}$$

where brackets and angle brackets are respectively zonal mean and deviation from it, and over bar and prime respectively denote one-year running mean and deviation from it. The Hadley index is defined as the minimum (maximum) value of $[\chi]$ in boreal winter (summer). The monsoon index is defined as the maximum (minimum) value of $\langle\chi\rangle'$ in boreal summer (winter). These indices can be defined only in summer and winter. Interannual variations of the indices used for this study are shown in Figure 3.2. The Hadley index in boreal winter shows a marked strengthening trend, which is consistent with Tanaka et al. [2004]. For linear regression and correlation calculation, we removed the linear trend of index and ozone in linear regression and correlation calculation to highlight year-to-year variation rather than a long-term trend.

We further adopt partial correlation technique [Spiegel, 1988] to distinguish the impacts of ENSO and IOD on the tropospheric ozone, because the Niño3.4 index correlates closely with DMI (r = 0.7). The partial correlation coefficient $r_{AB,C}$ between variable A and B after excluding the influence of variable C is defined as

$$r_{AB,C} = \frac{r_{AB} - r_{AC}r_{BC}}{\sqrt{1 - r_{AB}^2}\sqrt{1 - r_{BC}^2}} \tag{3.4}$$

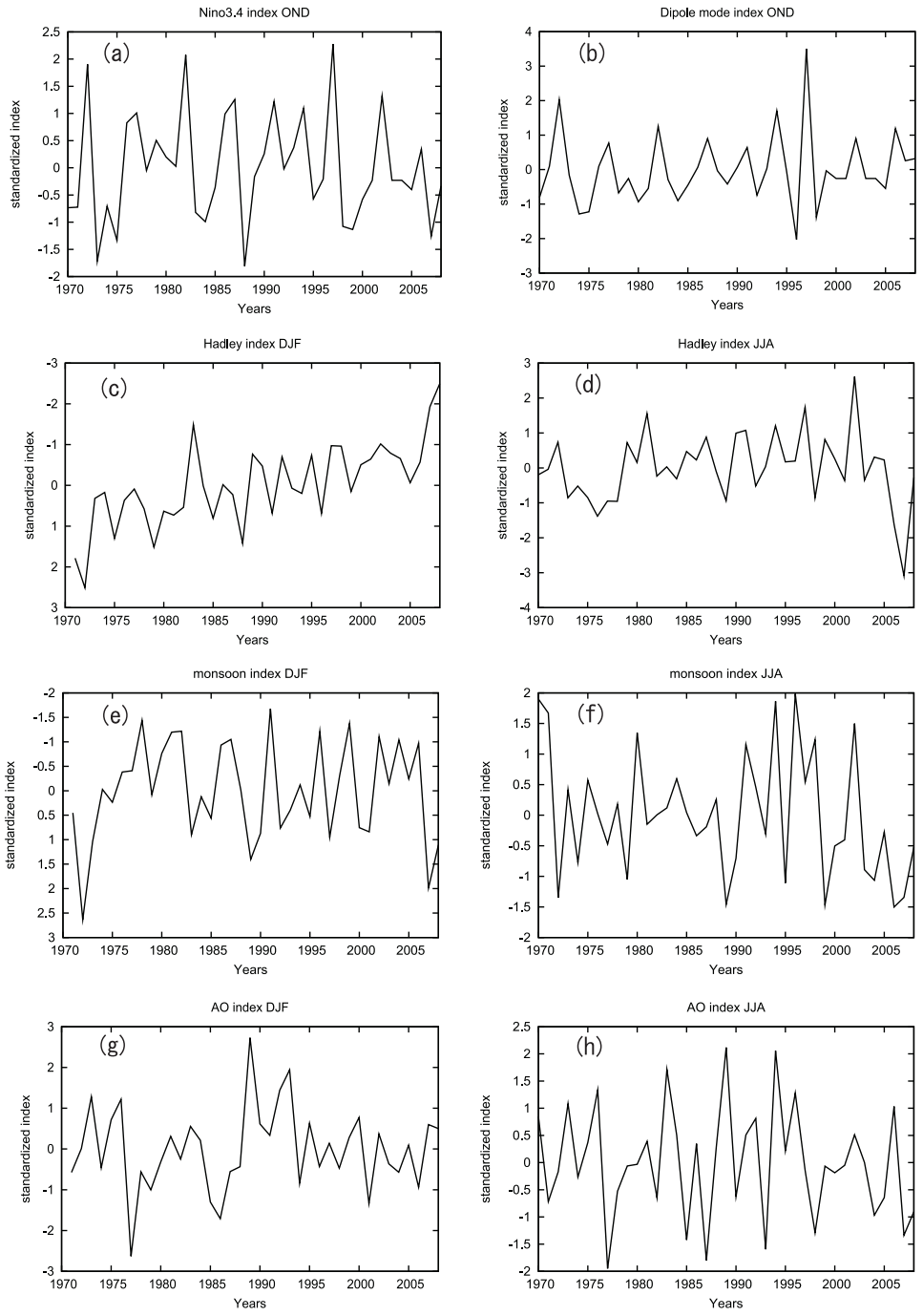

Figure 3.2. Indices of (a) Niño3.4, (b) Indian Ocean Dipole, (c, d) Hadley and (e, f) Asian monsoon circulations, and (g, h) Arctic Oscillation. The indices are standardized with their +1 standard deviation. Nino3.4 and the dipole mode index are seasonal means for October–November–December (OND). Figures 1c, 1e, and 1g and Figures 1d, 1f, and 1h respectively show seasonal means for December–January–February (DJF) and for June–July–August (JJA). The y axis of Hadley and Asian monsoon circulation indices for DJF is reversed. The details of Hadley and monsoon indices are described in Tanaka et al. [2004]

where r_{AB} is the linear correlation coefficient for A and B, and so on. We calculated the partial correlation coefficients between TCO and Niño3.4 index after excluding the influence of DMI (i.e., $r_{TCONiño3.4,DMI}$), and between TCO and DMI after excluding the influence of Niño3.4 index (i.e., $r_{TCODMI,Niño3.4}$).

We also characterize the interannual variation of tropospheric ozone with Empirical Orthogonal Functions (EOFs). The general application of EOF analysis to the geophysical field is described by Wilks [2006]. We applied EOF analysis to monthly and seasonal ozone anomalies (difference from average for 1970–2008). Each meteorological variability-related signal was explored by examining the EOF spatial patterns (EOF) and the corresponding principal component time series (PC) with its index for the first four EOF modes. We multiplied EOF spatial patterns by the standard deviation of corresponding PC time series, as for the regression coefficient.

3.3 Interannual variation of the global tropospheric ozone distribution

3.3.1 Comparison with satellite observation

We first compare annual mean of simulated tropospheric column ozone (TCO) with that of TCO derived from the TES instrument in Figure 3.3. The model captures general features of TES observation. It reproduces the zonal wave-one pattern of tropical TCO with minimum of 20 DU in the western Pacific and maximum of 40 DU in the Atlantic. TCO enhancements of 40–50 DU in eastern Asia and United States are also captured well, but the enhancement in the Pacific and the Atlantic are underestimated slightly. The simulated TCO is also low-biased (6–9 DU) in the high northern latitudes. TCO peaks of South Asia and the Middle East are overestimated in the model (3–6 DU).

We then evaluate interannual variation in zonal and tropical mean TCO with TES observations. A time-versus-latitude Hovmoller diagram of zonal and monthly mean TCO is portrayed in Figure 3.4. The monthly TCO is deseasonalized by subtracting the average during 2005–2007 in corresponding months. The modeled anomalies generally correlate with observed anomalies (r = 0.51). The correlation coefficient is significant at 99% confidence level. In high northern latitudes, the model captures observed decrease in 2006 and increase in 2007 in boreal winter. Although the observed anomaly in November and December 2007 may be related to the positive phase of AO, the modeled anomaly is not obvious. By contrast, the model does not reproduce observed anomalies

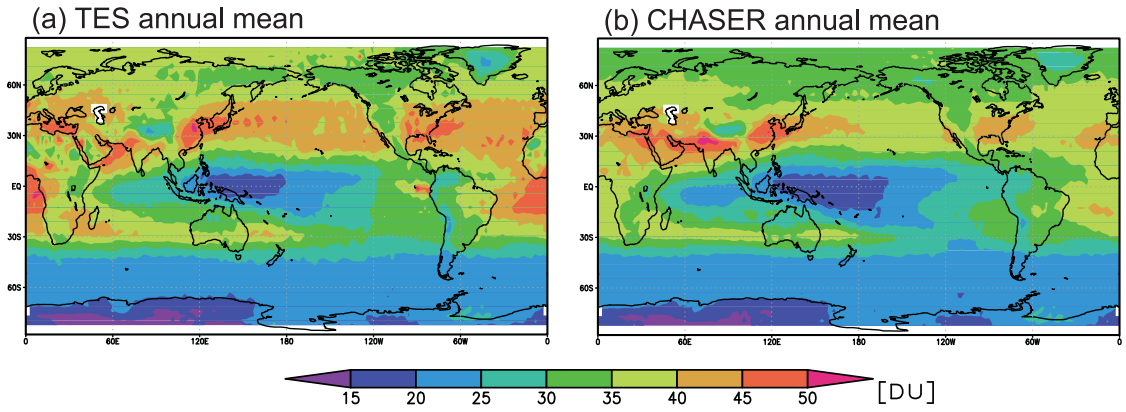

Figure 3.3. Annual mean distributions of tropospheric column ozone (TCO) (a) derived from TES instrument and (b) simulated by CHASER. TCO is averaged for 2005–2007. The modeled TCO was sampled at the closest grid box and time to the observation. The TES averaging kernel was applied to the modeled TCO. The unit is the Dobson Unit (DU).

in the boreal summer. The discrepancy is probably attributable to prescribed stratospheric ozone. The model underestimates ozone decrease (increase) observed by Microwave Limb Sounder/Aura (about 80%) at 100 hPa during spring–early summer in 2006 (2007) in the northern mid to high latitude. The underestimation might have affected interannual variation of TCO through stratosphere to troposphere transport. TES observation also shows a negative (positive) anomaly in the tropics and positive (negative) anomalies in the subtropics in late 2006 (2007). The model reproduces these anomalies, which can be linked to ENSO and Hadley circulation.

Figure 3.5 shows a time-versus-longitude Hovmoller diagram of monthly TCO anomaly averaged from 15°S to 15°N. The TCO is deseasonalized, as in Figure 3.4. The model generally captures observed anomalies (r = 0.53). The significance of correlation coefficient exceeds 99% confidence level. Both the observed and the simulated TCO changes show positive (negative) anomaly in late 2006, and negative (positive) anomalies in late 2005 and 2007 in the western Pacific and the eastern Indian Ocean (eastern Pacific). In addition, positive and negative anomalies are found, respectively, in the western Indian Ocean in late 2005 and 2006. These signals in the Pacific and the Indian Ocean can result from ENSO and IOD respectively. The simulated anomalies are smaller than the TES observations around Indonesia, primarily because of a lack of anomalous Indonesian forest fires in 2006 in the model. The model tends to capture the observed interannual variation in TCO during October–December (OND) in the tropics (r = 0.54, significant at 99% confidence level), and during December–February (DJF) in the high northern latitudes well (r = 0.53, significant at 99% confidence level). We show that ENSO, IOD, and AO can be related to interannual variation in TCO. Therefore, we investigate the impact of ENSO and IOD in OND, and

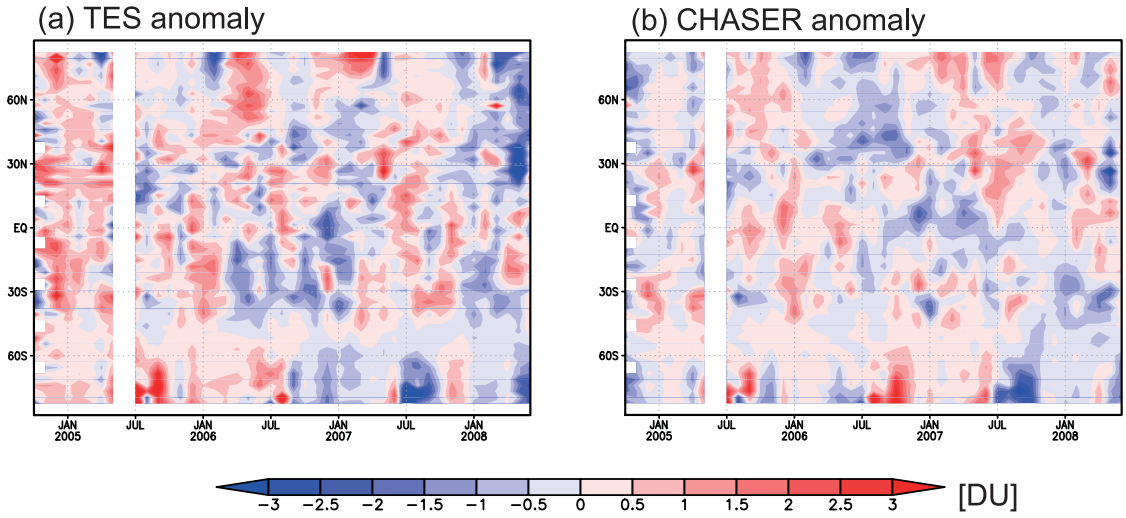

Figure 3.4. Time–latitude cross section of monthly and zonal mean deseasonalized TCO anomaly (DU) showing the anomaly (a) derived from TES and (b) simulated by CHASER.

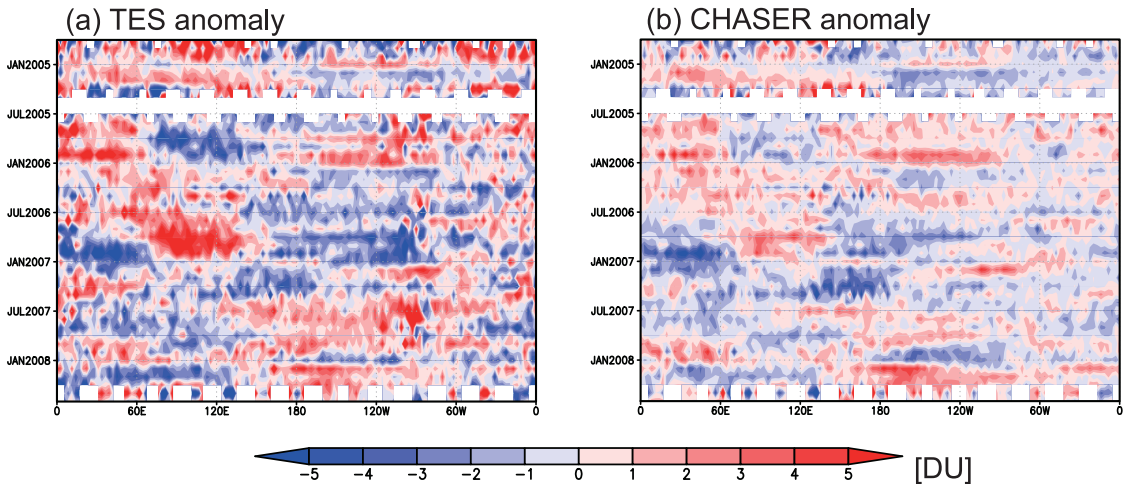

Figure 3.5. Longitude–time cross section of monthly deseasonalized TCO anomaly (DU) averaged between 15°S and 15°N showing the anomaly (a) derived from TES and (b) simulated by CHASER.

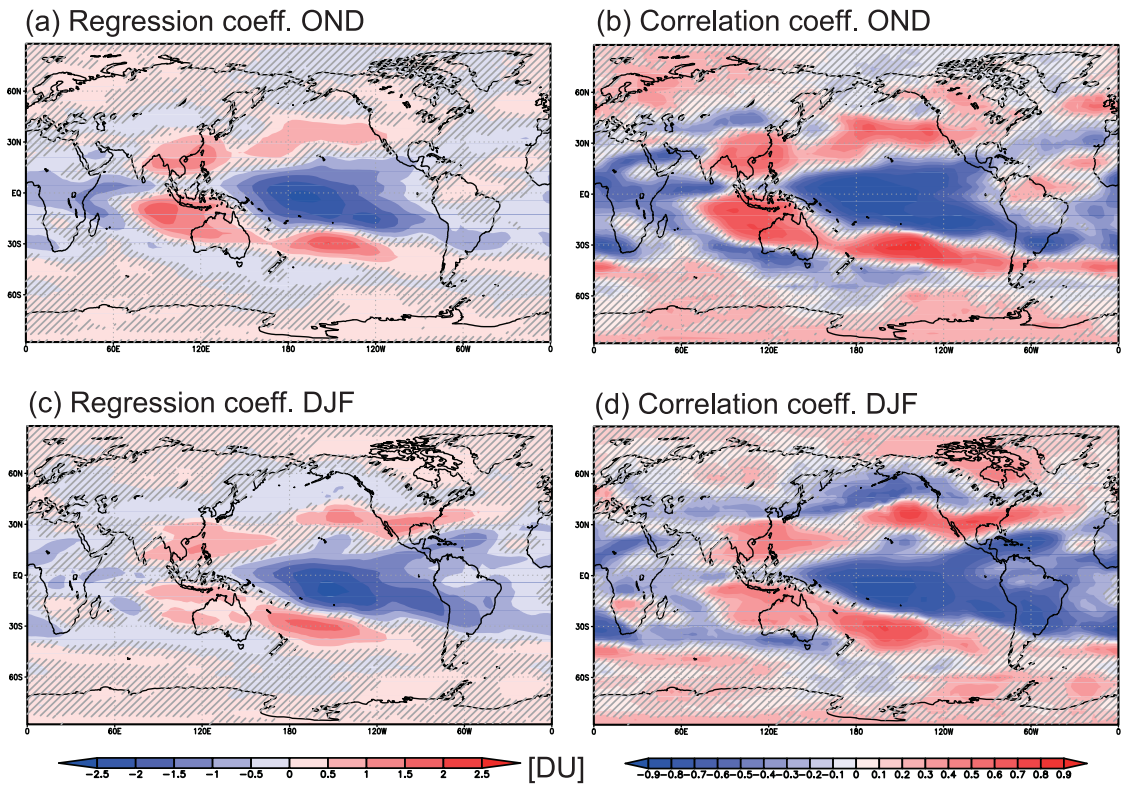

Figure 3.6. (a, b) Regression coefficient of TCO (DU) with respect to Nino3.4 index and (c, d) partial correlation coefficient of TCO with respect to Nino3.4 after excluding the influence of DMI. Figures 3.6a and 3.6c are calculated using TCO and the index in OND. Figures 3.6b and 3.6d are calculated using TCO in DJF and the index in OND (correspond to a 2 month lag). Hatched regions are not significant at the 95% confidence level.

ENSO and AO in DJF below. Additionally, we address interannual variation in Hadley and Asian monsoon circulations in DJF.

3.3.2 Impact of El Niño–Southern Oscillation

Figure 3.6a shows regression coefficient of TCO with respect to the Niño3.4 index in OND. A two-tail Studentfs t-test demonstrated that hatched regions are not significant at the 95% level. The result shows a positive anomaly of 1–1.5 DU in the tropical western Pacific including Indonesia, and a negative anomaly of 2.5 DU in the tropical eastern Pacific. The model also exhibits positive anomalies of 0.5–1.5 DU in the central to eastern Pacific over the subtropics. The correlation coefficient shows a similar pattern (not shown). Significant correlation was found in the tropical eastern Pacific (r = 0.8), Indonesia (r = 0.6) and the eastern Pacific over the subtropics (r = 0.8). These spatial patterns are consistent with those described in earlier studies [Doherty et al., 2006; Oman et al., 2011].

Two month-lagged regression coefficient of TCO with respect to the Niño3.4 index (i.e., regression between TCO in DJF and Niño 3.4 index in OND) is presented in Figure 3.6b. We picked the two month-lagged regression to compare impact of ENSO with that of Hadley circulation in southern North America in DJF. The anomalies in DJF show a similar pattern to that in OND, while positive anomaly in southern North America is elevated from 0.2 DU to 1 DU. The positive anomaly can result from the combination of an enhanced local Hadley cell and intensified subtropical jet in the eastern Pacific because of ENSO [Shapiro et al., 2001; Wang, 2002] through changes in the horizontal and vertical transport in troposphere, and stratosphere–troposphere exchange of ozone [Hsu et al., 2005; Koumoutsaris et al., 2008].

Sudo and Takahashi [2001] reported that large-scale atmospheric circulation, cumulus convection, and water vapor are key factors contributing to tropical TCO change during El Niño. However, the respective factorsf contributions to the TCO change are not understood quantitatively. We attempt to quantify the impact of interannual variation in transport (large-scale circulation and cumulus convection) and chemistry (water vapor, etc.) associated with ENSO using the two simulations described in sections 3.2.1 and 3.2.2. S1 accommodates year-to-year variation of both meteorological (transport) and chemical fields (production and loss rate of O_y), but S2 allows only the meteorological (transport) field to vary. In this study, we define the impact of transport as regression coefficient of TCO in S2 with respect to the Niño3.4 index. We also define the impact of chemistry as regression coefficient of TCO difference between S1 and S2.

Figures 3.7a and 3.7b respectively show the impacts of transport and chemistry. The impact of transport is greater than that of chemistry over most of the globe. The significant impact of chemistry is confined to the tropical central Pacific, where the impacts of transport and chemistry are comparable, although the chemistry process has less impact in Indonesia. This lesser impact is attributable to cancelling out of the positive anomaly below 5 km and negative anomaly above 5 km over Indonesia (Figures 3.7c and 3.7d). The positive anomaly (+0.2 DU) below 5 km is related to a decrease in the chemical loss of ozone with water vapor, while negative anomaly (0.1 DU) above 5 km is related to a decrease in chemical production of ozone from lightning NO_x. However, this simulated change in lightning over Indonesia is opposite to the change derived from LIS/TRMM [Hamid et al., 2001]. They showed that convective storms were concentrated on land and the coast area, and that the number of lightning flashes increased during 1997–1998 (El Niño year) compared to 1998–1999. We must improve convection and lightning NO_x schemes, for example, as did Nassar et al. [2009]. In addition, the impact of chemistry may include some bias, because only one year (1990) of chemical fields is used in S2. However, as Figure 1 shows, all indices were

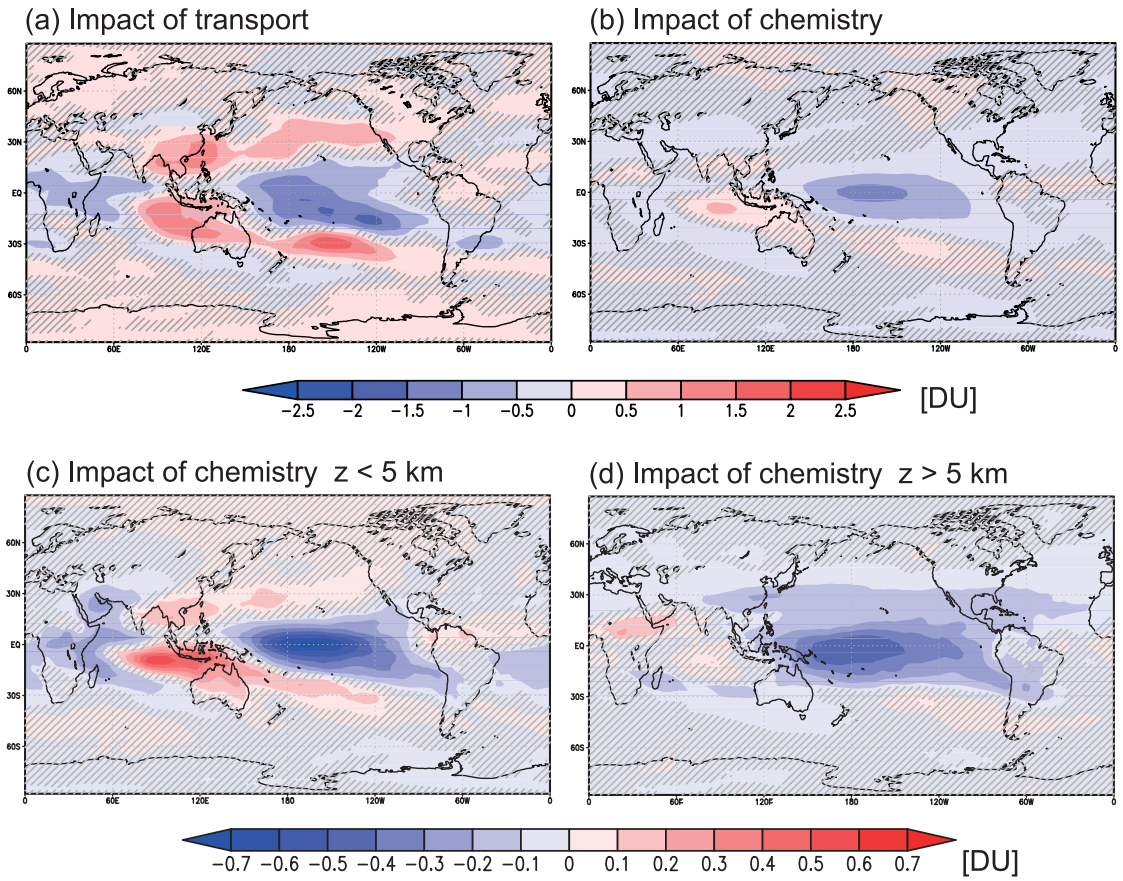

Figure 3.7. Impact of interannual variation in (a) transport and (b) chemistry on the regression coefficient of TCO (DU) with respect to the Nino3.4 index shown in Figure 5a, and impact of chemistry on column ozone (c) between surface and 5 km and (d) between 5 km and tropopause. The impacts are seasonal averages for OND. Hatched regions are not significant at the 95% confidence level.

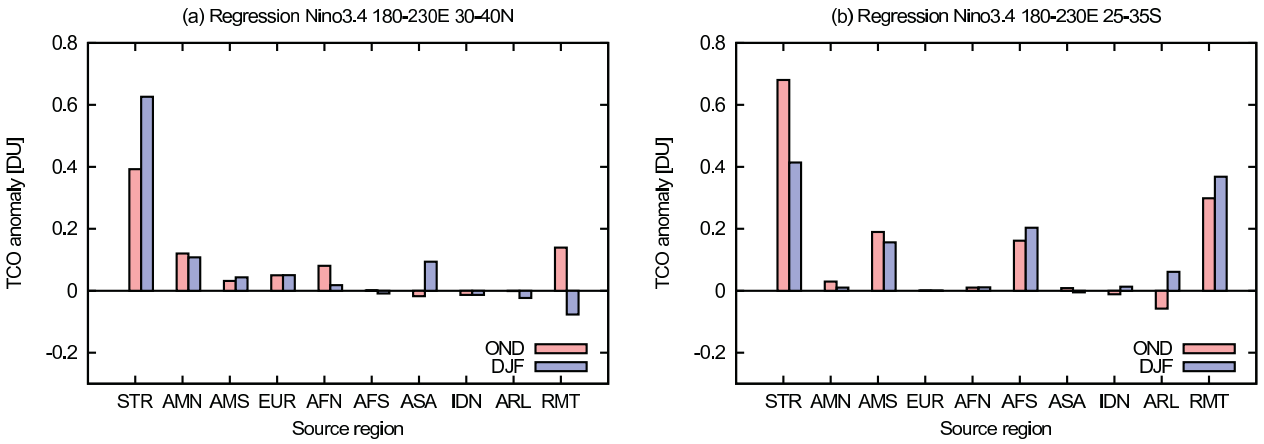

Figure 3.8. Regression coefficient of ozone from each source regions with respect to Niño3.4 index in (a) the northern midlatitude (30°N–40°N, 180°–230°E) and (b) the southern subtropics (25°S–35°S, 180°–230°E). The source regions in the troposphere are shown in Figure 3.1

within one standard deviation in 1990.

Previous studies showed that the increase of TCO in the northern extratropics can result from enhanced Asian pollution transport and stratosphere–troposphere exchange [Langford et al., 1998; Hsu et al., 2005; Zeng and Pyle, 2005; Koumoutsaris et al., 2008; Voulgarakis et al., 2011]. We attribute sources of the TCO increase in the northern and southern extratropics. Figure 3.8a shows contributions of 10 source regions to the TCO increase in the northern extratropics over the eastern Pacific (30°N–40°N, 180°–230°E). Ozone from the stratosphere (STR) is most responsible for the TCO increase. Second most contribution is ozone from the North America (AMN). Ozone from Asia have an impact on the TCO increase in DJF. In the southern extratropics over the eastern Pacific, stratospheric-origin ozone is also most important source of TCO increase (Figure 3.8b). Ozone from South America (AMS) and South Africa (AFS) contributes to the TCO increase (Figure 3.8b).

3.3.3 Impact of Indian ocean dipole variability

Figure 3.9a presents regression coefficient with respect to DMI in OND. Positive anomaly (+1.5–2 DU) is evident in the eastern Indian Ocean and Indonesia. Negative anomaly (1–1.5 DU) is also found in the western Indian Ocean and eastern Africa. Large-scale descent (ascent) flow, suppressed (enhanced) convection, and dryness (wetness) are found in the eastern Indian Ocean (western Indian Ocean) during the positive phase of IOD (not shown). These results suggest that the mechanism causing the changes is analogous to ENSO. We further assess the partial correlation coefficients between TCO and Niño3.4 index after removing the influence of DMI (Figure 3.6c) and

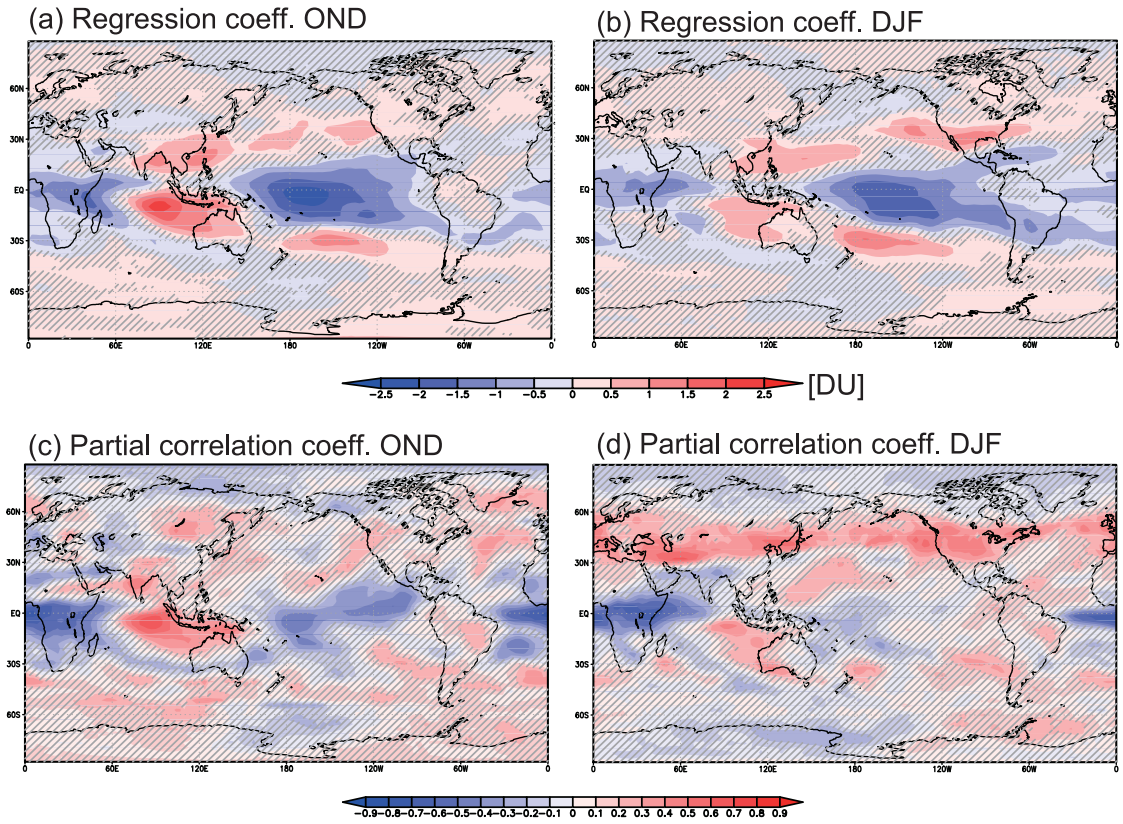

Figure 3.9. (a, b) Regression coefficient of TCO (DU) with respect to the dipole mode index (DMI) and (c, d) partial correlation coefficient of TCO with respect to DMI after excluding the influence of Niño3.4 index. Figures 3.9a and 3.9c are calculated using TCO and the index in OND. Figures 3.9b and 3.9d are calculated using TCO in DJF and the index in OND (corresponding to a 2 month lag). Hatched regions are not significant at the 95% confidence level.

between TCO and DMI after removing the influence of Niño3.4 index (Figure 3.9c), because DMI correlates significantly with the Niño3.4 index (r = 0.7). Figure 3.9c shows positive and negative partial correlations in the eastern and western Indian Ocean (r = 0.6 and 0.6) respectively. Although Figure 3.6c shows positive partial correlation between TCO and Niño3.4 in the southeastern Indian Ocean, Negative partial correlation is found along equator in the Indian Ocean. These imply that dipole structure in the Indian Ocean in Figure 3.9a results from IOD rather than ENSO. In the tropical eastern Pacific, negative partial correlation between TCO and DMI is weaker than that between TCO and Niño3.4 index, suggesting that the impact of ENSO is dominant.

Two month-lagged regression coefficient with respect to DMI is also shown in Figure 3.9b as for Figure 3.6. Regression coefficient shows similar patterns to those with respect to Niño3.4. Figure 3.9d shows that two month-lagged partial correlation between TCO and DMI in the western Indian Ocean is significant (r = 0.6). However, the partial correlation between TCO and DMI in the tropical Pacific and southern North America is weaker than that between TCO and Niño3.4 index

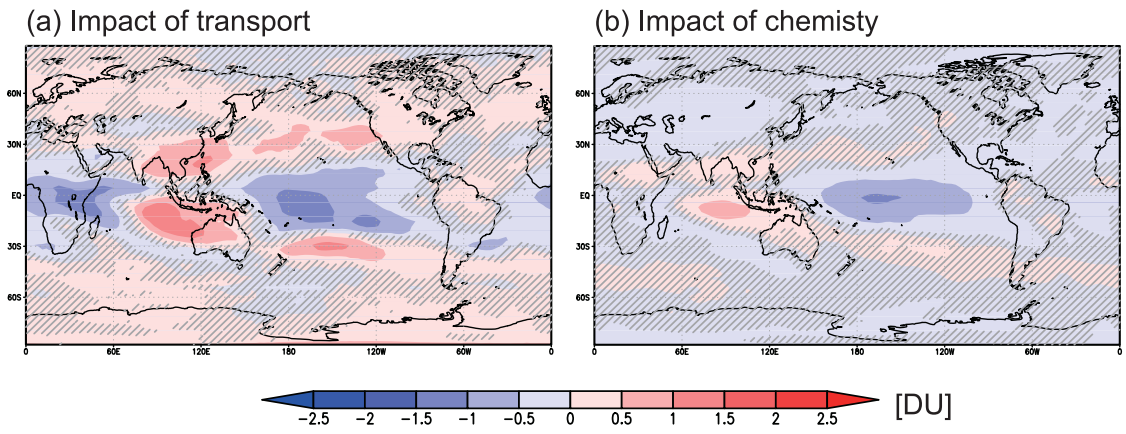

Figure 3.10. Impact of interannual variation in (a) transport and (b) chemistry on the regression coefficientof TCO (DU) with respect to DMI shown in Figure 3.9a. The impacts are seasonal averages for OND. Hatched regions are not significant at the 95% confidence level.

(Figures 3.6d and 3.9d).This suggests that the anomalies are due to the impact of ENSO rather than to that of IOD.

We also quantify the impacts of interannual variation in transport (atmospheric circulation and convection) and chemistry (water vapor, etc.) associated with IOD on TCO as for ENSO. Figure 3.10 presents the impacts of transport and chemistry. The impact of transport is greater than that of chemistry as for ENSO. The significant impact of chemistry is confined to the eastern Indian Ocean. Over eastern Africa, increased ozone production from lightning NO_x and increased ozone loss with water vapor cancel each other. We need to interpret them with caution, because they may be also influenced by ENSO. Nevertheless the partial correlation in Figure 3.9c suggests that the anomalies are mainly caused by IOD.

3.3.4 Impact of Hadley circulation

Figure 3.11a presents regression coefficient of TCO with respect to the Hadley circulation index in DJF. Regression shows increases of TCO up to 0.8 DU particularly in the Himalayas, the northeast Pacific, North America, and Northern Africa. The Hadley impact is independent from ENSO because the Hadley index used for this study does not correlate with the Niño3.4 index (r = 0.1).

We discuss the cause of change in TCO associated with Hadley circulation. Figure 3.11b also presents regression coefficient of TCO transported from the stratosphere. The regression coefficient shows positive anomalies (up to 0.6 DU) in the Himalayas, the northeastern Pacific, North America, and Northern Africa. The positive anomalies reach from 250 hPa to surface (Figure 3.11c). Additionally, Figure 3.11d presents climatology and regression coefficient of zonal mean vertical

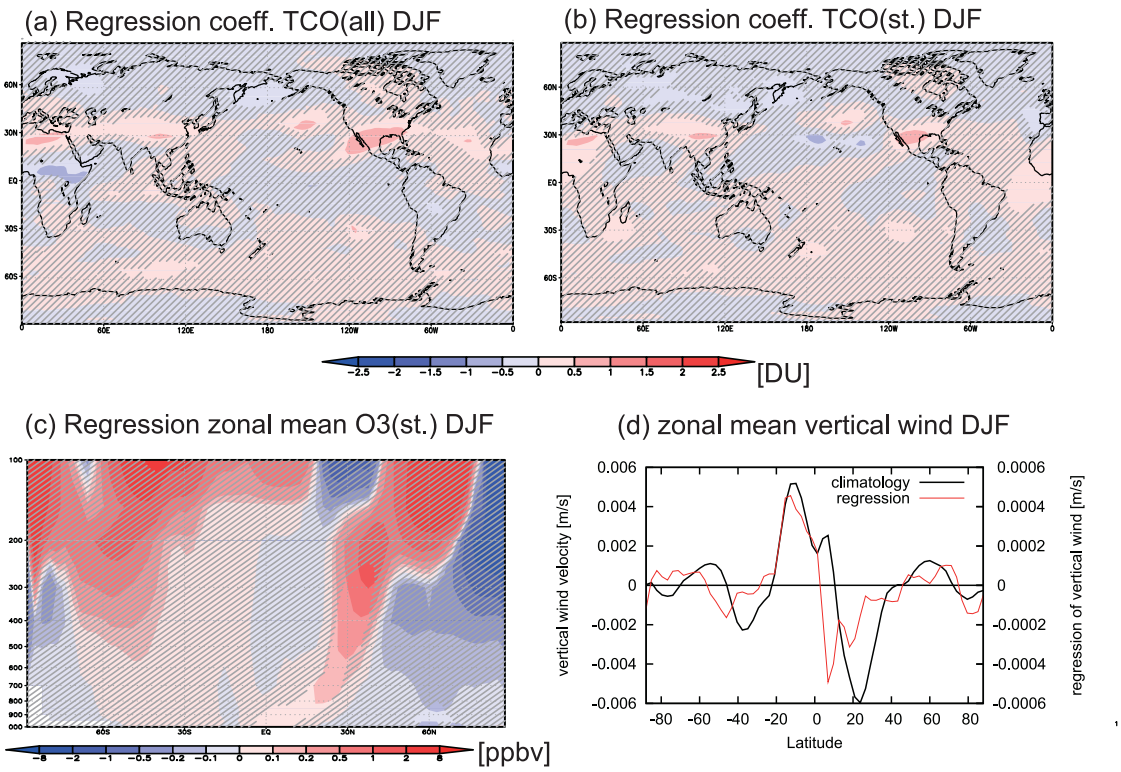

Figure 3.11. (a) Regression coefficient of TCO, (b) TCO transported from the stratosphere with respect to the Hadley circulation index (DU). (c) Regression of zonal mean ozone from the stratosphere with respect to Hadley circulation index (ppbv). (d) Climatology and regression coefficient of vertical wind velocity (m/s) at 300 hPa. The coefficient is calculated using TCO, ozone, or wind velocity and the index in DJF. Hatched regions are not significant at the 95% confidence level. Black and red lines respectively show climatology and regression coefficient in Figure 3.11d.

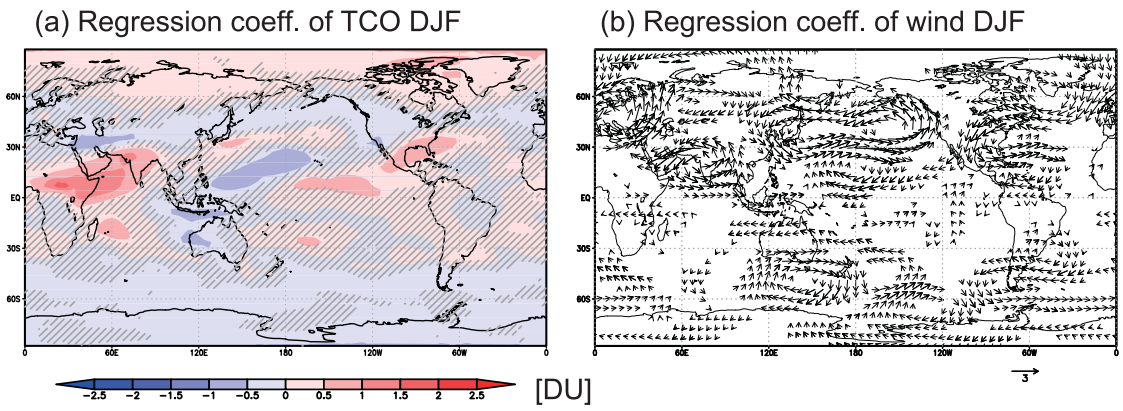

Figure 3.12. Regression coefficient of (a) TCO (DU) and (b) horizontal wind at 400 hPa with respect to the Asian monsoon circulation index. The coefficient is calculated using TCO and the index in DJF. Hatched regions are not significant at the 95% confidence level. Vectors are drawn only in significant region with 95% confidence level.

wind velocity at 300 hPa. The climatology and regression present increase in downward vertical wind velocity between 10°N and 40°N in the upper troposphere. These results suggest that the TCO increase results from enhanced downward transport of ozone-rich air from the stratosphere and upper troposphere to the lower–middle troposphere. However, we need to investigate the reason why the anomalies are significant only in the Himalayas, the northeastern Pacific, North America, and Northern Africa.

3.3.5 Impact of Asian monsoon circulation

In this section, we particularly examine the Asian winter monsoon especially because Asian summer monsoons have a minor impact on TCO (not shown). Figures 3.12a and 3.12b present regression coefficients of TCO and horizontal wind vector at 400 hPa in DJF respectively. The regression shows positive anomaly of 1.2 DU in South Asia and the western Indian Ocean. The change in TCO results from the intensified cyclonic circulation over South Asia associated with monsoon circulation in the upper troposphere (Figure 3.12b). The anomalous circulation enhances transport from Africa to South Asia and the western Indian Ocean. In this study, we also calculated the tagged ozone tracers from various source regions in the simulation fixed to the 1990 chemical field. Results of the simulation suggest that ozone from North Africa (AFN) is most responsible for the TCO increase (about 40% of the increase) in the western Indian Ocean (Figure 3.13). Second most contribution to the TCO increase is ozone from South America (AMS).

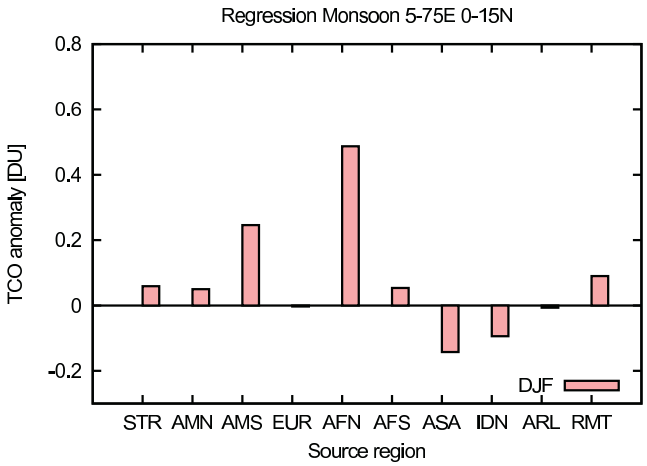

Figure 3.13. Regression coefficient of ozone from each source regions with respect to monsoon index in the western Indian Ocean (0°–15°N, 5°E–75°E). The source regions in the troposphere are shown in Figure 3.1

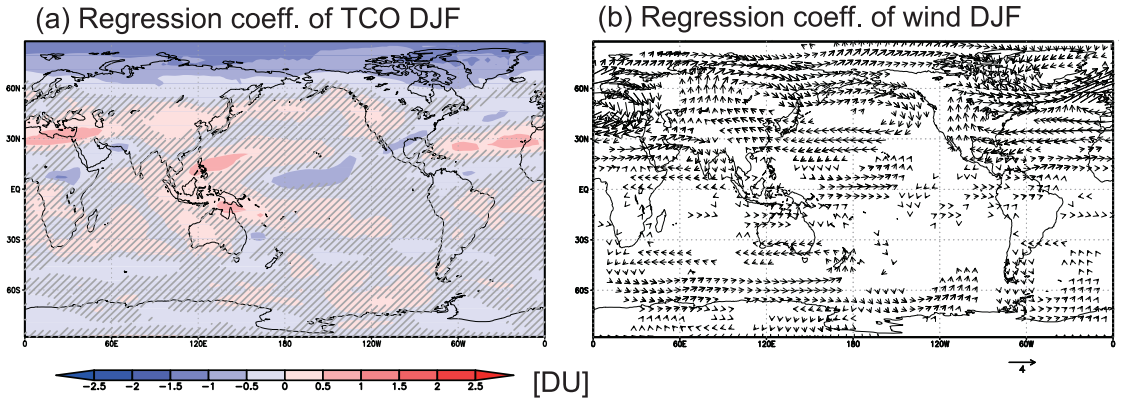

Figure 3.14. Regression coefficients of (a) TCO (DU) and (b) horizontal wind at 500 hPa with respect to the Arctic Oscillation index. The coefficient are calculated using TCO and the index in DJF. Hatched regions are not significant at the 95% confidence level. Vectors are drawn only in the significant region with a 95% confidence level.

3.3.6 Impact of Arctic oscillation

Figure 3.14a shows regression coefficient of TCO with respect to AO index in DJF. Figure 3.14b shows a regression coefficient of horizontal wind at 500 hPa. Wind vectors are drawn in areas with a 95% confidence level. Figure 3.14a shows negative anomaly (1 DU) in the high northern latitudes. This TCO change is qualitatively consistent with previous studies [e.g. Hess and Lamarque, 2007].

The TCO change associated with AO is related to a change in the poleward transport from the northern midlatitude to Arctic. The poleward transport is weakened during the positive phase of AO, resulting from intensified polar vortex (Figure 3.14b). Our tagged ozone simulation suggest that ozone produced in the free troposphere and stratosphere is more responsible for the TCO decrease (about 95%) than that produced in the boundary layer.

3.4 Contribution of meteorological variability to interannual variation in ozone

In this section, we quantify the contribution of major meteorological variability to total interannual variation in global TCO (section 3.4.1) and regional TCO (section 3.4.2).

3.4.1 Contribution to global distribution

We perform EOF analysis to detect the leading mode of interannual variation in global TCO and to quantify its contribution. A result of EOF analysis is shown in Figure 3.15. Figure 3.15a shows time series of EOF first mode (PC1) with the Niño3.4 index in OND. PC1 correlates with that of Niño3.4 index (r = 0.90), suggesting that the first mode represents a component related to ENSO. Spatial patterns of the first mode (EOF1) are also similar to that of the regression coefficient in Figure 3.6a (Figure 3.15b). The spatial correlation coefficient between EOF1 and the regression is 0.98. Contribution of EOF1 to total variance is 33%. Hess and Mahowald [2009] also applied EOF analysis to global ozone field. Although the spatial pattern in our study is similar to that in their study, the contribution to total variance in our study is about five times larger than that in their study. This is attributable to applying EOF to TCO in OND when El Niño is mature phase. The result for DJF is also similar. These results indicate that the variation of TCO associated with ENSO is the most important in all interannual variations of global TCO distribution.

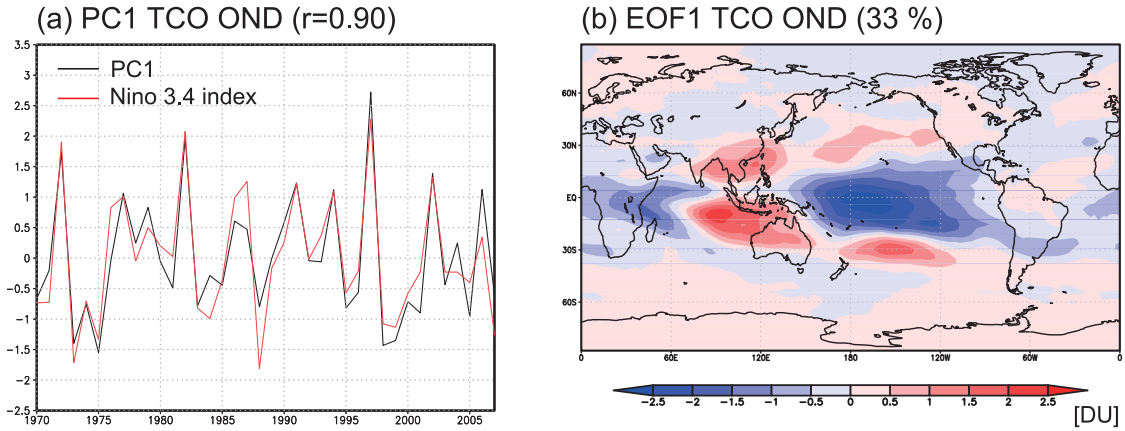

Figure 3.15. Time series corresponding to EOF first mode (EOF1) with Nino3.4 index. The time series are standardized with their +1 standard deviation. EOF1 eigenvector of TCO (DU) averaged for OND. The spatial pattern is scaled by +1 standard deviation of PC1. Its contribution rate is 33%.

3.4.2 Contribution to temporal variation

We quantify the contribution of the meteorological variability to total interannual variation of TCO in six regions. We quantify the contribution as an index of meteorological variability multiplied by the corresponding regression coefficient at each grid and year. For example, ENSO impact is given as

$$C_{ENSO}(x, y, t) = a_{ENSO}(x, y) \times I_{ENSO}(t) \tag{3.5}$$

where C is contribution of ENSO, a stands for regression coefficient of ENSO, I denotes Niño3.4 index, x, y, and t are longitude, latitude, and year respectively. We also constructed total contribution by adding contributions of ENSO, IOD in OND, and by adding ENSO IOD, Hadley, Asian monsoon, and AO in DJF. Figure 3.16 shows correlation coefficients between the total contribution and the simulated TCO. Figure 3.16a shows significant correlation in the eastern Pacific in the tropics, the western Pacific including Indonesia. Figure 3.16b also shows the significant correlation in the southern North America and the northern high latitude as well as tropical eastern Pacific and northwestern Indian Ocean. There is, however, no significant correlation in the Atlantic, East Asia, and Europe. We focus on the six regions where the correlation coefficient is larger than 0.6 (Figure 3.16). The simulated TCO and the contribution of meteorological variability in the right panels of Figures 3.17 and 3.18 are detrended to emphasize year-to-year variation.

Figure 3.17a shows the interannual variation of simulated and satellite-observed TCO in OND in the tropical eastern Pacific. The simulated variation agrees well with the observed variation, except in the late 1980s, although the model overestimates the observed long-term trend. Overes-

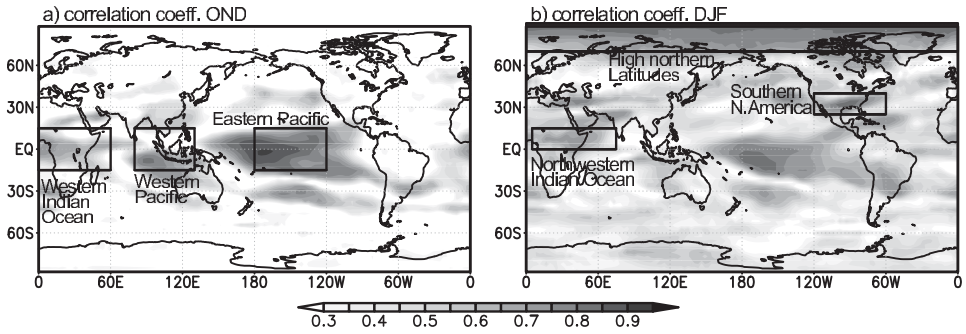

Figure 3.16. Correlation coefficient between the simulated TCO and total contribution of meteorological variability considered in this study, and map of regions used inFigures 3.17 and 3.18 for (a) OND and (b) DJF.

timation of the long-term trend might be attributable to increasing trend in ozone precursor emissions in the tropics after 1990 in the model. Figure 3.17b presents detrended TCO variation with the anomalies calculated from the Niño3.4 index (hereinafter, the ENSO component). The ENSO component, explaining 79% of the total variance (r = 0.89), is most responsible for the variation in the tropical eastern Pacific. In strong El Niño years (1982 and 1997), the ENSO component contributed more than 68% to TCO anomalies there.

Figure 3.17c shows simulated and observed TCO anomaly in the tropical western Pacific and Indonesia. These anomalies are shown as deviations from average value during whole observation period. The average, however, does not include the value in 1997, because the simulation in this study does not include emission enhancement during the severe Indonesian fires in 1997. The model generally captures interannual variation, while the long-term trend is overestimated as in Figure 3.17a. Figure 3.17d portrays detrended TCO anomalies in addition to the anomalies calculated from the Niño3.4 index and DMI as in Figure 3.17b (ENSO and IOD component, respectively). In this region, both the ENSO and IOD components play important roles in the interannual variation of TCO. They contributed more than 84% of the TCO increase in 1982 and 1997. The quantities of relative importance of the ENSO and IOD components were 56% and 44%, respectively, in 1982, and were 35% and 65% in 1997. We, however, need to pay attention to possible double counting of ENSO and IOD, because of the significant correlation between Niño 3.4 index and DMI. In other El Niño years, TCO changes are not explained merely by ENSO and IOD. This results from interannual variation in ozone above 5 km, which might be related to changes occurring in the upper tropospheric circulation over Indonesia.

Interannual variation of TCO in the tropical western Indian Ocean in OND is shown in Figure 3.17e. The satellite observation and the simulation show similar variations, especially after 1996. The simulated increasing trend is overestimated after 1990 as in the tropical Pacific. Figure 3.17f

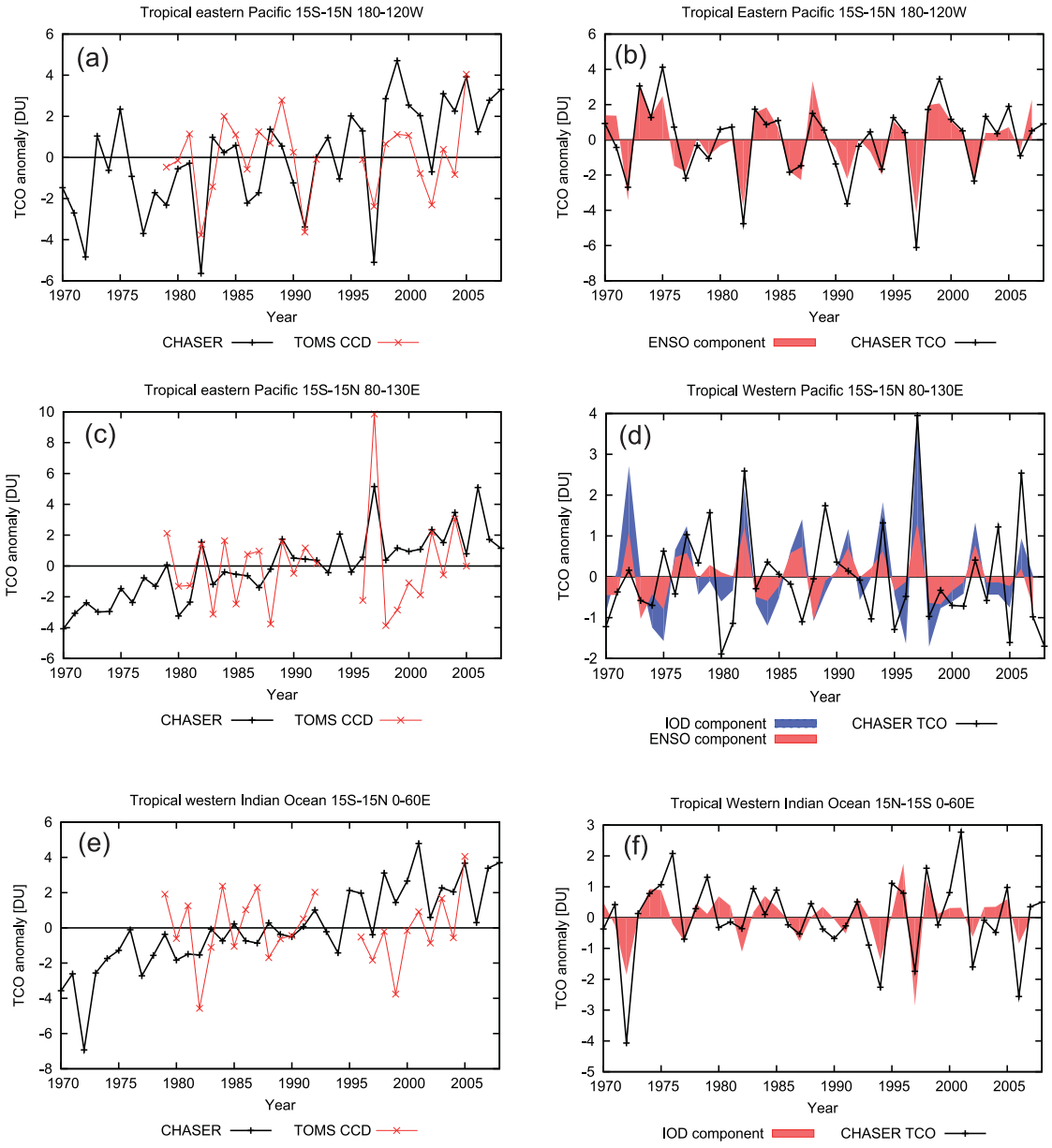

Figure 3.17. Time series of TCO (DU) in (a, b) the tropical eastern Pacific, (c, d) the tropical western Pacific, and (e, f) the tropical western Indian Ocean averaged for October?December. Figures 3.17a, 3.17c, and 3.17e show the simulated (black) and the observed (red) TCO. Observation data are derived using the TOMS convective cloud differential method in the tropics. Figures 3.17b, 3.17d, and 3.17f show the simulated TCO (black line) and the contribution of climate variability (red and blue) calculated from the regression coefficient and the corresponding index. The time series are calculated from the whole simulation period and are detrended to emphasize year-to-year variation rather than long-term change.

presents detrended anomalies that are simulated and calculated from DMI (IOD component). IOD explains 36% of TCO variation in the tropical western Indian Ocean. The variation after 1992 is particularly influenced by IOD significantly.

Figure 3.18a shows interannual variation of TCO in the northwestern Indian Ocean in DJF. The simulated variation reproduces satellite-observed variation well during 1998–2008. The model, however, overestimates the observed trend. Figure 3.18b presents the simulated TCO anomalies, and the anomalies calculated from Asian monsoon index (monsoon component). During 1999–2008, the simulated variation is influenced strongly by interannual variation in Asian monsoon circulation (Figure 3.18b). The average contribution of the monsoon component is approximately 50%. However, the monsoon component has less impact on variation of TCO in the late 1980s and early 1990s. In addition, IOD has a non-negligible impact on TCO in the northwestern Indian Ocean in DJF.

We compare the simulated TCO variation with the observation by ozonesonde (Boulder, Huntsville, and Wallops Island) in southern North America (Figure 3.18c) because no long-term satellite observation is sufficient to evaluate the simulated interannual variations in ozone over North America. The variation shown in Figure 3.18c is averaged only at the observation sites and for the days when ozonesonde was launched. The model reproduces increasing trend in TCO well. Interannual variation of TCO is generally captured by the model, in particular, between the early 1980s and the late 1990s. In this region, the ENSO component has significant impacts on TCO variation during El Niño events (Figure 3.18d). The contributions of ENSO were 70% in 1973, 58% in 1983, and 46% in 1998. Additionally, the Hadley component has a non-negligible impact in the region.

Figure 3.18e shows interannual variation of the simulated TCO with ozonesonde observations (Alert, Eureka, Ny-Aalesund, Thule, and Resolute) in the high northern latitudes in DJF, as in Figure 3.18c. The simulated TCO variation captures the observation well after 1985. A positive trend is also reproduced by the model. Figure 3.18f shows that the AO component explains 72% of the variance (r = 0.85). In strong positive and negative phase years of AO (1989 and 1977), its respective contributions are 110% and 77% of the total anomaly.

3.5 Summary

This chapter characterizes the interannual variation of global tropospheric ozone associated with meteorological variability during 1970–2008. The CHASER model generally reproduces the main features of the observed distribution and interannual variation observed by TES in late 2000s. Parts

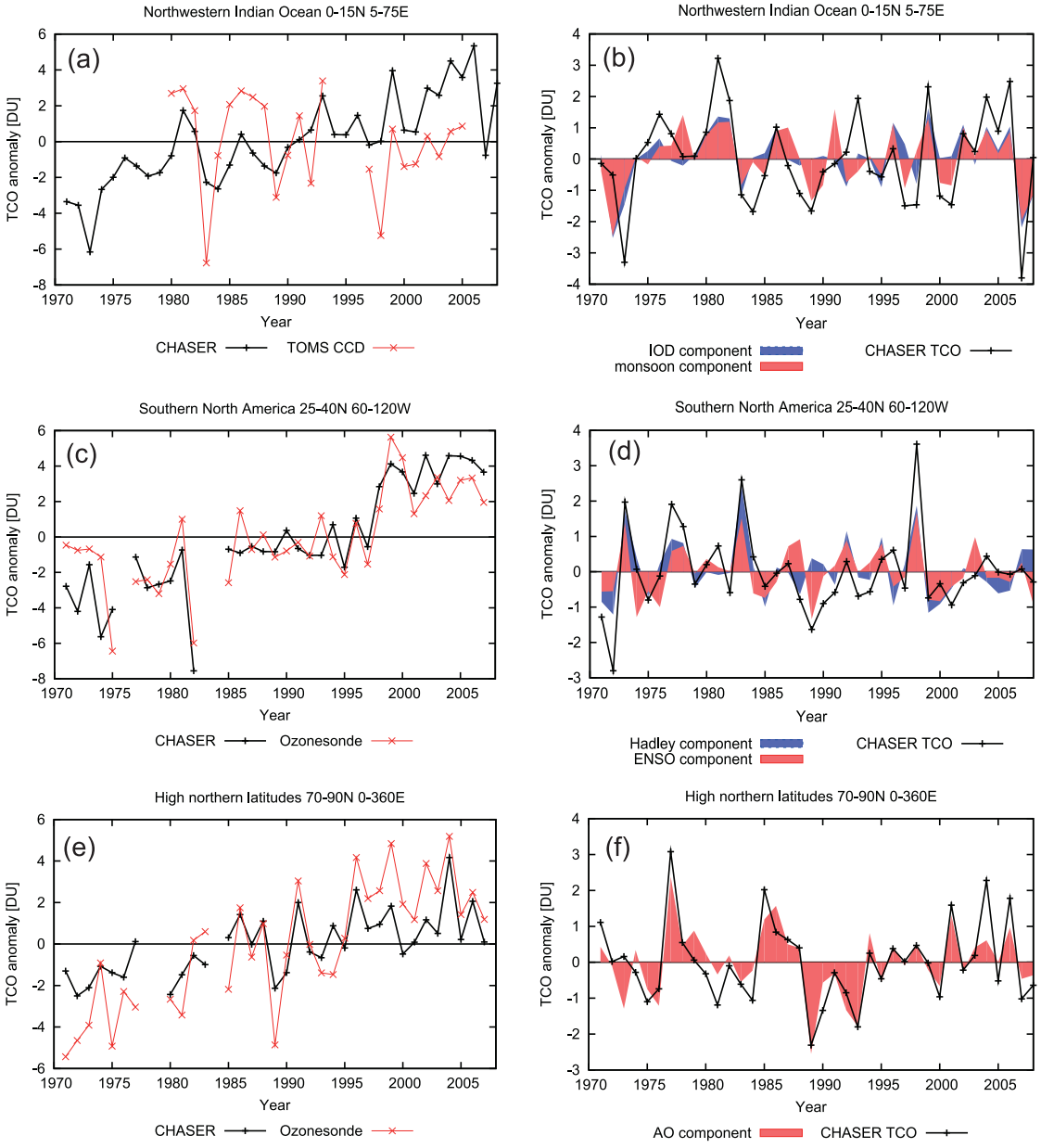

Figure 3.18. Same as Figure 3.17, but for TCO in (a, b) the northwestern Indian Ocean, (c, d) the southern North America, and (e, f) the high northern latitudes. Observation data are derived from ozonesonde (Figures 3.18c and 3.18e) in the middle to high northern latitudes. The simulated TCO shown in Figures 3.18c and 3.18e are sampled at closest time to the observation.

of simulated and observed interannual variation are explainable by ENSO, IOD variability, and AO.

We investigated changes in TCO spatial patterns associated with ENSO, IOD variability, interannual variation in Hadley circulation, interannual variation in Asian monsoon circulation, and AO using linear regression analysis. The change associated with ENSO shows a dipole structure, which is positive anomaly (1–1.5 DU) in the western Pacific including Indonesia and negative anomaly (2.5 DU) in the eastern Pacific in OND. This pattern is consistent with those found in previous studies [Peters et al., 2001; Doherty et al., 2006; Oman et al., 2011]. The model also exhibits a TCO increase (0.5–1.5 DU) in the central to eastern Pacific over the subtropics during the positive phase of ENSO. The increase extends to southern North America with a 2-month lag (from 0.2 in OND to 1 DU in DJF). Additionally, we investigated the meteorological impact of ENSO more quantitatively. Sudo and Takahashi [2001] reported that key factors controlling ozone changes caused by meteorological change are large-scale atmospheric circulation, convection, and water vapor changes in the tropics. We further quantified the impact of atmospheric circulation and convection changes (transport), and the impact of water vapor changes (chemistry). Results show that transport has a dominant impact on the most of globe, while those of transport and chemistry are comparable in the tropical central Pacific. The pattern of TCO change induced by IOD variability shows a dipole structure, which is increased (1.5–2 DU) in the west of 90°E with a decrease (1–1.5 DU) in the east during the positive phase of IOD. The mechanism causing the changes is analogous to ENSO because meteorological changes associated with IOD variability resemble those of ENSO.

Intensified Hadley circulation causes TCO increase (up to 0.8 DU) in the Himalayas, the northeastern Pacific, and North America in DJF. The increase is probably linked to enhanced downward transport from stratosphere and upper troposphere to the lower–middle troposphere. Stronger Asian monsoon circulation enhances TCO (1.2 DU) in the western Indian Ocean because of anomalous eastward transport of ozone from Africa. In the years of AO positive phase, TCO is decreased (1 DU) in the high northern latitudes, reflecting weakened poleward transport from midlatitudes. Transport process plays dominant roles in the TCO variation associated with interannual variation in Hadley circulation, interannual variation in Asian monsoon circulation, and AO.

Finally, we quantify the contribution of meteorological variability to total interannual variation in global and regional TCO distributions. The result suggests that interannual variation in TCO in the tropics and the high northern latitudes are generally explainable by ENSO, IOD, AO, and interannual variation in Asian monsoon circulation. ENSO explains 33% of global TCO variance and 79% of the variance in the tropical eastern Pacific in OND. In years of strong El Nino events (1982,

1997), ENSO contributed more than 68% to negative anomalies. In the tropical western Pacific and Indonesia, both ENSO and IOD play important roles in OND. Their combinations contributed more than 84% to positive anomalies in the strong El Nino years. The relative importance of ENSO (IOD) is 56% (44%) in 1982, and is 35% (65%) in 1997. ENSO also contributes to 46–70% of the increase in southern North America for DJF in 1973, 1983, and 1998. Hadley circulation has a non-negligible impact in DJF there. In the tropical western Indian Ocean and Africa, IOD explains 36% of the variance in OND. The interannual variation of TCO in the northern Indian Ocean is influenced strongly by Asian monsoon circulation in DJF after late 1990s. Its average contribution is about 50%. AO dominates the interannual variation of TCO in the high northern latitudes in DJF. It explains 72% of the variance, and contributes 110% (77%) of anomalies in the strongest positive (negative) phase year of AO.

In this chapter, our simulation does not incorporate year-to-year variation in natural sources of ozone precursors (e.g., emission from wildfire, soil, vegetation) to evaluate meteorological impact on ozone apart from these emissions. However, these emissions can also be important factors controlling interannual variation in ozone. In future work, we must investigate the interannual variability of global tropospheric ozone more comprehensively, including changes in these emissions. In addition, ENSO and AO might provide a preview of future warming climate in the tropics and the northern mid-high latitude [Yamaguchi and Noda, 2006]. Further investigation of variation in ozone associated with them is necessary for testing changes in ozone under global warming.

Chapter 4

Evaluation of chemistry–climate model

4.1 Introduction

Chemistry–climate model (CCM), which a general circulation model coupled with atmospheric chemical processes, is a frequently-used tool for a future projection of stratospheric and tropospheric ozone. Chemical transport model (CTM), which is used in chapter 3, calculates only chemical field. In contrast, CCM simulates chemistry, radiation, dynamics, and their interactions. For a reliable future projection, CCM needs to calculate the processes relevant to future change in ozone accurately. Climate change can have a non-negligible impact on future change in stratospheric and tropospheric ozone [Eyring et al., 2010b; Kawase et al., 2011]. It is necessary to validate the response of ozone to CCM-driven meteorological variability. Additionally, emissions of tropospheric ozone precursors and ODSs is expected to be reduced in the next century [WMO, 2011; van Vuuren et al., 2011]. The reduced emissions can cause a substantial change in ozone in the troposphere and stratosphere. Therefore, evaluation of the ozone response to change in the emissions is important.

For evaluation of ozone responses to meteorology, examining of ozone variation associated with El Niño Southern Oscillation (ENSO) is often used [Oman et al., 2011; 2013]. ENSO is regarded as a dominant mode of interannual variation in tropospheric ozone [Peters et al., 2001; Doherty et al., 2006; Hess and Mahowald, 2009]. As shown in chapter 3 and Sekiya and Sudo [2012], ENSO impact on tropospheric ozone is greater than those of other meteorological variability. This chapter compares the simulated ENSO-related variation in stratospheric and tropospheric ozone with that observed by satellite instruments and ozonesonde. During the 1980s and 2000s, the increased emissions of tropospheric ozone precursors and ODSs have a significant impact on stratospheric and tropospheric ozone [Fusco and Logan, 2003; Gillett et al., 2011]. To evaluate the ozone response to a change in the emissions, we evaluate the change in ozone during the 1980s and 2000s

with satellite and ozonesonde observation.

Moreover, we test sensitivities of the ENSO-related variation and the change in ozone to increased horizontal resolution through ozone transport (i.e. an impact of horizontal resolution on wind field and advection calculation) apart from chemistry using the model with two horizontal resolutions (about 300 km and 120 km). Therefore this study does not consider an impact of horizontal resolution change on non-linearity of tropospheric ozone chemistry. Earlier studies typically used CCMs with about 300 km horizontal resolution. However, it remains unclear whether such CCM resolution simulates the variation and change appropriately.

This chapter is organized as follows. Section 4.2 provides the experimental settings and observational data. In section 4.3, we compare the present-day simulation with observation and reanalysis data. To validate the response of ozone to CCM-driven meteorological variability, we evaluate the simulated ENSO-related ozone variation during 2004–2009 by comparison with that derived from satellite and ozonesonde observations (section 4.4). To evaluate the ozone response to a change in the emissions of tropospheric ozone precursors and ODSs, we assess the long-term change in ozone during the 1980s and 2000s (section 4.5). In section 4.6, we summarize the results in this chapter.

4.2 Methodology

4.2.1 Experimental settings

We performed time-slice runs for the 1980s and the 2000s, which mean an average state in the years around 1980 and 2000 respectively. We compared the time-slice run for the 2000s with satellite and ozonesonde observations. The time-slice runs are also used to evaluate change in stratospheric and tropospheric ozone between the 1980s and 2000s. A transient run for the period during 2004–2009 is also performed. We evaluate ENSO-related variation in stratospheric and tropospheric ozone during 2004–2009 in the transient run. To obtain boundary conditions (chemical production and loss rate of O_x family, N_2O, CH_4, and CFCs) for the O_3-tracer-transport model, we conducted simulations using the AGCM version with T42 resolution (hereinafter FC). Subsequently, we performed simulations using the O_3-tracer-transport version with T42 and T106 resolutions (hereinafter MTT and HTT respectively). In this study, we refer respectively to T42 and T106 as medium and high horizontal resolution. The simulation settings used for this study are presented in Table 4.1.

We conducted the time-slice FC simulations for the 1980s and the 2000s. Their lengths are five

Table 4.1. Summary of experiment performed in this study.

Full-chemistry simulation (FC)

Period	SST/SIC	GHGs/ODSs/Emissions
1980s (5yr)	HadISST[1]	Historical (1980)
2000s (5yr)	HadISST[2]	Historical (2000)
2004–2009	HadISST	Historical (2000)

O_3-tracer-transport simulation

Experiment	H. resolution	Period	SST/SIC	P, β
MTT	T42	1980s (5yr)	HadISST[1]	1980s
		2000s (7yr)	HadISST[2]	2000s
		2004–2009	HadISST	2004–2009
HTT	T106	1980s (5yr)	HadISST[1]	1980s
		2000s (7yr)	HadISST[2]	2000s
		2004–2009	HadISST	2004–2009
MTT-fCHEM	T42	1980s (5yr)	HadISST[1]	2000s
		2004–2009	HadISST	average for 2004–2009

[1)] Average for 1975–1984
[2)] Average for 1995–2004

years in the each period following Zeng et al. [2008]. We specified the concentrations of greenhouse gases (GHGs) and ODSs in 2000 [Meinshausen et al., 2011], and the emissions of tropospheric ozone precursors in 2000 [Lamarque et al., 2010] as the boundary conditions for the 1980s and the 2000s Table 4.1). The average of HadISST data [Rayner et al., 2003] for 1975–1984 and for 1995–2004 are respectively used as the SST/SIC for the 1980s and the 2000s. The biogenic emissions of isoprene and terpenes estimated by Guenther et al. [1995] is respectively reduced by 20% to 400 Tg C/year and 100 Tg C/year following Houweling et al. [1998] and Roelofs and Lelieveld [2000]. We used the monthly mean climatology of biogenic emissions because this study examines a combined impact of anthropogenic and biomass burning emissions and climate change on stratospheric and tropospheric ozone. The initial conditions were taken from the result of ACCMIP experiment for the corresponding period using MIROC-ESM-CHEM [e.g. Lamarque et al., 2013].

We conducted the time-slice MTT simulations for the 1980s and the 2000s. The simulations ran for five and seven years respectively in the 1980s and the 2000s. The P, β, and GHGs (N_2O, CH_4, and CFCs) were prescribed by the output obtained from the time-slice FC simulations (Table 4.1). The other settings are same as the time-slice FC simulations. Additionally, we performed the simulation which calculates the ozone tendency attributable to transport and dry deposition in the 1980s with the P and β in the 2000s (hereinafter MTT-fCHEM). To assess a sensitivity of the change in ozone to the change in horizontal resolution, we performed the time-slice HTT simulations for the 1980s and the 2000s. Their lengths are five and seven years respectively in

the 1980s and the 2000s. The boundary and initial conditions for HTT simulations were linearly interpolated from those for the MTT simulations.

We also conducted the transient FC, MTT, and HTT simulations during 2004–2009 with the SST/SIC in the corresponding year (Table 4.1). The other settings are same as those of the time-slice simulations for the 2000s. This study also performed the transient MTT-fCHEM simulation which maintained the P and β at the average for 2004–2009, and allowed the ozone tendency because of transport and dry deposition to vary among years. However, the P and β for the MTT-fCHEM simulation include diurnal and seasonal cycles.

4.2.2 Observation data

We used the data derived from Microwave Limb Sounder (MLS) and Tropospheric Emissions Spectrometer (TES) instruments for the evaluation of stratospheric and tropospheric ozone in the model. The MLS/TES data were constructed following Oman et al. [2013]. MLS level 2 ver. 3.3 data were used for ozone above 261 hPa. The data were screened using the quality and convergence threshold recommended by Livesey et al. [2011]. We used TES level 3 ver. 2 monthly mean data for ozone below 261 hPa. TES ozone profiles have about two degrees of freedom for signals in the troposphere [e.g. Worden et al., 2004]. The MLS and TES data were mapped into the model grid. Oman et al. [2013] used the MLS data from August 2004 to May 2012 and the TES data from September 2004 to December 2009 because the frequency of TES observations was decreased after January 2010. However, we used the data from September 2004 to December 2009, when both MLS and TES are available. In this study, the averaging kernels of MLS and TES were not applied to the simulated ozone.

We also used ozonesonde data for the comparison with the simulations for the 2000s (Section 3), we applied the ozonesonde data compiled by Tilmes et al. [2012], which are climatological data of 42 selected stations for 1995–2011. We also used the monthly mean data at Samoa, Java, and Hilo for 2004–2009 obtained from Southern Hemisphere ADditional OZonesondes (SHADOZ) [Thompson et al., 2003a;b; 2007] for the evaluation of the simulated variation in ozone associated with ENSO (Section 4.4).

We evaluate change in the modeled ozone during the 1980s and 2000s with merged ozone data (MOD) total ozone based on version 8 SBUV and TOMS [Stolarski and Frith, 2006], and an updated global ozone data set derived from SAGE I+II data plus polar ozonesondes [Randel and Wu, 2007]. We compare the difference of the simulated ozone between the 1980s and 2000s with a linear trend of the observed total column ozone and ozone mixing ratio. We excluded the

data during 1992–1995 to calculate the linear trend, because the data during this period is largely influenced by the Pinatubo eruption.

4.3 Evaluation of Present-day simulation

We first compare ozone and meteorology in the simulation for the 2000s with those in the observation data and the re-analysis data before investigating the ENSO-related variation and the long-term change. The model results in the last five years are used for the comparison. We compare the zonal means of simulated temperature and zonal winds with those in the ERA-Interim re-analysis data [Dee et al., 2011]. We use an average of the ERA-Interim for 1995–2004. The simulated ozone volume mixing ratio is compared with the MLS/TES data and the ozonesonde observations. The MLS/TES data are averaged for 2005–2009.

Figure 4.1a shows annual and zonal means of the simulated temperature for the MTT simulation (contour), and biases relative to the ERA-Interim (shade). The MTT generally reproduces temperatures in the ERA-Interim, although a warm bias (up to 6 K) is apparent in the lower stratosphere. The MTT also shows a cold bias of 8 K near the extratropical tropopause. A similar cold bias is also found in the original version of MIROC-ESM-CHEM [Watanabe et al., 2011b]. The reason for this cold bias is related to the short wave heating in the model. In the HTT simulation, the warm bias of temperature in the lower stratosphere is reduced by 4 K compared to that in the MTT (Figure 4.1b), although the reduction is probably related to dynamical process. The HTT shows a slight warm bias in the troposphere, except near the extratropical tropopause.

We examine the vertical mass flux at 100 hPa surface. The flux is often used for estimating stratosphere–troposphere exchange of mass and ozone in the extratropics [e.g. van Noije et al., 2004]. Table Table 4.2 presents a summary of vertical mass flux at 100 hPa in ERA-Interim, MTT and HTT simulations. The fluxes are integrated in the tropics ($20^\circ S$–$25^\circ N$), the northern and the southern extratropics ($90^\circ S$–$20^\circ S$ and $25^\circ N$–$90^\circ N$). Boundaries between the tropics and the extratropics are defined as the latitude where the flux in ERA-Interim is equal to zero. Although MTT simulation underestimates absolute values of vertical mass flux at 100 hPa relative to ERA-Interim (19–23$\%$) in all regions, the flux in HTT is comparable to that in the ERA-Interim.

We examine the vertical mass flux at 100 hPa surface. The flux is often used for estimating stratosphere–troposphere exchange of mass and ozone in the extratropics [e.g. van Noije et al., 2004]. Table 4.2 presents a summary of the vertical mass flux at 100 hPa in the ERA-Interim, the MTT, and the HTT simulations. The fluxes are integrated in the tropics (20°S–25°N), the northern

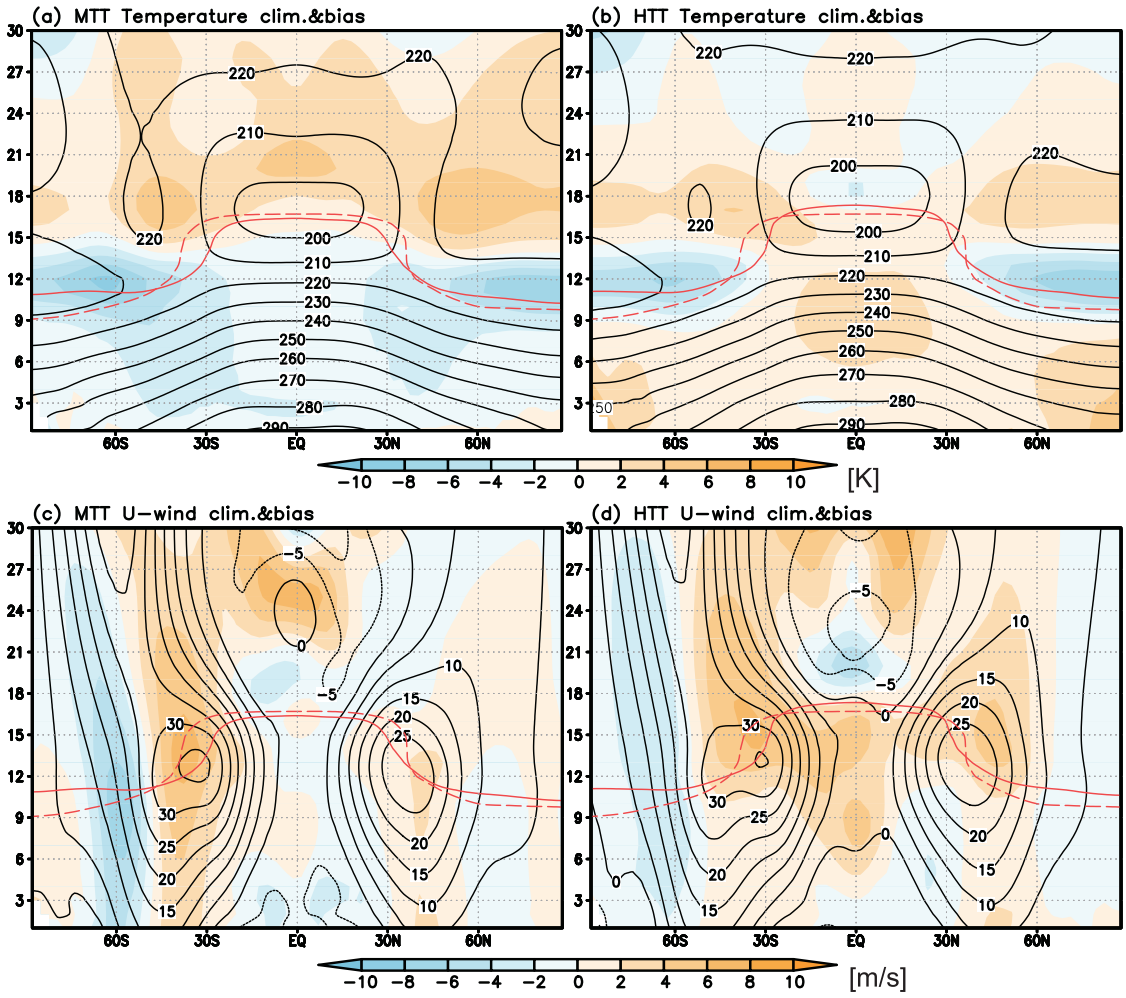

Figure 4.1. Annual and zonal means of temperatures (K) and zonal winds (m/s) and their biases relative to ERA-Interim. Top and bottom panels respectively show temperatures (a, b) and zonal winds (c, d). Left is MTT simulation and right is HTT. Contours and shading respectively represent the mean field and its bias.

Table 4.2. Vertical mass and ozone (in parentheses) flux at 100 hPa. The positive sigh is upward flux. The top four rows are an average for the 2000s, and the bottom four rows are regression or partial regression coefficients with respect to Niño3.4 index. Unit of the mass flux is 10^6 Tg/yr for the average and is 10^6 Tg/yr/K for ENSO-related variation. Unit of the ozone flux is Tg/yr for the average and is Tg/yr/K for the ENSO-related variation. The range is defined as a two-side 95% confidence interval for the ENSO-related variation.

	90°S–20°S	20°S–25°N	25°N–90°N
Climatology			
ERA-Interim	−199.2 (−223.7)	422.6 (102.3)	−223.4 (−360.3)
MTT	−153.0 (−238.0)	335.0 (89.0)	−180.0 (−333.8)
HTT	−207.6 (−294.3)	422.5 (103.3)	−214.6 (−381.2)
ENSO-related variation			
ERA-Interim	-17.6 ± 6.0 (-16.7 ± 4.3)	37.0 ± 10.7 (3.1 ± 5.2)	-19.3 ± 5.3 (-24.8 ± 17.2)
MTT	-3.2 ± 4.6 (0.9 ± 14.2)	14.6 ± 3.9 (-0.7 ± 2.5)	-11.4 ± 4.7 (-11.2 ± 4.3)
HTT	-13.4 ± 1.1 (-9.5 ± 10.0)	17.4 ± 1.6 (-2.2 ± 2.6)	-4.0 ± 11.6 (-1.2 ± 39.2)

and the southern extratropics (90°S–20°S and 25°N–90°N). The boundaries between the tropics and the extratropics are defined as the latitude where the flux in the ERA-Interim is equal to zero. Although the MTT simulation underestimates the absolute values of the vertical mass flux at 100 hPa relative to those in the ERA-Interim (19–23%) in all latitude bands, the flux in the HTT is comparable to those in the ERA-Interim.

The vertical mass flux at 100 hPa in the HTT simulation is greater than that in the MTT. This is mainly attributable to a difference of wave drag between the MTT and the HTT. The difference is, at least partly, related to a difference of zonal means of zonal winds between the MTT and the HTT. The upper flanks of the subtropical jet in the HTT are stronger than those in the MTT (Figures 4.1c and 4.1d). Critical layer, which leads to a wave breaking and drag, occurs where the phase velocity of a wave matches the background wind velocity. Therefore, the stronger subtropical jet implies that the critical layer in the HTT is higher than that in the MTT. Shepherd and McLandress [2011] showed that a wave drag change attributable to climate change is largely explainable by an upward shift of the critical layer associated with the acceleration of the upper flanks of the subtropical jet.

We compare ozone in the simulations with that in the MLS/TES observation. Figure 4.2a shows the annual and zonal mean of ozone in the MLS/TES observation averaged for the period from 2005 to 2009. General feature of the observed distribution is reproduced by the MTT and HTT simulations (contour in Figures 4.2c–d). Figures 4.2c–d also shows the differences between

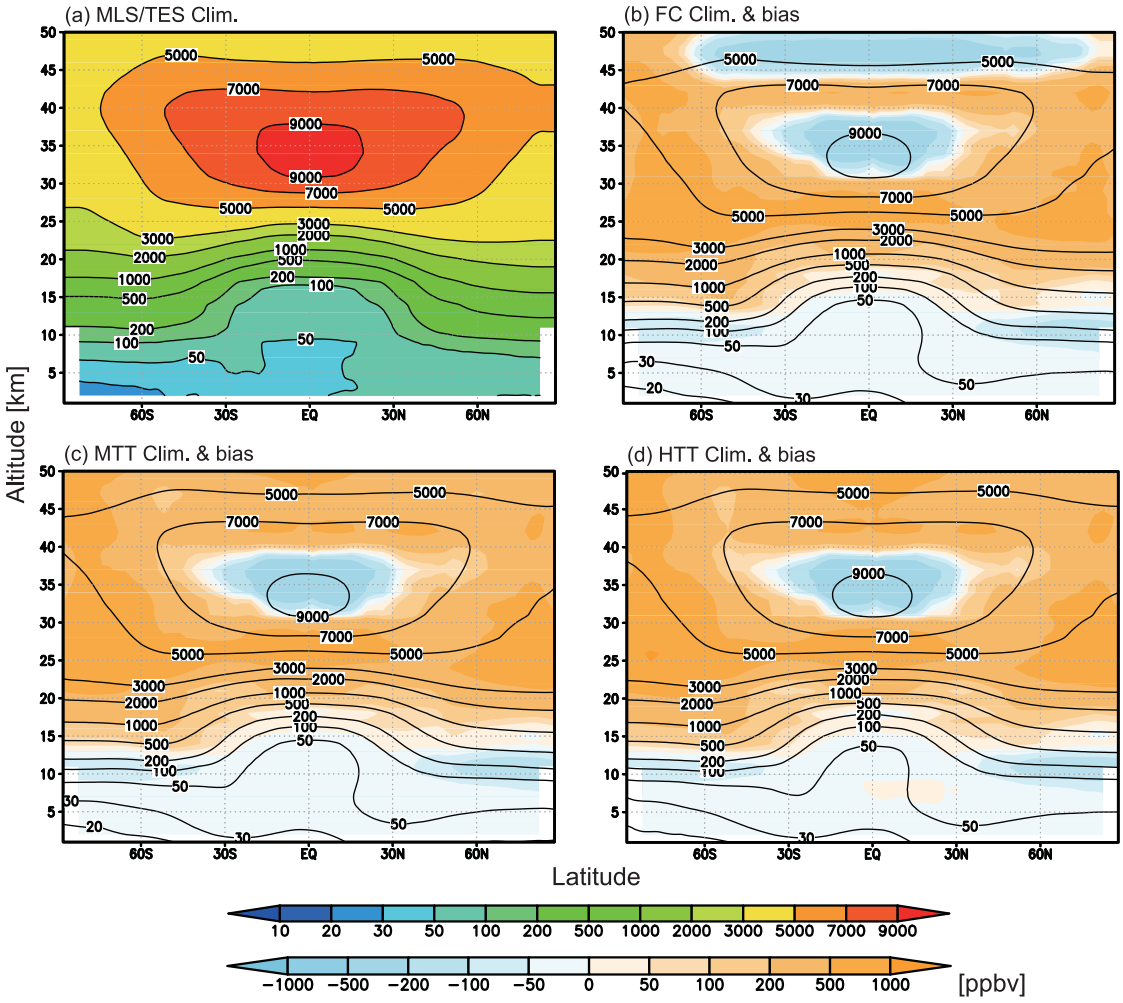

Figure 4.2. Annual and zonal mean of ozone (ppbv). (a) The mean value during the period from 2005 to 2009 observed by the MLS/TES instruments. (b–d) The mean in the simulations for the 2000s (contour) and its bias relative to that derived from the MLS/TES instruments (shade). (b), (c), and (d) are respectively the FC, the MTT, and the HTT simulations.

the observed and the simulated ozone in the stratosphere and troposphere. The difference is within 10% in the middle and upper stratosphere (1–20 hPa). However, the simulated ozone in the lower stratosphere is high-biased to that in the MLS/TES observation (10–30% in 20–50 hPa and 30–60% in 50–200 hPa). In contrast, the simulated ozone in the middle troposphere is low-biased (15–40%).

Figures 4.3a–d show biases of ozone in the simulations and the MLS/TES observation relative to that in the ozonesonde observation. The each panel of Figure Figure 4.3 shows the average of all available profiles at the stations, which are located in the corresponding latitude band. The ozone profiles in the simulations and the MLS/TES observation are sampled at the closest grid to the station. Although the bias of ozone observed by the MLS/TES is within 10% compared to that observed by the ozonesonde in the stratosphere, it is high-biased by 50% in the troposphere. The

simulated ozone in the MTT is high-biased to that in the ozonesonde by 30% above 50 hPa, and the simulated ozone shows the positive bias larger than 50% in the altitudes between the tropopause and 50 hPa. The bias in the lower stratosphere exceeds the annual mean of ± 1 standard deviation for each month over the all soundings in the ozonesonde observation. The bias near the tropopause is attributable to the simulated tropopause height which is lower than the observed one, because such large bias near the tropopause in the MTT is not found on the height coordinate relative to the tropopause (Figure 4.4). In contrast, the tropospheric ozone in the simulations is low-biased to that in the ozonesonde by 30%. The simulated tropospheric ozone in the HTT is similar to that in the MTT in the extratropics. In the tropics, tropospheric ozone in the HTT is larger compared to that in the MTT (Figure Figure 4.3b, c). The increase reduces the bias in the southern tropics, although it raises the bias in the northern tropics. Because the results of the MTT simulation are generally similar to those of the FC simulation (Figures 4.2b and 4.3), we show only the results of the O_3-tracer-transport simulations hereinafter.

The comparison between the MLS/TES and the ozonesonde observations suggests the positive bias in the MLS/TES for the middle–upper troposphere (Figure 4.3). The positive bias of tropospheric ozone derived from the MLS/TES is larger than that reported by Nassar et al. [2008]. They reported that mean difference of all profiles, which meet the criteria for the coincide observation of TES and ozonesonde, is generally in the 0–15% range for the troposphere. Their validation of TES was performed using the TES observation which coincides with the ozonesonde observation. However, we use all available profiles for the comparison, because we aim to validate the climatological mean of stratospheric and tropospheric ozone in the simulations with those in the satellite and ozonesonde observations. We show the MLS/TES data averaged for 2005–2009, and show the ozonesonde data averaged for 1995–2011.

We also calculate the vertical ozone flux at 100 hPa using the ERA-Interim wind field and the MLS ozone field, and compare with the simulated vertical ozone flux. Table 4.2 presents a summary of the flux in the tropics and the extratropics in the same manner of the mass flux. In the tropics, the MTT simulation underestimates the upward ozone flux calculated from the ERA-Interim and the MLS by 13%. The HTT improves the underestimation. In the extratropics of the northern hemisphere, the MTT underestimates the calculated downward ozone flux (7.4%), although the HTT overestimates it (5.8%). In the extratropics of the southern hemisphere, the MTT and the HTT overestimate the calculated ozone flux (6.4% and 31.6%, respectively). The MTT underestimates the mass flux at 100 hPa in the ERA-Interim, and the HTT agrees with the mass flux in the ERA-Interim. The overestimation of the simulated ozone at 100 hPa is responsible for

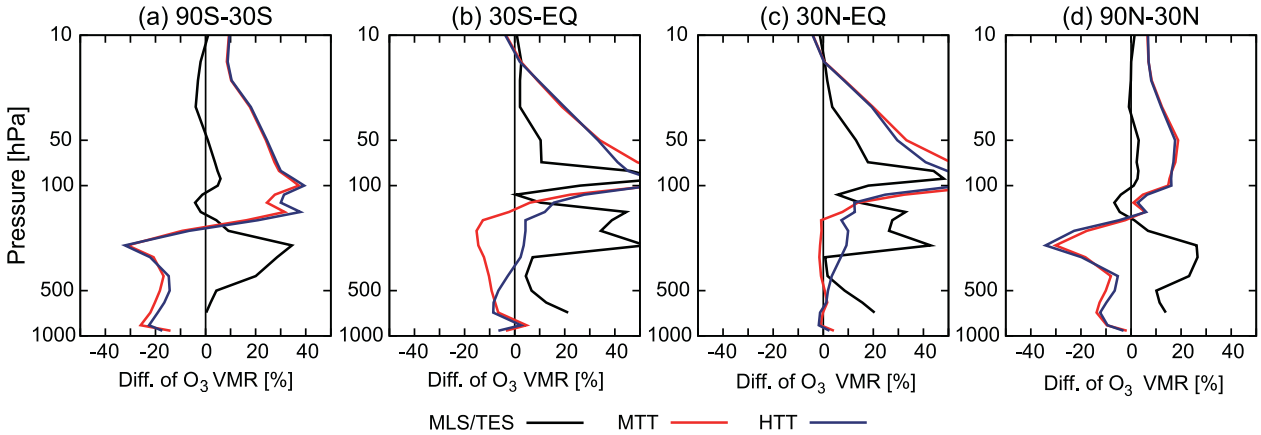

Figure 4.3. Biases of ozone in the MLS/TES measurements and the simulations relative to that in the ozonesonde observations (%) for the 2000s. The each panel shows the average of all available profiles in (a) 90°S–30°S, (b) 30°S–Eq., (c) Eq.–30°N, and (d) 30°N–90°N. Black cross shows the MLS/TES observation averaged for 2005–2009. Green dashed-dotted line, red solid line, and blue dotted line respectively show the simulated ozone in the FC, the MTT, and the HTT simulations for the 2000s. The black dashed line indicates an annual mean of standard deviation for each month over the all soundings. The MLS data is used above horizontal thin line, and the TES data is used below it. The ozonesonde data averaged for 1995–2011 are compiled by Tilmes et al. [2012].

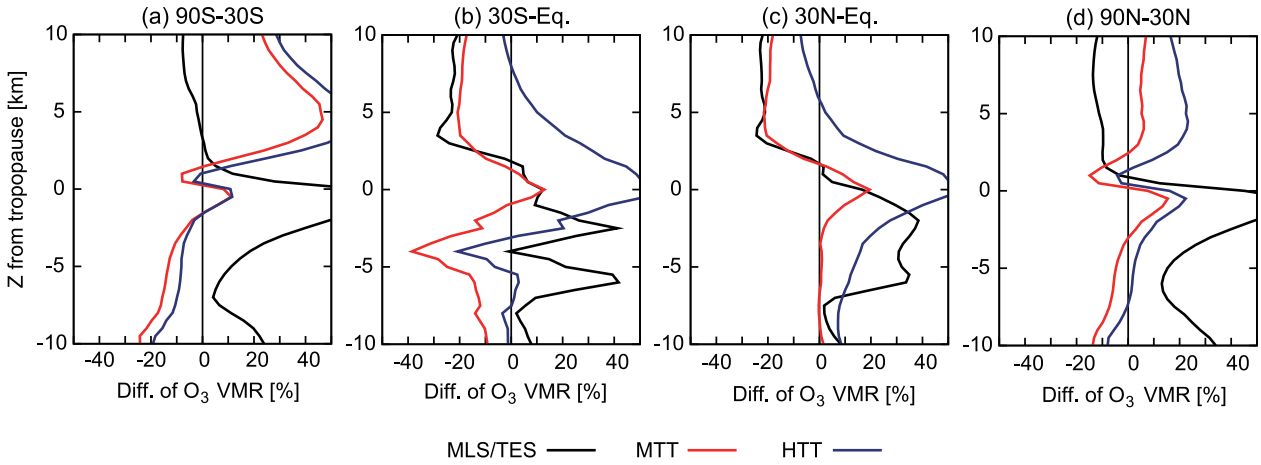

Figure 4.4. Biases of MLS/TES and simulated ozone relative to ozonesonde observations (%) on height coordinates relative to that in the tropopause. Each panel shows averages of all available profiles in (a) 90°S–30°S, (b) 30°S–Eq., (c) Eq.–30°N, and (d) 30°N–90°N. Black line shows the MLS/TES observations averaged for 2005–2009. Red and blue lines respectively represent ozone in the MTT and the HTT. The black dashed line indicates an annual mean of standard deviation for each month over the all soundings. The ozonesonde data averaged for 1995–2011 are compiled by Tilmes et al. [2012].

the overestimation of the ozone flux at 100 hPa.

4.4 ENSO-related variation

This study evaluates ENSO-related ozone variation in the simulations forced by the observed SST variability with that derived from the MLS/TES instruments and the SHADOZ ozonesonde network. The observed variation related to ENSO is found by Randel and Thompson [2011] and Oman et al. [2011; 2013]. Additionally, we test the sensitivity of the ozone variation to increased horizontal resolution using the simulations with medium (about 300 km) and high (about 120 km) resolutions. The interannual variability of ozone in the lower stratosphere is influenced by the quasi-biennial oscillation (QBO) as well as ENSO [e.g. Randel and Wu, 2007; Oman et al., 2013]. Therefore, we used multiple linear regression (MLR) analysis to assess the ENSO-related variation in ozone in the MLS/TES observation and the HTT simulation as

$$C(t) = \sum_i a_i X_i(t) + \varepsilon(t). \tag{4.1}$$

Therein, C is an anomaly of ozone, a represents the partial regression coefficient, X denotes indices of ENSO and QBO, and ε stands for a residual term. Niño3.4 index is used as Index of ENSO. The Niño3.4 index is calculated from the HadISST data. Two orthogonal time-series based on EOF analysis of zonal wind at equator are used as QBO indices [Wallace et al., 1993; Randel and Wu, 1996]. The QBO indices for the MLS/TES and the HTT is respectively calculated from zonal wind field in the ERA-Interim and the HTT. Linear regression analysis is applied for the MTT, because the MTT simulation does not internally generate QBO. This analysis method is similar to that used in Oman et al. [2011; 2013].

We analyze the simulation during 2004–2009 in order to evaluate the simulated ozone variation related to the observed SST variability during the same period as that of the observation. However, the simulation length is shorter than that in the previous studies [e.g. Doherty et al., 2006; Oman et al., 2011; 2013]. We present three month running mean of Niño3.4 index, the anomaly of ozone in the MTT and the HTT simulations (Figure 4.5). In the MTT and the HTT simulations, the simulated anomaly of ozone is well correlated with Niño3.4 index at 3 km and 12 km altitude in the tropical eastern Pacific. The correlation coefficients are -0.79 (-0.84) in the MTT, and -0.76 (-0.83) in the HTT at 3 (12) km altitude. The ozone anomaly in the regions follows Niño3.4 index during the positive phase of ENSO, the difference between the anomaly and the index stands out during the negative phase of ENSO. The month-to-month variability also causes the difference.

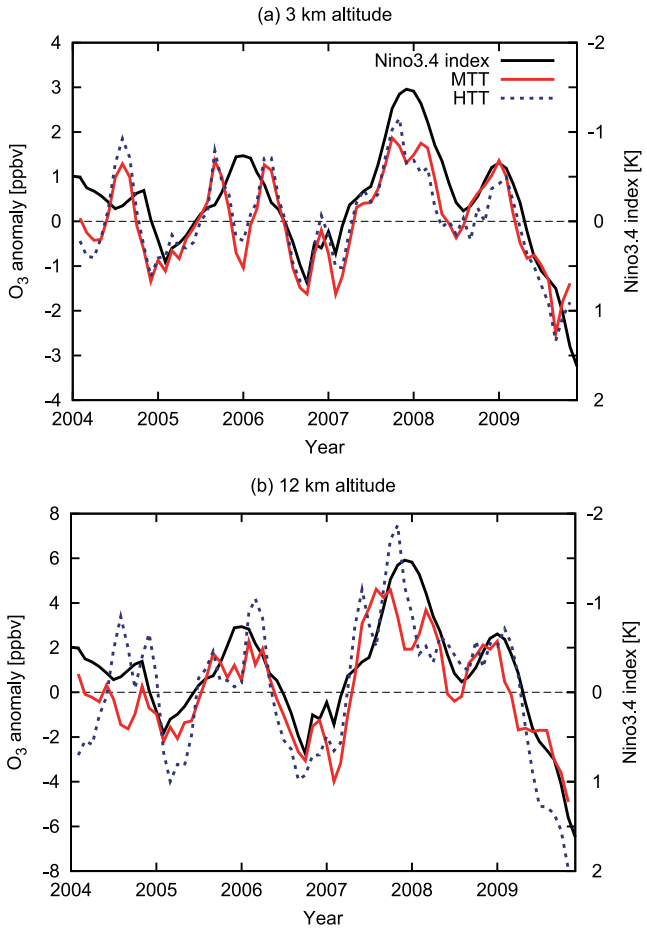

Figure 4.5. Three month running mean of Niño3.4 index (K) and O_3 anomaly (ppbv) in the MTT and the HTT simulations averaged in the tropical eastern Pacific (180°–240°E, 15°S–15°N). (a) is at 3 km altitude and (b) is at 12 km altitude. Black line is Niño3.4 index, red line is the anomaly in the MTT, and blue line is the anomaly in the HTT. The left and right y-axes are respectively for the anomaly of ozone and Niño3.4 index. The right y-axis is reversed.

Figure 4.6a presents the partial regression coefficient of ozone observed by the MLS/TES with respect to Niño3.4 index averaged in the tropics (15°S–15°N). The MLS/TES shows a positive anomaly over Indonesia and Indian Ocean. Local peaks of the anomaly are located at 80°E and at 14 km altitude (up to 5 ppbv/K), and at 100°E in the altitudes between 5 and 10 km (up to 3 ppbv/K). A negative anomaly of about 2 ppbv/K is found in the middle troposphere over the central and eastern Pacific. The anomaly reaches 10 ppbv/K near the tropopause. The regression coefficient of ozone in the MTT shows a similar spatial pattern to that in the MLS/TES (Figure 4.6b). However, the MTT simulation underestimates the magnitude of the observed anomalies. The HTT simulation generally shows a spatial pattern of the anomalies similar to that in the MTT, although the HTT simulation partly improves the underestimation in the central and eastern Pacific. However, the anomaly over Indonesia and the Indian Ocean is underestimated in the MTT and the HTT, because the monthly mean emission from biomass burning in 2000 is used in the simulations during 2004–2009. In the tropical lower stratosphere, the observed and the modeled variation in ozone show a negative anomaly of approximately 20 ppbv/K. The spatial pattern of the variation in tropospheric ozone in our model is similar to that in HadAM3-STOCHEM [Doherty et al., 2006] and GEOSCCM [Oman et al., 2013], despite of their different simulation periods. The simulation periods are six years (2004–2009) in this study, twenty three years (1980–2002) in Doherty et al. [2006], and twenty five years (1985–2009) in Oman et al. [2013].

The difference of the anomalies between the MTT and the HTT simulations is attributable to transport process, because the simulations prescribed same chemical production and loss rate of O_x. One reason for the difference is the different response of Walker circulation to the observed SST variability. We calculate the sensitivity of Walker circulation to the observed SST variability using the Southern Oscillation Index (SOI) as a proxy of Walker circulation, and compare with the sensitivity of SOI obtained from NOAA CPC (http://www.cpc.ncep.noaa.gov/data/indices/). We defined the sensitivity as a linear regression coefficient of SOI with respect to Niño3.4 index. The sensitivities are 0.53 ± 0.29 K^{-1} in the MTT, 0.72 ± 0.23 K^{-1} in the HTT, and 0.88 ± 0.22 K^{-1} in the observation. The range of the sensitivities is a two-side 95% confidence interval. These sensitivities indicate that Walker circulation in the HTT is more sensitive to the observed SST variability than that in the MTT. The sensitivity in the MTT is out of the range of the observed sensitivity, although that in the HTT is within the range of the observed sensitivity.

In the eastern Pacific, positive anomalies are apparent in the MLS/TES observation and the simulations in the 12–20 km altitude over the subtropics and the midlatitudes (Figure 4.7). The positive anomalies in the MTT simulation (about 10 ppbv/K) are weaker than those in the MLS/TES

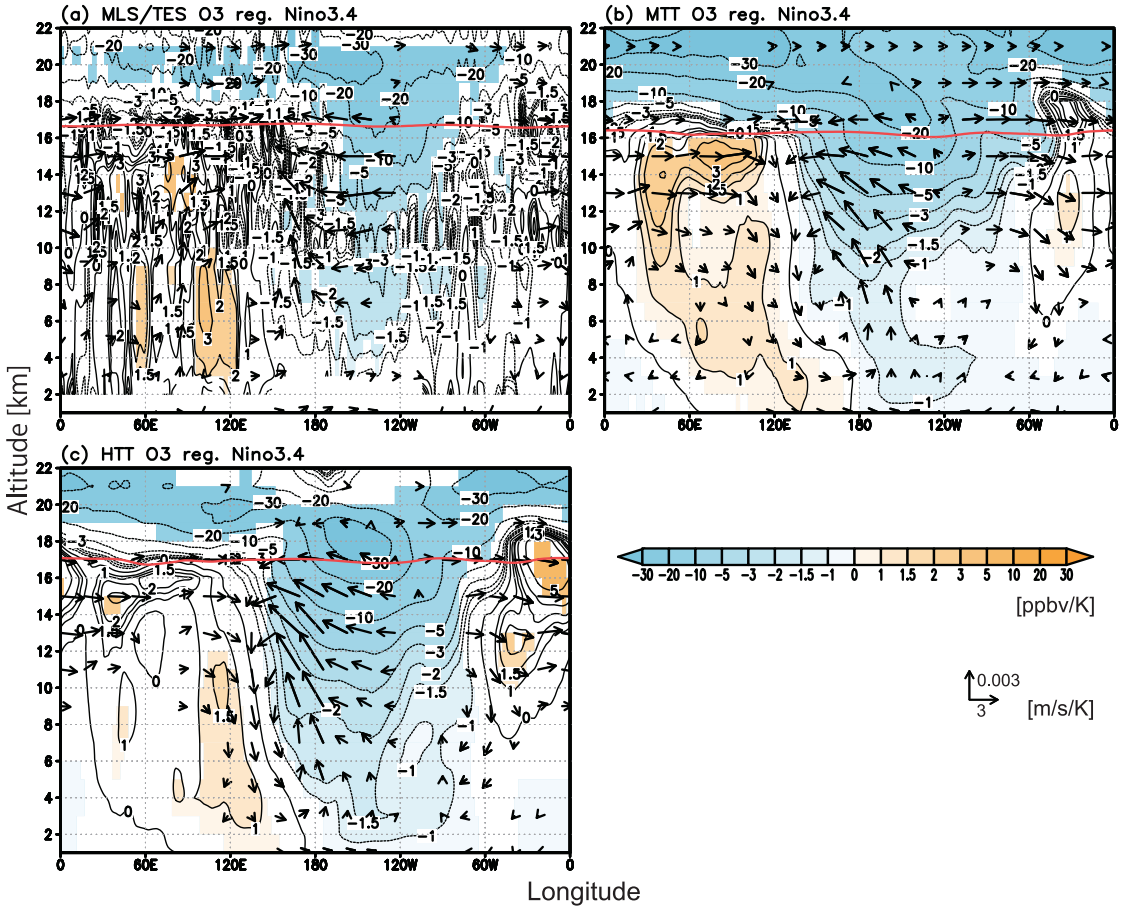

Figure 4.6. Regression and partial regression coefficients of ozone (ppbv/K) and wind field (m/s/K) with respect to Niño3.4 index averaged in the tropics (15°S–15°N) during 2004–2009. The shaded regions show a significant ozone variation at a 95% confidence level. Arrows indicate a wind field variation at a 95% confidence level: (a) is the partial regression coefficient in the MLS/TES observation (ozone) and the ERA-Interim (wind); (b) is the regression coefficient in the MTT; and (c) is the partial regression coefficient in the HTT. The vertical component of wind is scaled by 1000. Red line is the tropopause height, which is defined by temperature lapse rate of 2 K/km. The tropopause height in the left panel is calculated from the ERA-Interim.

(about 50 ppbv/K) especially in the northern hemisphere, although the anomalies in the HTT are comparable to those in the MLS/TES. The simulated positive anomalies extend to the low to middle troposphere over the subtropics (0.5–1 ppbv/K). The simulated anomalies are in agreement with the observed anomalies. These anomalies are slightly weaker than those in GEOSCCM (2–3 ppbv/K in the low to middle troposphere, and 10–15 ppbv/K near the tropopause shown in Figure 4b of Oman et al. [2013]). The anomalies can result from enhanced transport of Asian pollution and increased stratosphere–troposphere exchange of ozone during El Niño [Langford et al., 1998; Hsu et al., 2005; Zeng and Pyle, 2005; Koumoutsaris et al., 2008; Voulgarakis et al., 2011], reflecting intensified subtropical jet, and enhanced local Hadley and Brewer–Dobson circulation [Shapiro et al., 2001; Wang, 2002; Calvo et al., 2010]. The enhanced meridional circulation is also shown in Figure 4.7 as arrows. A negative anomaly is also found in the tropics in the MLS/TES and the simulations. As with Oman et al. [2013], the modeled negative anomaly is narrower in latitude than the observed anomaly in the tropical troposphere. The HTT improves the tropical negative anomaly in the middle troposphere compared to that in the MTT.

We also investigate the zonal mean response of temperature and ozone to ENSO. Figure 4.9 shows the temperature regression and partial regression coefficients with respect to Niño3.4 index. In the tropical troposphere, the ERA-Interim, the MTT, and the HTT show a positive anomaly, although the simulations overestimate the anomaly in the ERA-Interim. In contrast, a negative anomaly of 0.4 K/K is found in the tropical lower stratosphere in the ERA-Interim. The simulations also show the negative anomaly of 0.2 K/K in the MTT and 0.6 K/K in the HTT. Over 30°–60°N and S, positive anomalies are found in the lower stratosphere. The model underestimates the observed positive anomaly of 0.6 K/K in the northern hemisphere. The difference between the MLS/TES and the simulations is attributable to the weak anomalous descent in the lower stratosphere of northern midlatitude. The spatial pattern of the anomalies of temperature in this study is similar to the SAGE and ozonesonde observations and the simulation with WACCM [Randel et al., 2009; Randel and Thompson, 2011].

Regarding zonal mean of ozone, the MLS/TES and the simulations show a negative anomaly in the tropical lower stratosphere, and positive anomalies in the midlatitude lower stratosphere (Figure 4.10). In the tropical lower stratosphere, the simulated negative anomaly in the MTT and the HTT is comparable to the observed one (20–30 ppbv/K). However, the simulated positive anomaly above 18 km altitude over 30°–60°N (about 5 ppbv/K in the MTT and 10 ppbv/K in the HTT) underestimate the observed one (about 50 ppbv/K). In 12–18 km altitude over 30°–60°S, the HTT reproduces the positive anomaly of approximately 5 ppbv/K derived from MLS/TES, although

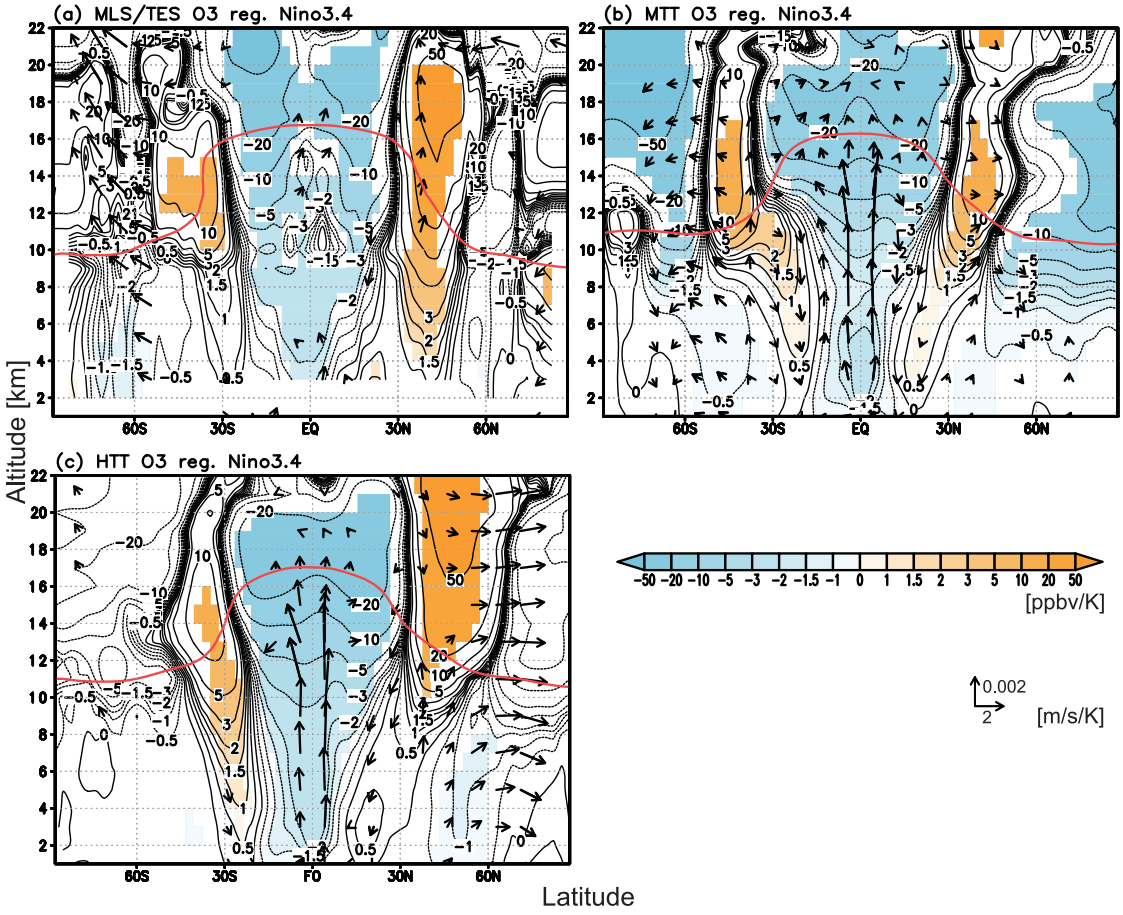

Figure 4.7. Regression and partial regression coefficients of ozone (ppbv/K) and wind field (m/s/K) with respect to Niño3.4 index averaged in the eastern Pacific (180°–230°E) during 2004–2009. The shaded regions show a significant ozone variation at a 95% confidence level. Arrows indicate a wind field variation at a 95% confidence level: (a) is the partial regression coefficient in the MLS/TES observation (ozone) and the ERA-Interim (wind); (b) is the regression coefficient in the MTT; and (c) is the partial regression coefficient in the HTT. The vertical component of wind is scaled by 1000. Red line is the tropopause height. The tropopause height in the left panel is calculated from the ERA-Interim.

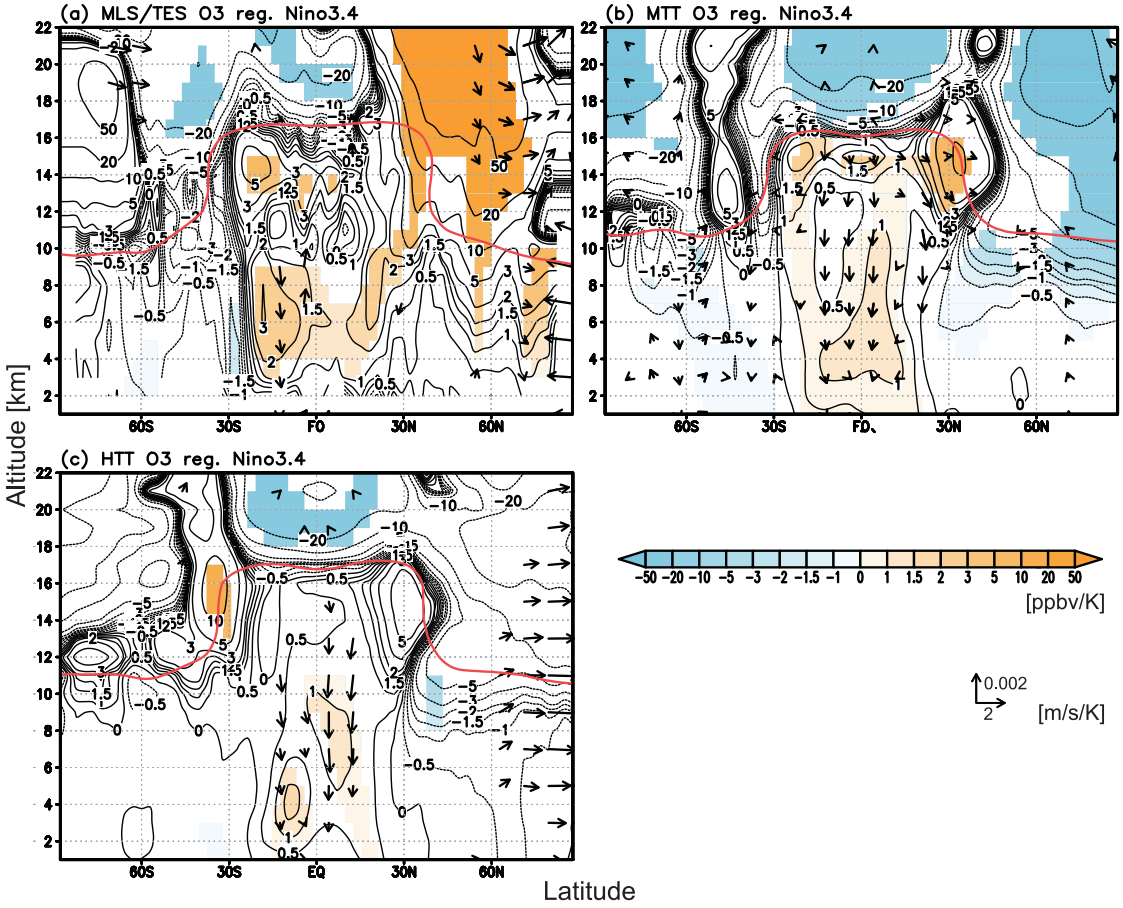

Figure 4.8. Regression and partial regression coefficients of ozone (ppbv/K) and wind field (m/s/K) with respect to Nino3.4 index in the western Pacific (90°E–120°E) during 2004–2009. Shaded regions show significant ozone variation at a 95% confidence level. Arrow indicates wind field variation at a 95% confidence level: (a) is the partial regression coefficient obtained from the MLS/TES observation (ozone) and the ERA-Interim (wind); (b) is the regression coefficient in the MTT; and (c) is the partial regression coefficient in the HTT. The vertical component of wind is scaled by 1000. Red line is the tropopause height. The tropopause height in the left panel is calculated from the ERA-Interim.

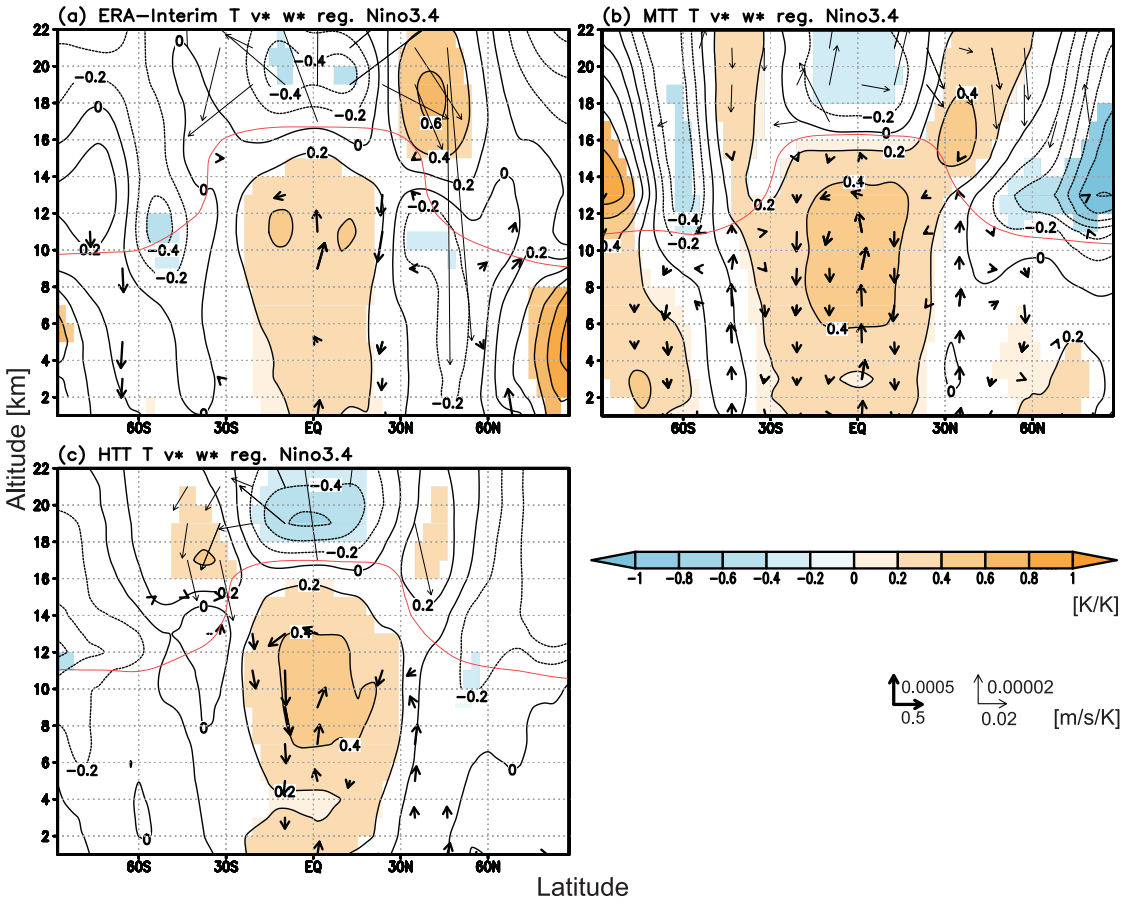

Figure 4.9. Zonal means of regression and partial regression coefficients of temperatures (K/K) and residual circulation (m/s/K) with respect to Niño3.4 index during 2004–2009. The shaded regions show a significant temperature variation at a 95% confidence level. Arrows indicate a wind field variation at a 95% confidence level: (a) and (c) respectively stand for the partial regression coefficient in the ERA-Interim and the HTT simulation; (b) is the regression coefficient in the MTT. The vertical component of residual circulation is multiplied by 1000. The scale of thin arrow is 25 times larger than that of thick arrow. Red line is the tropopause height. The tropopause height in the left panel is calculated from the ERA-Interim.

the MTT underestimates it slightly. Randel et al. [2009] and Randel and Thompson [2011] also analyzed the SAGE and ozonesonde observations and the simulation with WACCM. This study shows the regression coefficient of -2.5–3% per standardized Niño3.4 index in the tropical lower stratosphere, and the regression coefficients of 0.6–1.2% per standardized Niño3.4 index in the midlatitude lower stratosphere. However, the regressions are weaker than those in Randel et al. [2009] and Randel and Thompson [2011].

Additionally, we compare the ENSO-related variation in the MLS/TES and the simulations with that in the ozonesonde observation during 2004–2009 in the tropical Pacific. This evaluation is similar to that in Oman et al. [2011], which used the observation in the two western region SHADOZ

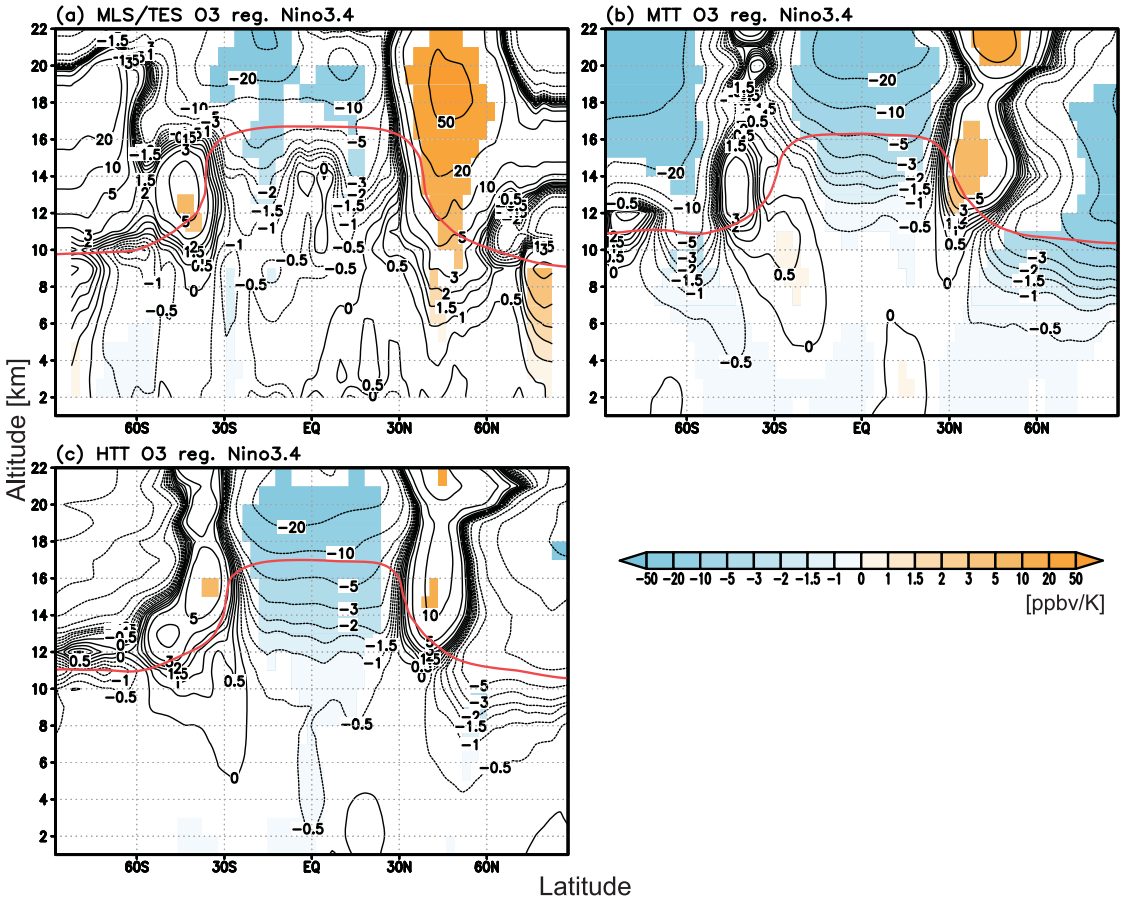

Figure 4.10. Zonal means of regression and partial regression coefficients of ozone (ppbv/K) with respect to Niño3.4 index during 2004–2009. The shaded regions show a significant ozone variation at the 95% confidence level: (a) and (c) respectively denote the partial regression coefficients in the MLS/TES observation and the HTT simulation; (b) is the regression coefficient in the MTT. Red line is the tropopause height. The tropopause height in the left panel is calculated from the ERA-Interim.

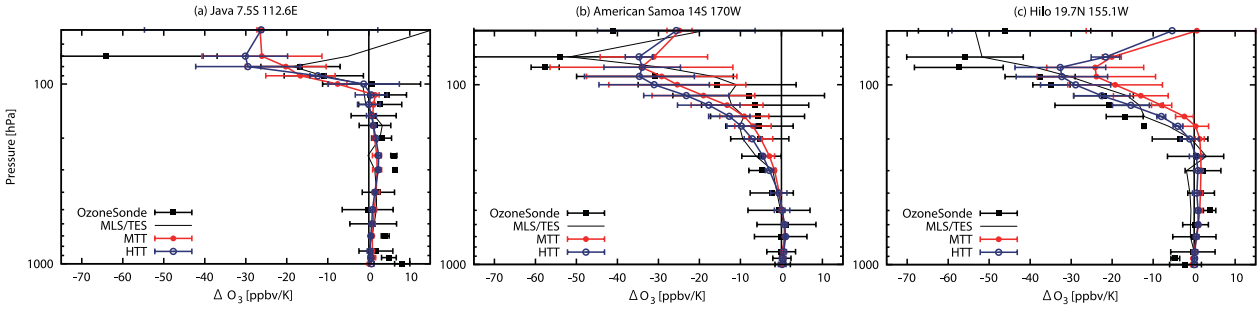

Figure 4.11. Regression and partial regression coefficients of ozone with respect to Niño3.4 index (ppbv/K) at (a) Java, (b) Samoa, and (c) Hilo during 2004–2009. Black squares and line respectively stand for the partial regression in the ozonesonde and the MLS/TES observations. Red line shows the regression in the MTT. Blue one is the partial regression in the HTT. The error bar represents a range of a two-side 95% confidence interval.

locations (Java and Kuala Lumpur) and the three eastern region SHADOZ locations (Samoa, Hilo, and San Cristobal) for 1998–2009. At Java, the simulations, the satellite and the ozonesonde observations show ozone increase in the troposphere (Figure 4.11a). However, the simulations slightly underestimate the increase observed by the ozonesonde observation. At Samoa, the observed and the simulated ozone are decreased, although the simulated ozone underestimates the observed one in the middle troposphere (Figure 4.11b). At Hilo, the simulations and the ozonesonde observation show a positive anomaly in the middle troposphere and a negative anomaly in the upper troposphere (Figure 4.11c). The HTT simulation partly improves the underestimation of the negative anomaly in the upper troposphere. In the tropical lower stratosphere, a negative anomaly of about 40 ppbv/K is observed at all stations. The simulations tend to underestimate the observed negative anomaly (10–34 ppbv/K). The vertical profile of the regression coefficient with respect to Niño3.4 index in this study is similar to that in Oman et al. [2011].

Table 4.2 shows ENSO-related variation in the vertical mass flux at 100 hPa. During the positive phase of ENSO (El Niño), increases in upward and downward mass fluxes are seen, respectively, in the tropics and the extratropics. The change in the simulated fluxes is, however, underestimated compared to the fluxes in the ERA-Interim. The MTT simulates the flux change stronger than that in the HTT in the northern extratropics, although the difference is within the range of the two-side 95% confidence interval. In the southern extratropics, the MTT simulates the flux change weaker than that in the HTT, and the difference exceeds the range. In the tropics, the HTT simulates the change in the flux slightly larger than that in the MTT. We estimate the vertical ozone flux at 100 hPa from a wind field of the ERA-Interim and an ozone field of the MLS/TES data. The flux indicates increases in upward and downward ozone fluxes, respectively, in the tropics and the extratropics (Table 4.2). The change in the ozone fluxes in the simulations is weaker than the change estimated

from the ERA-Interim and the MLS/TES in all latitude bands.

Sudo and Takahashi [2001] reported that large-scale atmospheric circulation, convection, and water vapor are key factors contributing to change in tropical tropospheric ozone during El Niño. To elucidate the processes determining ENSO-related variation of ozone, we quantify the individual impacts of transport (i.e. atmospheric circulation and convection) and chemistry (i.e. water vapor) on ozone variation. We additionally conducted the sensitivity simulation fixed to average of chemical field (P and β) for 2004–2009 (MTT-fCHEM). The simulation presents that transport and chemistry have comparable impacts on the ozone variation in the tropics (Figures 4.12a, b). However, the impact of chemistry is dominant in the lower troposphere over the central and eastern Pacific. The variation attributable to chemistry is probably caused by variations in water vapor and lightning NO_x, although variations in temperature and cloud might affect it. Our simulation shows that the impact of chemistry is greater than the results of chapter 3 over the Indian Ocean and the western Pacific, reflecting enhanced production of lightning NO_x over Africa (Figure 4.13).

We also quantify the individual impacts of transport and chemical processes on the ozone variation. The MTT simulation accommodates year-to-year variation of both transport field (wind field) and chemical field (P and β of O_x), although the MTT-fCHEM simulation allows only the transport field to vary among years. The impact of transport is defined as a regression coefficient of ozone in the MTT-fCHEM simulation. We also define the impact of chemistry as a regression coefficient of ozone difference between the MTT and the MTT-fCHEM. The simulations present that transport and chemistry have comparable impacts on the ozone variation in the tropics (Figures 4.12a, b). However, the impact of chemistry is dominant in the lower troposphere over the central and eastern Pacific. Our simulations show that the impact of chemistry is greater than that shown in Sekiya and Sudo [2012] (Figure 6 of Sekiya and Sudo [2012]) over the Indian Ocean. This difference reflects an increase in the production rate of O_x over Africa in the FC simulation, in which a regression coefficient of lightning NO_x production with respect to Niño3.4 index is positive (7.3 kg N/m^2/s/K) over Africa (Figure 4.13).

In the subtropics over the eastern Pacific, transport and chemistry play significant roles in the most regions. Nevertheless the impacts of transport are dominant in the midlatitude lower stratosphere over the eastern Pacific (Figures 4.12c, d). The model also calculates separate tracers for O_3 produced in the stratosphere ($p > 100$ hPa) and the troposphere ($p < 100$ hPa). These indicate that ozone from the stratosphere and the troposphere respectively contributes to the ozone increase because of transport in the upper troposphere and lower stratosphere. In the lower troposphere, ozone from the troposphere dominates the ozone increase. These results also suggest that

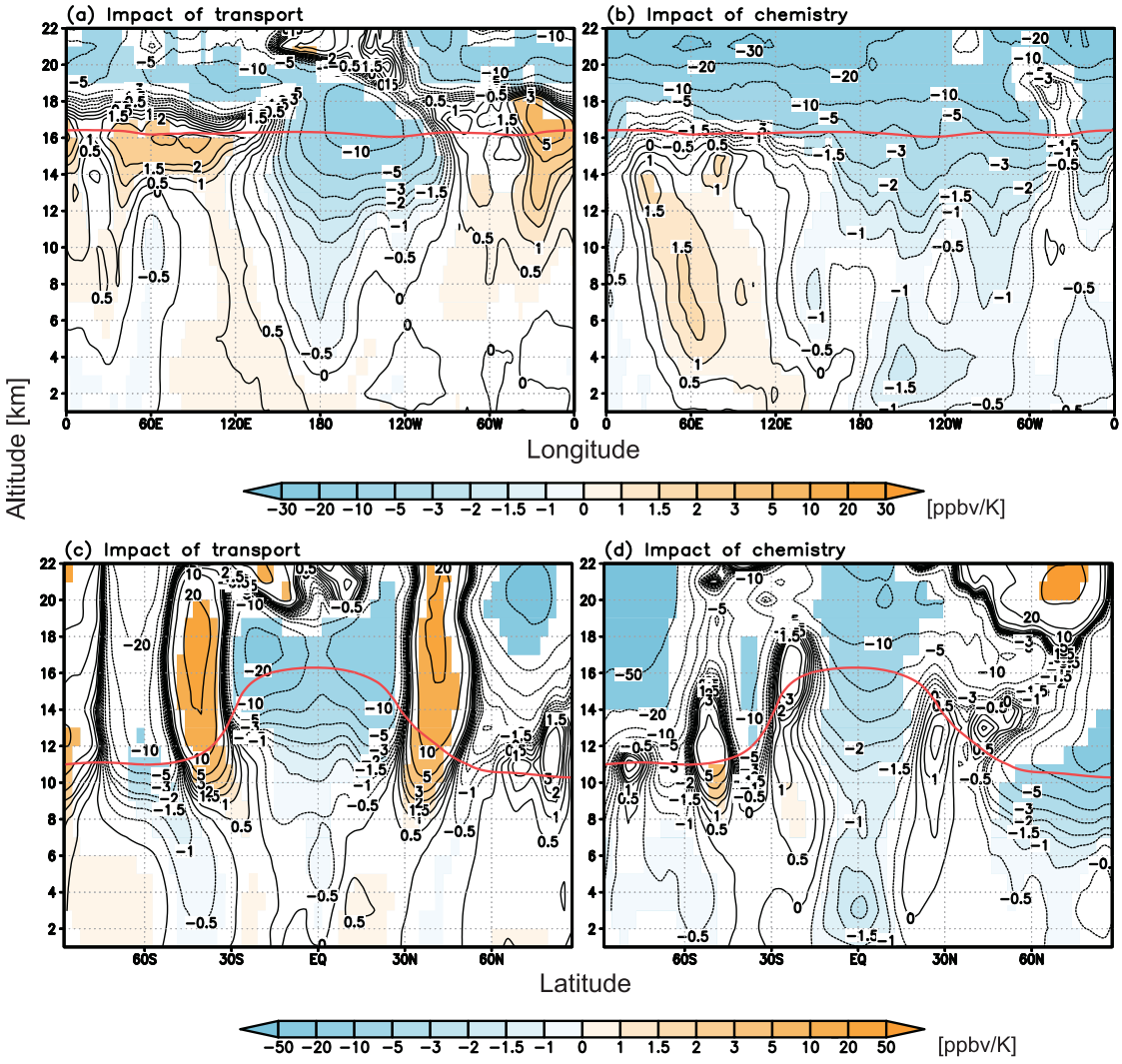

Figure 4.12. Impacts of (a, c) transport and (b, d) chemistry on the regression coefficients of ozone (ppbv/K) with respect to Niño3.4 index estimated from the MTT and the MTT-fCHEM during 2004–2009. The top and the bottom panels respectively show the average in the tropics (15°S–15°N) and the eastern Pacific (180°–230°E). The shaded regions show a significant ozone variation at a 95% confidence level. Red line is the tropopause height. The tropopause height in the left panel is calculated from the ERA-Interim.

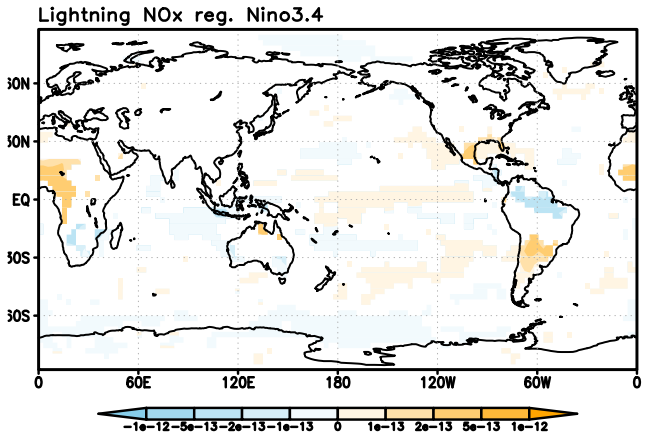

Figure 4.13. A regression coefficient of lightning NO_x production (kg/m^2/s/K) with respect to Nino3.4 index in by the FC simulation. Shaded regions show significant ozone variation at a 95% confidence level.

the ozone increase in the subtropics is caused not only by the intensified stratosphere–troposphere ozone exchange but also by the variation in tropospheric transport. For example, the export of Asian pollution to the Pacific is enhanced during El Niño, resulting from an intensification and a southward shift of the northern subtropical jet over the eastern Pacific [Koumoutsaris et al., 2008].

4.5 Change during the 1980s and 2000s

This study conducted global simulation of ozone concentrations for the 1980s. We evaluate the change in meteorology during the 1980s and 2000s, before evaluation of the ozone change. Figure 4.14a depicts a linear trend in annual and zonal means of temperature for 1979–2009 in the ERA-Interim reanalysis. The ERA-Interim shows negative trend of 0.2–0.6 K/decade between 18–30 km altitude in the tropics and the midlatitudes, and negative trend of up to 0.8 K/decade in the polar lower stratosphere (12–21 km altitude). The models simulate a negative trend of up to 0.8 K/decade in the stratosphere, although the location of the negative trend is replaced upward compared to that in the ERA-Interim (Figures 4.14b, c). The models do not reproduce the negative trend in the ERA-Interim in the polar lower stratosphere. In the troposphere, a positive trend of about 0.2 K/decade is found, although most of the observed trends are not significant at a 98% confidence level estimated by Student's t-test. A simulated positive trend of 0.2–0.4 K/decade is greater than that in the ERA-Interim. Figures 4.14b and c also present slight changes in residual circulation (arrows) in the models. Additionally, no crucial difference of the changes in meteorology is found in the MTT and the HTT.

Figure 4.15 shows a difference of total column ozone from the average for 1979–1982 in the

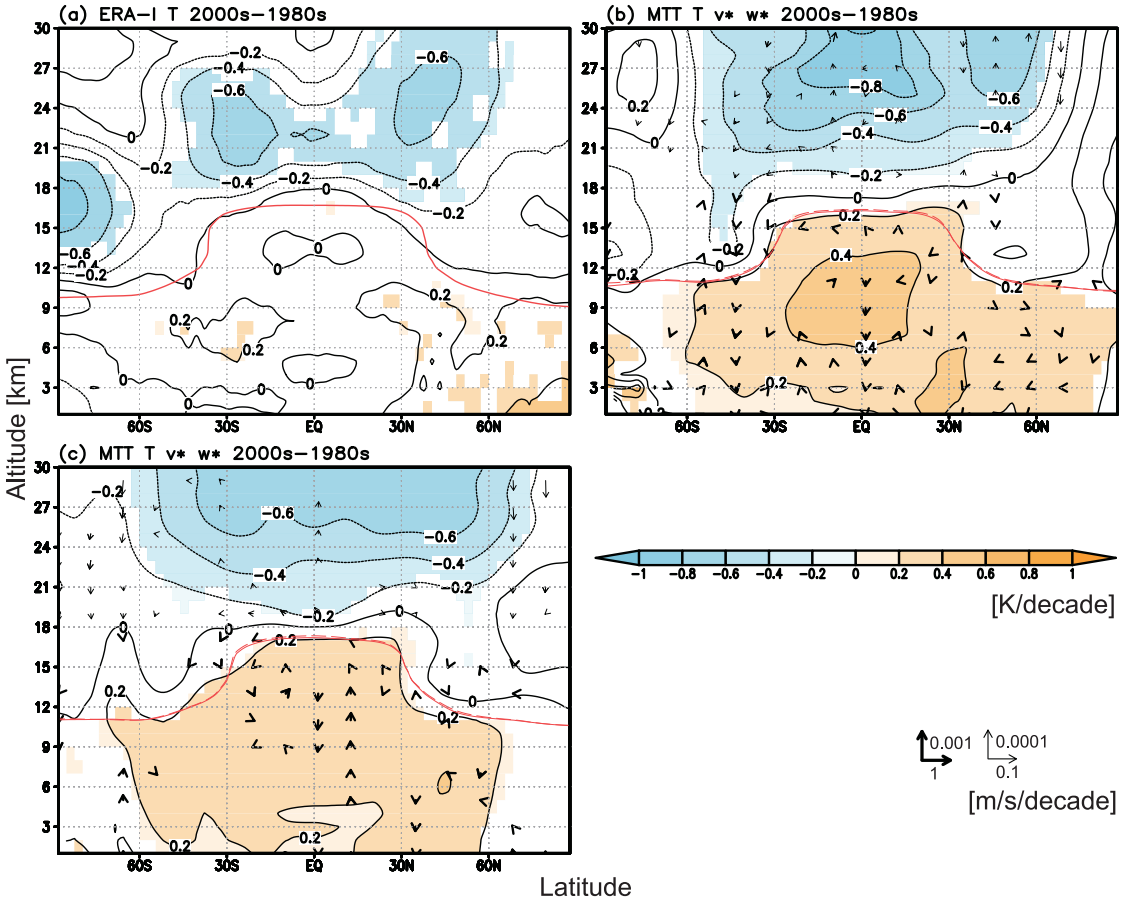

Figure 4.14. Zonal means of changes in temperature (K/decade) and residual circulation (m/s/decade) during the 1980s and 2000s. Shaded regions show significant temperature changes at a 98% confidence level. The arrow indicates wind field change at a 98% confidence level (only the simulations): (a) is the ERA-Interim; (b) is the MTT simulation; (c) is HTT. The vertical component of residual circulation is multiplied by 1000. The scale of thin arrow is 10 times larger than that of thick arrow. Solid red line is the tropopause height in the simulations for the 2000s, and dashed red line is the tropopause height in the simulations for the1980s.

MOD. The MOD shows a negative linear trend of the global and annual mean total column ozone ($-1.27\pm0.60\%$/decade) during 1979–2005. A range of the trend is a two-side 95% confidence interval. We calculated the linear trend excluding the data for 1992–1995, because the data is largely influenced by the Pinatubo eruption. Figure 4.15 also shows a difference of the global and annual mean of total column ozone in the MTT (red) and the HTT (blue) between the 1980s and 2000s. The simulated difference is $0.47\pm0.16\%$/decade in the MTT and $0.48\pm0.11\%$/decade in the HTT. A range of the simulated change is defined as a root-sum-square value of standard deviation for the simulations. We excluded the model data where the observation data is missing from the global and annual mean. The medium and high resolution simulations underestimate the observed negative trend. The difference between the observation and the simulation is comparable to the range. Figure 4.16 portrays the observed and the simulated changes in ozone during the 1980s and 2000s. The observed ozone change is a linear trend calculated from the data merging SAGE I+II instruments and ozonesonde for 1979–2005 in the same manner as the total column ozone. The maximum value of the observed negative trend (-230 ppbv/decade) is found in the lower stratosphere over the Antarctic. The simulations underestimate the observed negative trend in the lowermost stratosphere (about 10–24 km altitude). Particularly, the simulated trend shows an opposite sign to that in the observation in the northern extratropics. The deficit suggests that we need to improve the stratospheric chemistry scheme in our model. The simulations also calculated an increase in tropospheric ozone. The maximum of relative changes are located in the tropical upper troposphere and near the tropopause in the northern extratropics (6%/decade). In the middle troposphere of the northern midlatitudes, the simulations show an elevated ozone concentrations of 1.5–4%/decade. The changes fall within a range of the change derived from the long-term surface and ozonesonde observations [Oltmans et al., 2006; Parrish et al., 2012].

We also examine respective impacts of transport and chemical processes on the ozone change between the 1980s and 2000s to elucidate the processes controlling the ozone change. The MTT for the 1980s and the 2000s simulates ozone with the transport field (wind field) and the chemical field (P and β of O_x) for the corresponding period. The MTT-fCHEM simulates ozone with the transport field for the 1980s and the chemical field for the 2000s. We define the impact of transport as the difference between the MTT-fCHEM and the MTT for the 2000s, and define the impact of chemistry as the difference between the MTT for the 1980s and the MTT-fCHEM. Figures 4.17a and 4.17b show respectively impacts of transport and chemistry. Chemical process plays major roles in the ozone change in the stratosphere and troposphere. The ozone increase in the troposphere and decrease in the stratosphere can be attributable to emission increases of tropospheric ozone

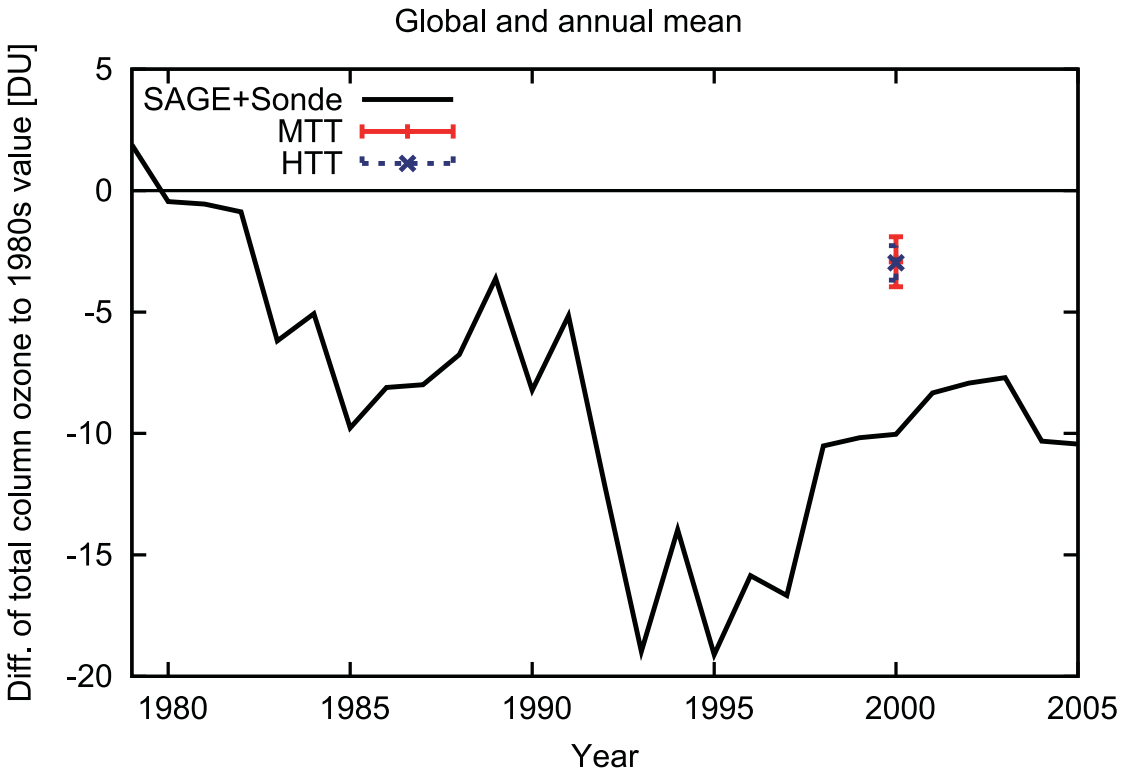

Figure 4.15. Timeseries of the difference of total column ozone (DU) from the average for 1979–1982 (black line). The differences of the simulated total column ozone between the 1980s and 2000s in the MTT (red plus) and the HTT (blue cross) are also shown. The error bar is a root-sum-square value of standard deviation for the simulations.

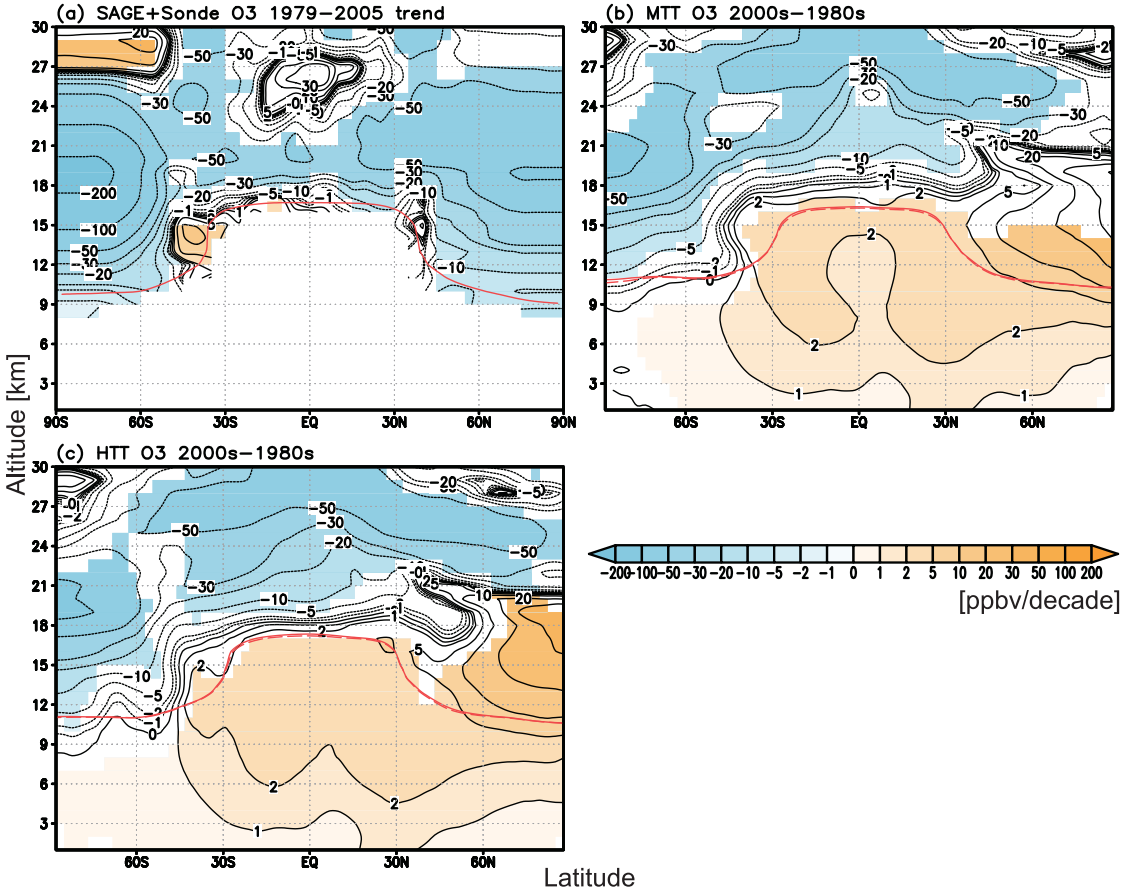

Figure 4.16. Zonal mean of changes in ozone (ppbv/decade) during the 1980s and 2000s. Shaded regions show significant ozone change at a 98% confidence level: (a) is the observation data obtained from the SAGE I and II satellite instruments and the ozonesonde in the polar region [Randel and Wu, 2007]; (b) is the MTT simulation; (c) is the HTT. (a) is a linear regression coefficient between 1979 and 2005, excluding the data for 1992–1995; (b) and (c) are differences between simulations for the 1980s and the 2000s. Solid red line is the tropopause height in the simulations for the 2000s, and dashed red line is the tropopause height in the simulations for the1980s.

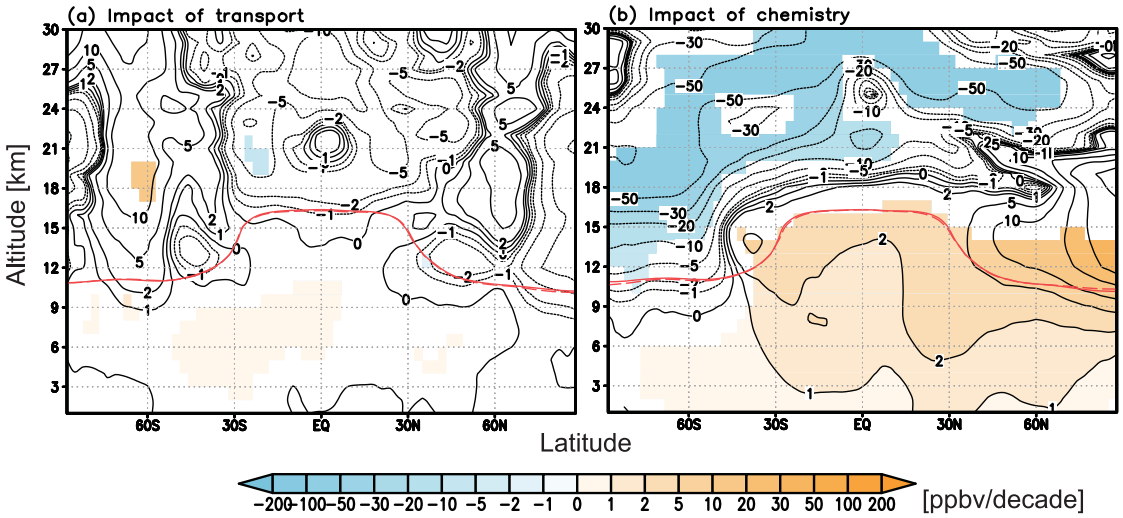

Figure 4.17. Impact of (a) transport and (b) chemistry on annual and zonal mean change in ozone (ppbv) during the 1980s and 2000s in MTT. Shaded regions show significant ozone change at a 98% confidence level. Solid red line is the tropopause height in the simulations for the 2000s, and dashed red line is the tropopause height in the simulations for the1980s.

precursors and ODSs. The changes in temperature and water vapor also influence chemical ozone production and loss. However, we do not isolate each effect. Transport process cause an increase in the global tropospheric ozone burden (0.30%/decade). The increase because of transport is supported largely by stratospheric-origin ozone (78%) rather than tropospheric-origin ozone.

4.6 Summary

This chapter evaluated the performance of our CCM focusing on (1) the ENSO-related ozone variation in the troposphere and lower stratosphere during 2004–2009 and (2) the change in stratospheric and tropospheric ozone during the 1980s and 2000s. Additionally, we conducted the simulations at two different horizontal resolutions (about 300 km and 120 km) to test the impact of horizontal resolution change on ozone through transport apart from chemistry. Our model captures general features of the observed ozone climatology, although the simulated ozone is high-biased in the lower stratosphere and low-biased in the troposphere. These biases in the simulation of two resolutions are similar.

This study evaluated the ENSO-related variation in tropospheric and lower stratospheric ozone in the simulations of medium and high resolutions forced by the observed SST variability. The medium and high resolution simulations show an increase in tropospheric ozone (1 ppbv/K) in the tropical western Pacific, and a decrease (2–20 ppbv/K) in the tropical eastern Pacific. The re-

sults generally agree with the variation observed by the MLS/TES instruments. In the midlatitude lower stratosphere over the eastern Pacific, ozone increases by 10 ppbv/K and by 50 ppbv/K are also found respectively in the medium and high resolution simulations. The simulated increase in the high resolution simulation agrees with the observed one better. In the other regions, no great difference exists between the two simulations. To investigate the processes determining the ENSO-related variation of ozone, we quantified the individual impacts of transport and chemistry using the sensitivity simulation fixed to the average chemical field for 2004–2009. The simulation shows that transport and chemistry play important roles in the ozone variation in the most regions. However, chemistry prevailingly affects the ozone decrease in the tropical lower troposphere over the eastern Pacific. Transport process dominates the ozone increases in the midlatitude lower stratosphere over the eastern Pacific. Transport of ozone of both stratospheric and tropospheric origin contributes to the upper tropospheric ozone increase, although the ozone increase results from ozone of tropospheric origin in the lower and middle troposphere.

This chapter also evaluated the change in stratospheric and tropospheric ozone during the 1980s and 2000s in the time-slice simulations. The simulated global and annual mean of total column ozone is decreased $0.47 \pm 0.16\%$/decade in the MTT and $0.48 \pm 0.11\%$/decade in the HTT during the 1980s and 2000s. The simulations underestimate the linear trend observed by TOMS/SBUV instruments ($-1.27 \pm 0.60\%$). The simulations also underestimate the observed negative trend in ozone (-230 ppbv/decade) in the lower stratosphere over the Antarctic. In the troposphere, the simulation shows an increase in global tropospheric ozone burden (3.6%/decade). The maximum of relative changes are located in the tropical upper troposphere and near the tropopause in the northern extratropics (6%/decade). The medium and high resolution simulations show similar changes in ozone during the period. Using the sensitivity simulation with the 1980s transport field and the 2000s chemical field, we examined the respective impacts of transport and chemical processes on the ozone change. The change is caused by chemical processes in the stratosphere. In the troposphere, chemical processes is more important than transport process. The change attributable to chemistry probably reflects the increased emissions of tropospheric ozone precursors and ODSs. The ozone increase because of transport is attributable to stratospheric-origin ozone.

Chapter 5

Long-term future change in global ozone

5.1 Introduction

Tropospheric ozone has increased from the pre-industrial to the present because of increased emissions of tropospheric ozone precursors (NO_x, CO, non-methane VOCs) and methane [Fusco and Logan, 2003; Lang et al., 2012; Stevenson et al., 2013]. Stratospheric ozone has been depleted over the past three decades, which is attributable to increased emissions of ozone-depleting substances (ODSs) [Gillett et al., 2011]. In the future, not only the reduced emissions but also climate change can influence change in stratospheric and tropospheric ozone [Brasseur et al., 2006; Zeng et al., 2008; Eyring et al., 2010b; Kawase et al., 2011]. The future change in stratospheric ozone is influenced by a decrease in temperature and by a strengthening of Brewer–Dobson circulation associated with climate change [Li et al., 2009]. In the troposphere, the strengthening also causes an increase in tropospheric ozone through stratosphere–troposphere exchange (STE) of ozone [e.g. Collins et al., 2003; Sudo et al., 2003; Zeng and Pyle, 2003]. In the lower troposphere, higher water vapor facilitates the chemical destruction of tropospheric ozone [Johnson et al., 2001]. Moreover, higher temperatures decompose PAN into NO_x more efficiently [e.g. Doherty et al., 2013]. Recent studies also investigate the future change under the framework of multi-model inter-comparison projects [Stevenson et al., 2006; Eyring et al., 2010a; 2013; Young et al., 2013].

As described above, the previous studies investigated a response of ozone to an individual external forcing (e.g. tropospheric ozone precursors, ODSs, and GHGs). We also need to investigate a role of an individual process quantitatively. This chapter quantifies the individual impacts of transport and chemical processes on the future ozone change during the 2000s and 2100s. Additionally, we test sensitivities of the future change in ozone to horizontal resolution through ozone transport (i.e. an impact of horizontal resolution on wind field and advection calculation) apart

Table 5.1. Summary of experiment performed in this study.

Full-chemistry simulation (FC)

Period	SST/SIC	GHGs/ODSs/Emissions
2100s (5yr)	HadISST[1] + MIROC[2]	RCP6 (2100)

O_3-tracer-transport simulation

Experiment	H. resolution	Period	SST/SIC	P, β
MTT	T42	2100s (7yr)	HadISST[1] + MIROC[2]	2100s
HTT	T106	2100s (7yr)	HadISST[1] + MIROC[2]	2100s
MTT-fCHEM	T42	2100s (7yr)	HadISST[1] + MIROC[2]	2000s

[1)] Average for 1995–2004

[2)] Difference between the 2000s and 2100s simulated by MIROC-ESM-CHEM

from chemistry using the model with two horizontal resolutions (about 300 km and 120 km) in the same manner as chapter 4.

This chapter is organized as follows. Section 5.2 provides the experimental settings. Section 5.3 presents future change in ozone between the 2000s and 2100s. Individual impacts of transport and chemical processes on the future change are examined in section 5.4. Finally, in section 5.5, we summarize the results in this chapter.

5.2 Experimental settings

We conducted the time-slice FC simulation for the 2100s. Their lengths are five years in the each period following Zeng et al. [2008]. We specified the concentrations of GHGs and ODSs, and the emissions of tropospheric ozone precursors in 2100 according to the RCP 6 scenario [Masui et al., 2011] as the boundary conditions for the 2100s (Table 5.1). In the scenario, the concentration of ODSs and the emissions of tropospheric ozone precursors are reduced during 2000 and 2100 (Table 5.2). The concentrations of CO_2 and N_2O are elevated during 2000 and 2100 in the RCP6, although that of CH_4 is slightly decreased. The FC simulation simulate the enhanced lightning NO_x production ($+23\%$). The monthly mean anomalies of SST between the 2000s and 2100s simulated by the original version of MIROC-ESM-CHEM [Watanabe et al., 2011a] added to the SST for the 2000s were used as the SST for the 2100s. The other settings are same as the FC simulation for the 2000s. The SIC for the 2100s was prescribed in the same manner. The initial conditions were taken from the result of ACCMIP experiment for the corresponding period using MIROC-ESM-CHEM [e.g. Lamarque et al., 2013].

We conducted the time-slice MTT simulations for the 2100s. The simulations ran for seven

Table 5.2. Change in the concentrations of CO_2, CH_4, and N_2O (ppm), the anthropogenic and biomass burning emissions of NO_x (Tg N/yr), CO (Tg/yr), and NMVOCs (Tg C/yr), and the production of lightning NO_x (Tg N/yr) during the 2000s and 2100s. The change in the concentrations and the emissions is taken from the RCP6 scenario. The lightning NO_x production is the simulated change during the 2000s and 2100s in the FC simulation. In the parenthesis, the relative change to the value in 2000 is also shown.

Concentration		
CO_2	300.8 ppm	(81.5 %)
CH_4	−101.6 ppm	(−5.8%)
N_2O	90.4 ppm	(28.6%)
Total chlorine	−2324.5 ppt	(−69.3%)
Total bromine	−8.9 ppt	(−42.1%)
Emission		
NO_x	−22.1 Tg N/yr	(−57.7%)
CO	−277.8 Tg/yr	(−25.8%)
NMVOCs	−21.4 Tg C/yr	(−15.2%)
Lightning		
NO_x	1.2 Tg N/yr	(23.2%)

years in the each period. The P, β, and GHGs (N_2O, CH_4, and CFCs) were prescribed by the output obtained from the time-slice FC simulations (the top three rows in Table 5.1). The other settings are same as the time-slice FC simulations. Additionally, we performed the simulation which calculates the ozone tendency attributable to transport and dry deposition in the 2100s with the P and β in the 2000s (hereinafter MTT-fCHEM). To assess a sensitivity of the future change in ozone to the change in horizontal resolution, we performed the time-slice HTT simulations for the 2100s. Their lengths are seven years in the each period. The boundary and initial conditions for HTT simulations were linearly interpolated from those for the MTT simulations.

5.3 Future changes

We performed future projections of climate and ozone, and investigated the future changes. The sensitivity of the change to the horizontal resolution is also assessed by comparing the projection with two horizontal resolutions (about 300 km and 120 km). We used the results in the last five years for each period. Figure 5.1 portrays the change in annual and zonal mean temperatures between the 2000s and 2100s. The MTT simulation shows a warming of 4 K in the troposphere and a cooling of 4 K in the stratosphere (Figure 5.1a). The HTT simulates a warming similar to that in the MTT in the troposphere. Moreover, the HTT simulates a slightly stronger cooling in the tropical lower stratosphere, a weaker cooling in the high latitudes lower stratosphere, and a stronger warming in

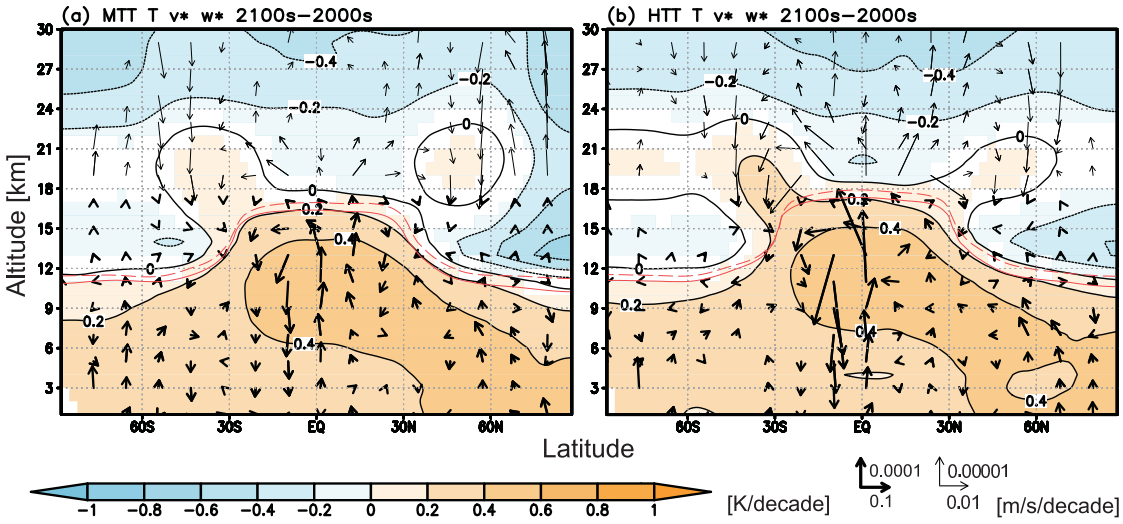

Figure 5.1. Zonal mean of changes in temperature (K/decade) and residual circulation (m/s/decade) during the 2000s and 2100s. The shaded regions show a significant temperature changes at a 98% confidence level. Arrows indicate a wind field change at a 98% confidence level: (a) is the MTT simulation; (b) is the HTT. The vertical component of residual circulation is multiplied by 1000. The scale of thin arrow is 10 times larger than that of thick arrow. Solid red line is the tropopause height in the simulations for the 2000s, and dashed red line is the tropopause height in the simulations for the 2100s.

the subtropical lower stratosphere (Figure 5.1b).

The model predicts an increase in global stratospheric ozone burden by $0.24 \pm 0.01\%$/decade in the MTT and by $0.29 \pm 0.01\%$/decade in the HTT. We regard the range of change as a root-sum-square value of the standard deviation in the simulations for the 2000s and the 2100s. The predicted changes in annual and zonal mean ozone during the 2000s and 2100s show a decrease by 20 ppbv/decade in the tropical lower stratosphere, and an increase by 20 ppbv/decade in the extratropical lower stratosphere (Figure 5.2). In the most region at a 98% confidence level estimated by Student's t-test (shaded region), a range of the change is within 30% of the change. The change in stratospheric ozone in the two resolution simulations is within the range of change, except in the lower stratosphere over the northern high latitudes where the difference reaches to 18 ppbv/decade (about two-times-larger increase) at 23 km altitude. The global annual mean ozone change at 50 hPa is -0.0028 ppmv/decade in the MTT and -0.0014 ppmv/decade in the HTT, which are smaller and opposite changes compared to the multi-model mean of CMIP5 and CCMVal-2 models [Eyring et al., 2013]. In particular, we must interpret the change in the lower stratosphere over the northern mid to high latitudes with some caution, because our model simulates a decrease in ozone at 50 hPa over there in contradiction to the result of CMIP5 models.

The global tropospheric ozone burden is reduced between the 2000s and 2100s by $0.82 \pm$

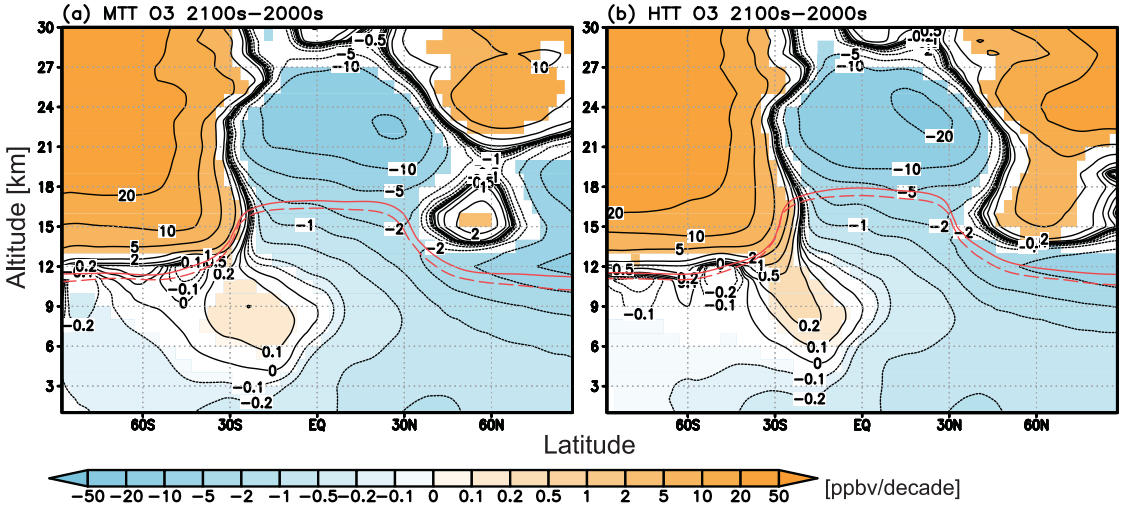

Figure 5.2. Zonal mean of change in ozone (ppbv/decade) during the 2000s and 2100s. The shaded regions show a significant ozone change at a 98% confidence level: (a) is the MTT simulation; (b) is the HTT. Solid red line is the tropopause height in the simulations for the 2000s, and dashed red line is the tropopause height in the simulations for the 2100s.

0.04%/decade in the MTT and by 0.76 ± 0.04 %/decade in the HTT. A reduction of tropospheric ozone concentration is typically 0.8 ppbv/decade in the free troposphere over the northern midlatitudes (Figure 5.2). The simulated tropospheric ozone is slightly increased in the upper troposphere over the southern subtropics (typically ≤ 0.2 ppbv/decade). In the most region at a 98% confidence level (shaded region), a range of the change in tropospheric ozone is within 30% of the change. The difference of tropospheric ozone change between the MTT and the HTT is smaller than 0.1 ppbv/decade in the middle and lower troposphere, and is comparable to the range of change in tropospheric ozone. In comparison with the time-slice simulations for the 2000s and the 2100s along with RCP6 scenario in Young et al. [2013], the reduction of global tropospheric ozone burden in this study is similar to that simulated by the ACCMIP models (0.9%/decade). The change in tropospheric ozone in this study also shows a similar value to that in the ACCMIP models (0.5–1 ppbv/decade) in the free troposphere over the northern midlatitudes. In the southern hemisphere, our simulations do not show an increase in tropospheric ozone as shown in the mean of the ACCMIP models. However, our model predicts the reduction of global tropospheric ozone burden larger than that (-0.15%/decade) in Kawase et al. [2011].

The differences of temperature and ozone between MTT and HTT are at least partially attributable to differences in the strengthening of Brewer–Dobson circulation (BDC). HTT simulates acceleration of BDC stronger than MTT (arrows in Figure 5.1). At 100 hPa, vertical mass flux are strengthened by 20% in MTT and by 25% in HTT (Table 5.3). The acceleration of BDC results in an increase of ozone influx from the stratosphere to the troposphere. We also examine vertical

Table 5.3. Future change in vertical mass and ozone (in parentheses) flux at 100 hPa during the 2000s and 2100s. The positive sigh is upward flux. Unit of the mass flux is 10^6 Tg/yr/decade. Unit of the ozone flux is Tg/yr/decade. The range is defined as a root-sum-square value of the standard deviation in the simulations.

	90°S–20°S	20°S–25°N	25°N–90°N
Change during the 2000s and 2100s			
MTT	-2.98 ± 0.76	6.24 ± 0.92	-3.30 ± 0.75
	(-5.19 ± 1.50)	(-0.21 ± 0.36)	(-1.93 ± 1.99)
HTT	-5.19 ± 0.59	10.33 ± 0.96	-5.14 ± 0.63
	(-9.11 ± 1.34)	(0.07 ± 0.43)	(-5.22 ± 2.00)

ozone flux at 100 hPa instead of STE ozone flux (Figure 5.3). The upward ozone flux is not altered significantly in the tropics because the ozone decrease and enhanced upwelling cancel each other out in the lower stratosphere. The downward ozone flux in the extratropics of northern and southern hemisphere is increased in MTT (19.3 and 51.9 Tg/yr, respectively). HTT predicts that downward fluxes in the northern and southern extratropics are, respectively, 52.2 and 91.1 Tg/yr, which are about two times larger than those in MTT.

The differences of temperature and ozone between the MTT and the HTT are at least partially attributable to a difference in the strengthening of Brewer–Dobson circulation (BDC). The HTT simulates an acceleration of BDC stronger than that in the MTT (arrows in Figure 5.1). At 100 hPa, the vertical mass flux is strengthened by 20% in the MTT and by 25% in the HTT during the 2000s and 2100s (Table 5.3). The acceleration of BDC results in an increase of ozone influx from the stratosphere to the troposphere. We also examine the vertical ozone flux at 100 hPa instead of STE ozone flux (Table 5.3). The upward ozone flux is not altered significantly in the tropics, because the ozone decrease and the enhanced upwelling cancel each other out at 100 hPa. The downward ozone flux in the extratropics of northern and southern hemispheres is increased in the MTT (1.93 and 5.19 Tg/yr/decade, respectively). The HTT predicts that the downward fluxes in the northern and southern extratropics are, respectively, 5.22 and 9.11 Tg/yr/decade, which are about two times larger than those in the MTT.

5.4 Impacts of transport and chemical processes

The future ozone changes are caused by transport (i.e. atmospheric circulation, convection, and vertical diffusion) and chemistry (i.e. temperature, water vapor, and emissions of ozone precursors and ODSs) processes in a similar fashion to the ENSO-related variation of ozone. To understand the processes determining future changes in ozone, we investigate the individual impacts of transport and chemistry on the ozone change. Therefore, we performed a sensitivity simulation with climate

(SST/SIC and GHGs) in the 2100s and chemical field (P and β of O_x) in the 2000s using a medium resolution model (MTT-fCHEM). Figures 5.3a and 5.3b respectively depict ozone changes between the 2000s and 2100s attributable to transport and chemistry. The change in ozone is mainly driven by chemistry in the stratosphere. Decrease in ODSs dominates the ozone increase attributable to chemistry in the southern extratropics. In the tropics and the northern extratropics, ozone decreases because of chemistry might be related to a decrease in actinic flux through an overhead ozone increase.

The future ozone change is caused by transport (i.e. atmospheric circulation, convection, and vertical diffusion) and chemical (i.e. temperature, water vapor, emissions of ozone precursors and ODSs, etc.) processes. To understand the processes determining the future change in ozone, we investigate individual the impacts of transport and chemistry on the future ozone change. The MTT for the 2000s and the 2100s simulates ozone with the transport field (wind field) and the chemical field (P and β of O_x) for the corresponding period. The MTT-fCHEM simulates ozone with the transport field for the 2100s and the chemical field for the 2000s. We define the impact of transport as the difference between the MTT-fCHEM and the MTT for the 2000s, and define the impact of chemistry as the difference between the MTT for the 2100s and the MTT-fCHEM. Figures 5.3a and 5.3b respectively depict the ozone change between the 2000s and 2100s attributable to transport and chemistry. The change in ozone is mainly driven by chemistry in the stratosphere. The decrease in ODSs dominates the ozone increase attributable to chemistry in the extratropical lower stratosphere of the southern hemisphere. In the tropical lower stratosphere and the extratropical lower stratosphere of the northern hemisphere, the decrease in ozone because of chemistry is caused by a decrease in the production of ozone, which exceeds a decrease in the loss of ozone. The decrease in production is related to a decrease in the actinic flux through an overhead ozone increase.

In the troposphere, chemistry process causes the reduction of global tropospheric ozone burden by 1.07%/decade (Figure 5.3b), reflecting the emission reductions of tropospheric ozone precursors and climate change. Transport process increases the global burden of tropospheric ozone by 0.25%/decade, corresponding to 23% of the decrease in global tropospheric ozone burden attributable to chemistry (Figure 5.3a). The model also calculates separate tracers for O_3 produced in the stratosphere ($p > 100$ hPa) and the troposphere ($p < 100$ hPa). Figures 5.3c and 5.3d suggest that the increase in global tropospheric ozone burden because of transport is supported by ozone of both the tropospheric-origin (57%) and the stratospheric-origin (43%).

We examine zonal mean of mass stream function for the 2000s and its change during the 2000s and 2100s to interpret the change in tropospheric ozone because of transport process. Figure 5.4

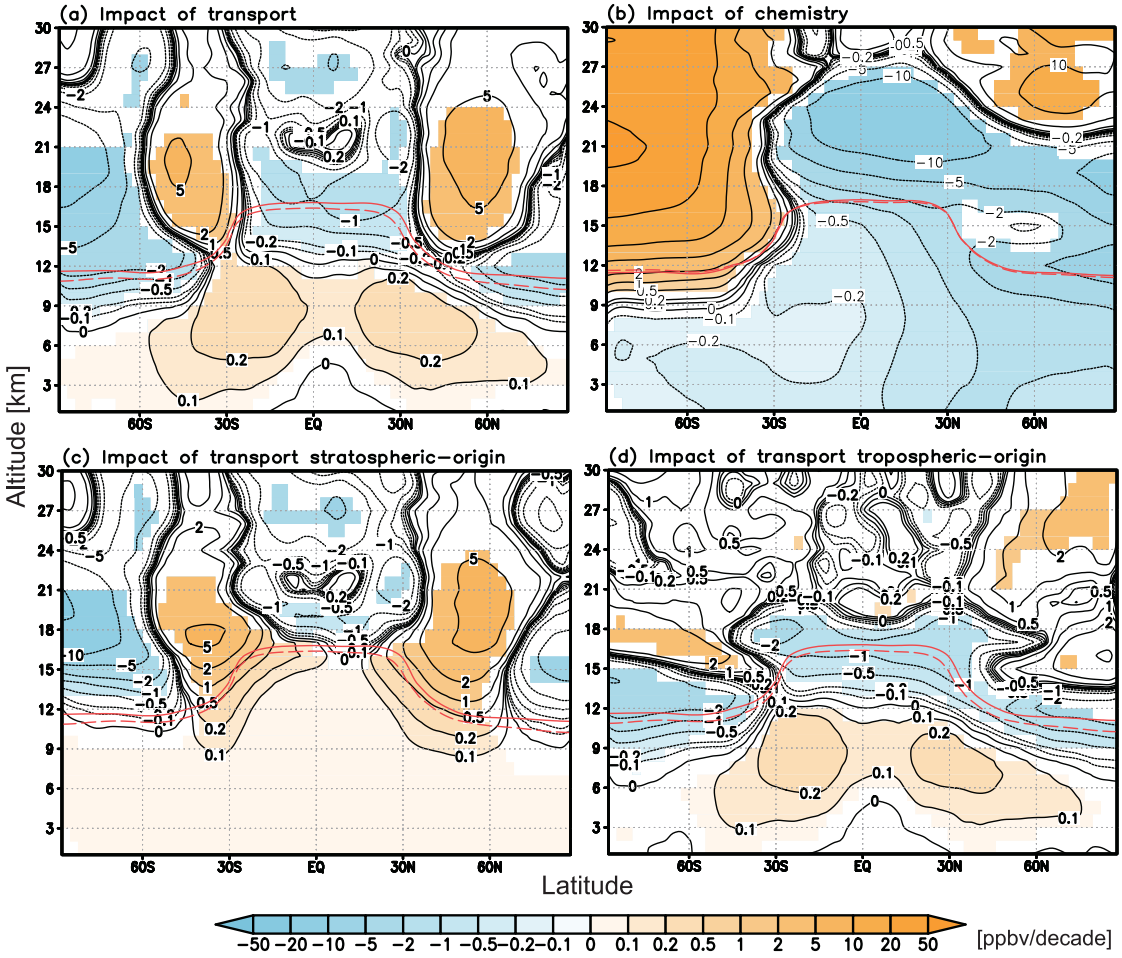

Figure 5.3. Impacts of (a) transport and (b) chemistry on annual and zonal mean change in ozone (ppbv/decade) during the 2000s and 2100s estimated from the MTT and the MTT-fCHEM, and impact of transport on future change in separate O_3 tracers produced in (c) the stratosphere and (d) the troposphere (ppbv/decade). The shaded regions show a significant ozone change at a 98% confidence level. Solid red line is the tropopause height in the simulations for the 2000s, and dashed red line is the tropopause height in the simulations for the 2100s.

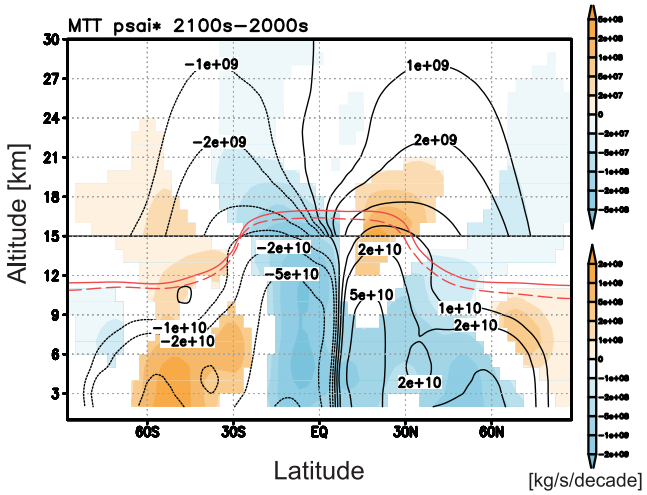

Figure 5.4. Zonal mean of residual mass stream function (kg/s) for the 2000s in the MTT (contour) and its change (kg/s/decade) during the 2000s and 2100s (shade). The shaded regions show a significant change at a 98% confidence level. Solid red line is the tropopause height in the simulations for the 2000s, and dashed red line is the tropopause height in the simulations for the 2100s. Different scales are used above and below 15 km altitude (horizontal line).

shows a positive (negative) change in the northern (southern) tropical stratosphere and a negative (positive) change in the high northern (southern) latitudes. These changes reflects an acceleration of BDC over the tropics and the midlatitudes and a deceleration over the high latitudes. The acceleration causes a decrease in ozone in the tropical lower stratosphere and an increase in the midlatitude lower stratosphere (Figure 5.3a). The deceleration leads to a decrease in ozone in the high latitude lower stratosphere. In the troposphere, the mass stream function shows a positive change over 60°N–90°N, a negative change over 20°S–60°N, and a positive change over 60°S–20°S (Figure 5.4). These changes indicate the enhanced southern branch of Hadley cell and the weakened meridional circulations elsewhere. However, we do not find clear relationship between the change in meridional circulation and the change in tropospheric ozone.

To interpret the impact of chemical process, we investigate change in production (P) and loss rate (β) of O_y family, which is defined as the sum of O_3, O, O(^{1}D), NO_2, 2×NO_3, 3×N_2O_5, PANs, HNO_3, and other nitrates. We use O_y family to exclude an effect of the following null cycle involving NO_x on P and β,

$$NO + O_3 \rightarrow NO_2 + O_2 \tag{5.1}$$

$$NO_2 + h\nu \rightarrow NO + O \tag{5.2}$$

$$O + O_2 + M \rightarrow O_3 + M. \tag{5.3}$$

Table 5.4. Reactions included for the calculation of the loss rate involving O_x, HO_x, NO_x, and halogen radicals (ClO_x and BrO_x).

β	Reaction
β_{O_x}	$O_3 + O \rightarrow 2O_2$
β_{HO_x}	$OH + O \rightarrow H + O_2$
	$OH + O_3 \rightarrow HO_2 + O_2$
	$HO_2 + O \rightarrow OH + O_2$
	$HO_2 + O_3 \rightarrow OH + 2O_2$
β_{NO_x}	$NO_2 + O \rightarrow NO + O_2$
β_{Cl+Br}	$ClO + O \rightarrow Cl + O_2$
	$Cl + O_3 \rightarrow ClO + O_2$
	$BrO + O \rightarrow Br + O_2$
	$Br + O_3 \rightarrow BrO + O_2$
β_{H_2O}	$O(^1D) + H_2O \rightarrow 2OH$

Figure 5.5a shows $\Delta P - \Delta\beta[O_3]_{2000s}$ in the FC simulation. Δ means the change during the 2000s and 2100s. We fix O_3 concentration to the 2000s value ($[O_3]_{2000s}$) to isolate the impact of the change in P and β. In the stratosphere, a global burden of $\Delta P - \Delta\beta[O_3]_{2000s}$ is positive (339 ± 382 Tg/yr). A decrease of $\Delta\beta[O_3]_{2000s}$ (-11168 ± 1164 Tg/yr) exceeds a decrease of ΔP (-10828 ± 1262 Tg/yr). Zonal mean distribution of $\Delta P - \Delta\beta[O_3]_{2000s}$ is positive (0.1–1 ppbv/day/decade) above 12 km altitude over the high southern latitudes and above 18 km altitude over the high northern latitudes. In the tropical lower stratosphere, it is negative (0.1 ppbv/day/decade). The distribution corresponds to the impact of chemical process on the future change in stratospheric ozone (Figure 5.3b). The effect of the negative $\Delta P - \Delta\beta[O_3]_{2000s}$ in the tropics propagates to the lowermost stratosphere over the high northern latitudes, because $\Delta P - \Delta\beta[O_3]_{2000s}$ is almost zero there. Figures 5.5b and c respectively illustrate ΔP and $\Delta\beta[O_3]_{2000s}$. $\Delta\beta[O_3]_{2000s}$ exceeds ΔP above 12 km altitude over the high southern latitudes and above 18 km altitude over the high northern latitudes, and vice versa in the tropical lower stratosphere.

We further investigate the respective contributions of O_y loss reactions involving O_x, HO_x, NO_x, and halogen radicals (ClO_x and BrO_x) to the change in β. Figures 5.6a–d respectively portray $\Delta\beta_{O_x}[O_3]_{2000s}$, $\Delta\beta_{HO_x}[O_3]_{2000s}$, $\Delta\beta_{NO_x}[O_3]_{2000s}$, and $\Delta\beta_{Cl+Br}[O_3]_{2000s}$. The subscript stands for chemical loss reactions, which is included for the calculation of the loss rate (Table 5.4). This suggests that the loss reactions involving the halogen radicals dominate the change in β during the 2000s and 2100s (98% in the global mean). Regarding the production of O_y, the reaction of ClO + NO $\rightarrow$ Cl + NO_2 (50% in the global mean) contributes to the change in P larger than the O_2 photolysis (12% in the global mean) in the stratosphere. These suggest that the reduction of ODSs strongly influences the change in P and β.

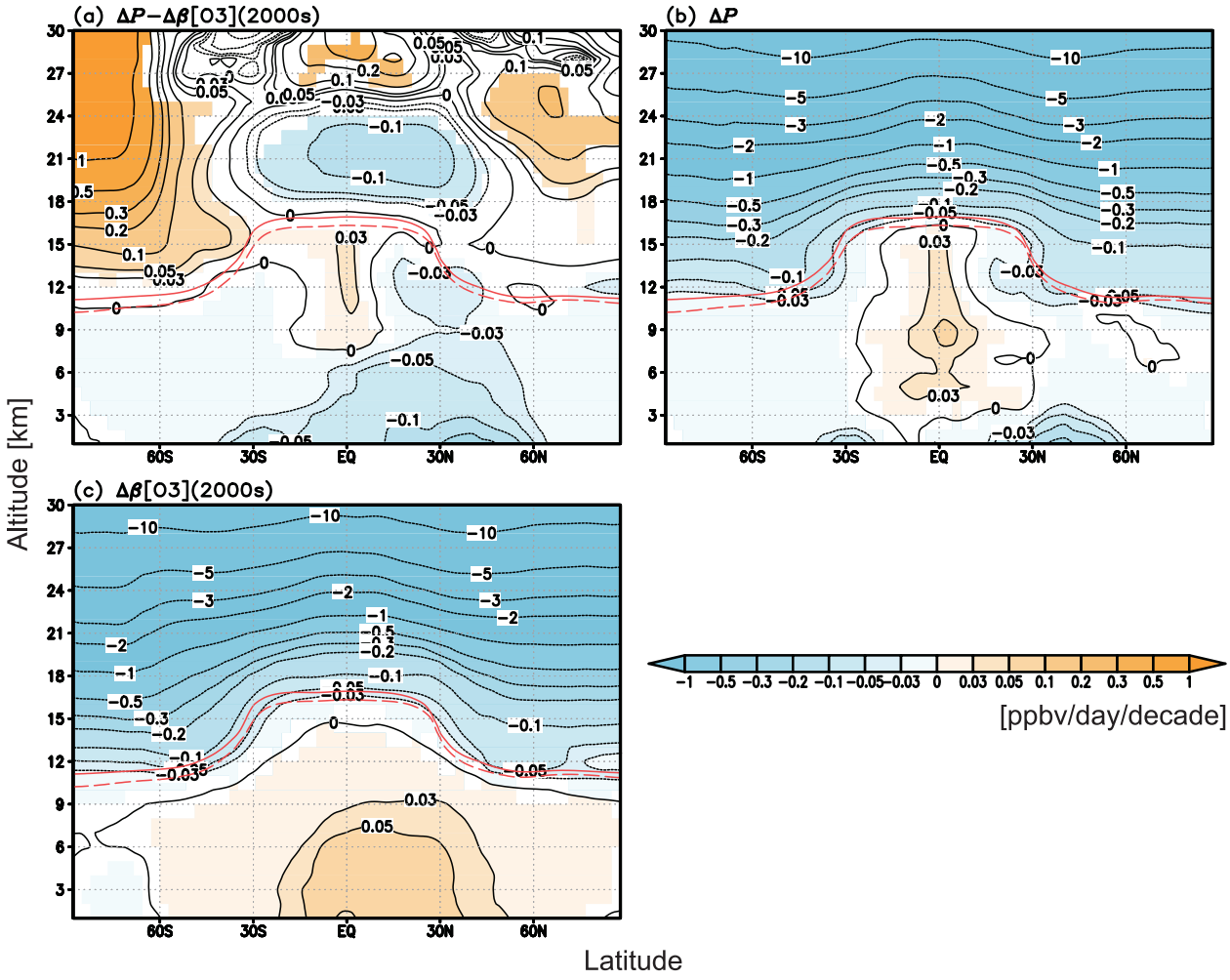

Figure 5.5. Zonal mean of (a) $\Delta P - \Delta\beta[\mathrm{O_3}]_{2000s}$, (b) ΔP, and (c) $\Delta\beta[\mathrm{O_3}]_{2000s}$ in the FC (ppbv/day/decade). Δ means the change during the 2000s and 2100s. P and β are respectively the production (ppbv/day) and the loss rate (1/day) of $\mathrm{O_y}$ ($= \mathrm{O_3} + \mathrm{O} + \mathrm{O(^1D)} + \mathrm{NO_2} + 2\mathrm{NO_3} + 3\mathrm{N_2O_5} + \mathrm{PANs} + \mathrm{HNO_3} +$ other nitrates). The shaded regions show a significant change at a 98% confidence level. Solid red line is the tropopause height in the simulations for the 2000s, and dashed red line is the tropopause height in the simulations for the 2100s.

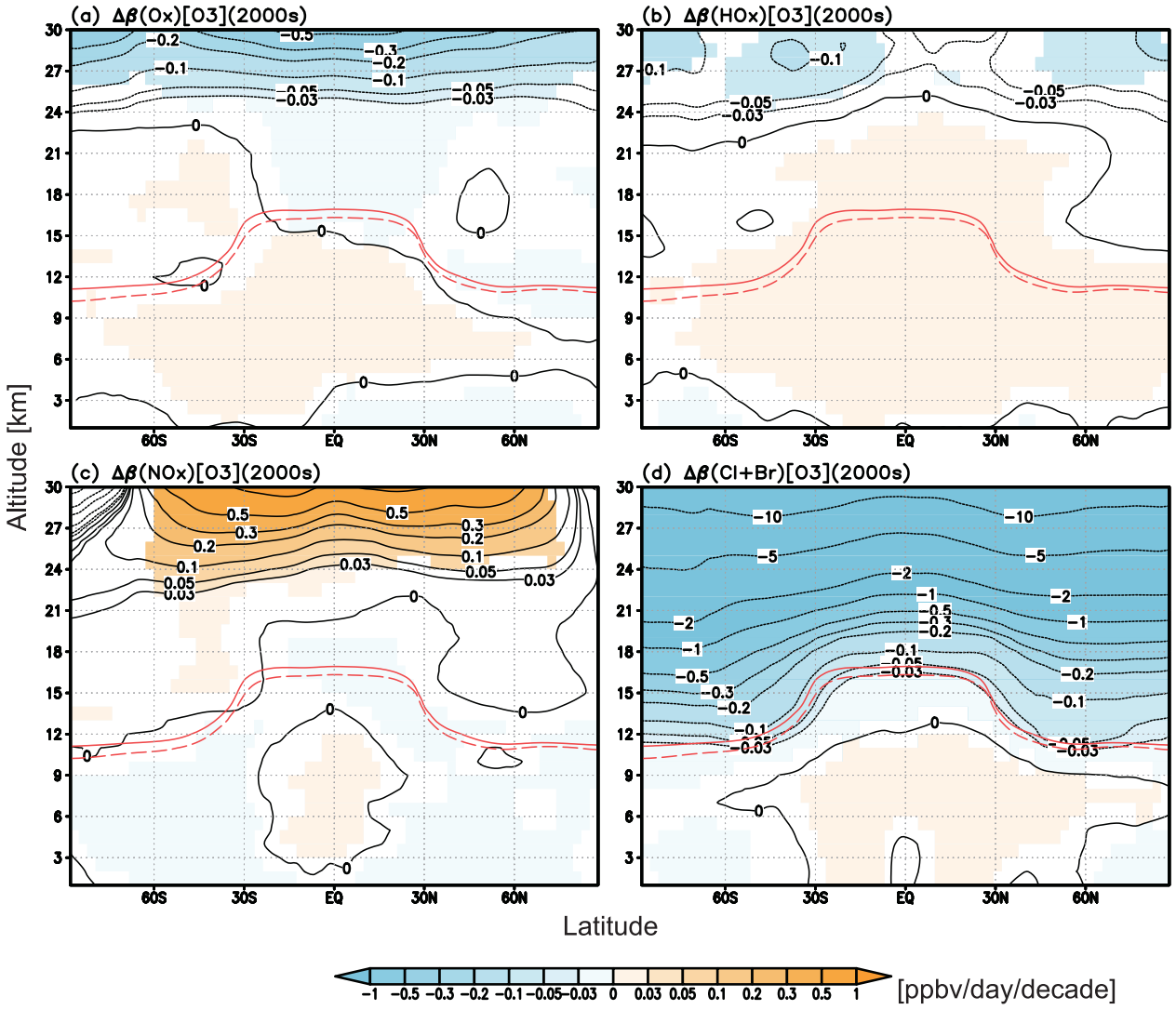

Figure 5.6. Zonal mean of (a) $\Delta\beta_{\mathrm{O_x}}[\mathrm{O_3}]_{2000s}$, (b) $\Delta\beta_{\mathrm{HO_x}}[\mathrm{O_3}]_{2000s}$, (c) $\Delta\beta_{\mathrm{NO_x}}[\mathrm{O_3}]_{2000s}$, and (d) $\Delta\beta_{\mathrm{Cl+Br}}[\mathrm{O_3}]_{2000s}$ in the FC (ppbv/day/decade). Subscript stands for chemical loss reactions included in the loss rate (summarized in Table 5.4). The shaded regions show a significant change at a 98% confidence level. Solid red line is the tropopause height in the simulations for the 2000s, and dashed red line is the tropopause height in the simulations for the 2100s.

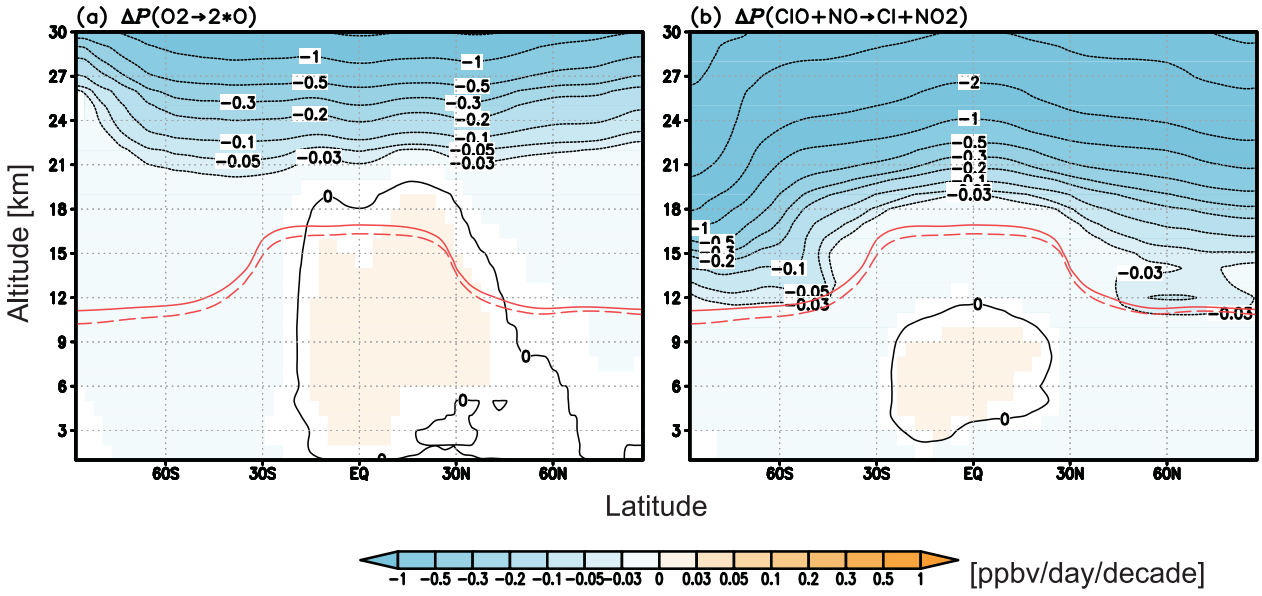

Figure 5.7. Zonal mean of (a) ΔP due to the reaction of $O_2 + h\nu \rightarrow 2O$, (b) ΔP due to the reaction of ClO + NO $\rightarrow$ Cl + NO_2 in the FC (ppbv/day/decade). The shaded regions show a significant change at a 98% confidence level. Solid red line is the tropopause height in the simulations for the 2000s, and dashed red line is the tropopause height in the simulations for the 2100s.

In the troposphere, a global burden of $\Delta P - \Delta\beta[O_3]_{2000s}$ is reduced by 1214 $\pm$ 233 Tg/yr. Zonal mean distribution of $\Delta P - \Delta\beta[O_3]_{2000s}$ is negative (up to 0.2 ppbv/day/decade in the lower troposphere) in the most regions and is positive (0.03 ppbv/day/decade) in the upper troposphere near the equator (Figure 5.5a). The negative $\Delta P - \Delta\beta[O_3]_{2000s}$ leads to the decrease in tropospheric ozone because of chemistry. Both the negative ΔP and the positive $\Delta\beta[O_3]_{2000s}$ contribute to the $\Delta P - \Delta\beta[O_3]_{2000s}$ in the lower and middle troposphere (Figures 5.5b and c). ΔP can be attributable to the decreased oxidation of hydrocarbon and the decelerated cycle involving NO_x. For instance, the reaction of HO_2 + NO $\rightarrow$ OH + NO_2 explains 54% of the total ΔP in the global mean. The $\Delta\beta_{H_2O}[O_3]_{2000s}$ is responsible for the total $\Delta\beta[O_3]_{2000s}$ (90% in the global mean). The enhanced β_{H_2O} reflects the higher concentration of water vapor associated with climate change. These indicate that the future change in tropospheric ozone is influenced not only by the reduced emission of tropospheric ozone precursors but also by climate change through chemical process.

5.5 Summary

In this chapter, we examined the respective impacts of transport and chemical processes on the future change in tropospheric and stratospheric ozone during the 2000s and 2100s. Additionally, we conducted the simulations at medium and high horizontal resolutions (about 300 km and 120

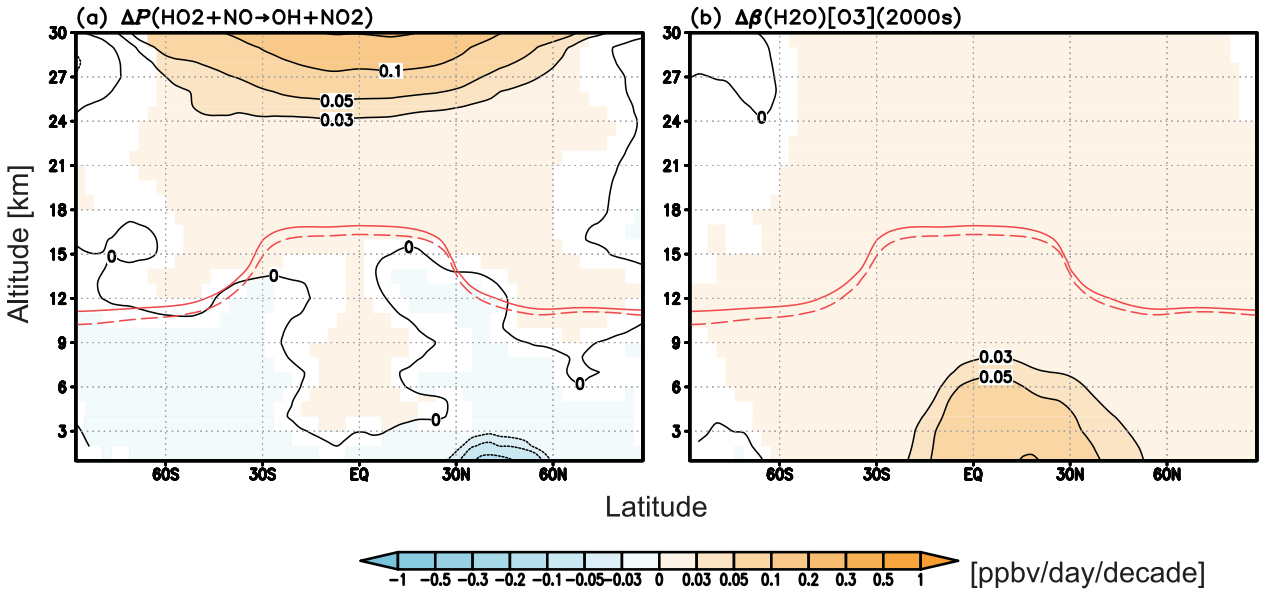

Figure 5.8. Zonal mean of (a) ΔP due to the reaction of $HO_2 + NO \rightarrow OH + NO_2$, (b) $\Delta\beta_{H_2O}[O_3]_{2000s}$ in the FC (ppbv/day/decade). β_{H_2O} is the loss rate due to the reaction of $O(^1D) + H_2O \rightarrow 2OH$. The shaded regions show a significant change at a 98% confidence level. Solid red line is the tropopause height in the simulations for the 2000s, and dashed red line is the tropopause height in the simulations for the 2100s.

km) to test the impact of increased horizontal resolution on the future change in ozone through transport apart from chemistry.

The model predicts an increase in global stratospheric ozone burden by 0.24 $\pm$ 0.01%/decade in the medium resolution simulation, and by 0.29 $\pm$ 0.01%/decade in the high resolution simulation. The predicted changes in annual and zonal mean ozone show a decrease by 20 ppbv/decade in the tropical lower stratosphere, and an increase by 20 ppbv/decade in the extratropical lower stratosphere. However, the MTT predicts a decrease in ozone in the lower stratosphere over the Arctic (5–10 ppbv/decade). This result is opposite to that of CMIP5 models shown in Eyring et al. [2013]. In particular, we must interpret the ozone change there with some caution, because our model simulates the decrease in ozone there in contradiction to the result of CMIP5 models. The global tropospheric ozone burden is reduced by 0.82 $\pm$ 0.04%/decade in the medium resolution simulation, and by 0.76 $\pm$ 0.04 %/decade in the high resolution simulation. A reduction of tropospheric ozone concentration is typically 0.8 ppbv/decade in the free troposphere over the northern midlatitudes. The changes in global burden of stratospheric and tropospheric ozone in the medium and high resolution simulations are within the ranges of change.

To elucidate the processes determining the future change in ozone, we investigate the individual impacts of transport and chemistry on the ozone change using the sensitivity simulation with the

2100s transport field and the 2000s chemical field. The change in global stratospheric ozone burden is controlled by chemical process. Chemical process also reduces the global burden of tropospheric ozone by 1.07%/decade. In the stratosphere, the reactions involving ClO_x and BrO_x largely contribute to the total change in production (P) and loss rate (β), suggesting that the reduction of ODSs is the most important forcing in the stratosphere. In the troposphere, the total change in P and β is respectively influenced by the reaction of HO_2+NO and by the reaction of $O(^1D)$+H_2O. This suggests that both the reduced emissions of tropospheric ozone precursors and climate change have a significant impact on the change in tropospheric ozone because of chemistry.

Transport process also has a non-negligible impact on the future change in tropospheric ozone. In contrast to the impact of chemical process, transport process increases the global burden of tropospheric ozone by 0.25%/decade. The increase attributable to transport is comparably supported by ozone of both stratospheric-origin and tropospheric-origin. This suggests not only that the increased influx of stratospheric ozone causes the increase in global tropospheric ozone burden as shown in the previous studies [Collins et al., 2003; Sudo et al., 2003; Zeng and Pyle, 2003, e.g.], but also that the future change in tropospheric circulation raises the global tropospheric ozone burden. However, it is unclear that what type of tropospheric circulation change is essential for the impact of transport. A further analysis of changes in atmospheric circulation and tracer transport is needed.

Our results are obtained from one model. We need to confirm a robustness of our result by comparing the result of other models (e.g. CMIP5 models). We also examined the respective impacts of transport and chemical process on the future change in stratospheric and tropospheric ozone. However, the result must be interpreted with caution because they are estimated from the simulations conducted only with the medium horizontal resolution. It is desirable to quantify the respective impacts of transport and chemical process using the model with high horizontal resolution.

Chapter 6

General conclusion

Ozone is one of important atmospheric constituents for atmospheric environment and climate. Changes in ozone are caused by a combination of complex transport and chemical processes. The previous studies investigated the individual contributions of transport and chemistry to the diurnal and seasonal cycles of ozone quantitatively, and examined the contributions to the interannual variation in stratospheric ozone. However, the contributions to the long-term changes in stratospheric and tropospheric ozone were hardly examined. This dissertation investigates the respective impacts of transport and chemical processes on the interannual variation in tropospheric ozone and the long-term change in stratospheric and tropospheric ozone. We particularly focus on (1) interannual variation of tropospheric ozone associated with meteorological variability during 1970–2008, (2) long-term future change in ozone during the 2000s and 2100s.

Chapter 3 investigated the interannual variation of global tropospheric ozone associated with meteorological variability, and the respective impacts of transport and chemical processes on it. We focus on five meteorological variability: El Niño Southern Oscillation (ENSO), Indian Ocean Dipole (IOD) variability, interannual variation in Hadley circulation, interannual variation in Asian monsoon circulation, and Arctic Oscillation (AO). In this chapter, we performed the simulation for 39 years from 1970 to 2008 using CHASER global chemical transport model (CTM), in which meteorology was nudged to NCEP/NCAR re-analysis data.

The model shows that the anomaly in tropospheric column ozone (TCO) is positive (1–1.5 DU) in the western Pacific including Indonesia and negative (2.5 DU) in the eastern Pacific in October–November–December (OND) during the positive phase of ENSO. The model exhibits TCO increase (0.5–1.5 DU) in the central to eastern Pacific over the subtropics. During the positive phase of IOD, the model shows TCO increase (1.5–2 DU) in the west of 90°E with a decrease (1–1.5 DU) in the east. Intensified Hadley circulation causes TCO increase (0.8 DU) in North

America in DJF. Intensified Asian monsoon circulation enhances TCO (1.2 DU) in the western Indian Ocean. During the positive phase of AO, TCO is decreased (1 DU) in the high northern latitudes. The interannual variation of TCO is significantly controlled by transport process in the subtropics and the high northern latitudes. However, chemical process also contributes to the TCO interannual variation in the eastern Pacific and the western Indian Ocean over the tropics. TCO variation because of chemical process could be caused by variations in temperature, water vapor, cloud, and lightning associated with meteorological variability.

The contribution of meteorological variability to total interannual variation in global and regional TCO was also quantified in this study. The Empirical Orthogonal Function (EOF) analysis suggests that ENSO is a dominant mode of the variation in global TCO distribution (the contribution rate: 33%) in OND. On regional scale, the other meteorological variability also has non-negligible impacts on the TCO variation. AO explains 72% of the variance in the high northern latitudes in DJF. IOD variability explains 36% of the variance in the equatorial Africa and the tropical western Indian Ocean in OND.

For a reliable future projection, CCM needs to calculate the processes relevant to future change in ozone accurately. In chapter 4, we evaluated the ozone responses to CCM-driven meteorological variability and to a change in the emissions of tropospheric ozone precursors and ODSs, before investigating the future change in ozone. Additionally, we test sensitivities of the ozone changes to increased horizontal resolution through transport apart from chemistry using high-resolution (about $1.1^\circ \times 1.1^\circ$) and medium-resolution (about $2.8^\circ \times 2.8\ ^\circ$) simulations.

To validate the ozone response to CCM-driven meteorological variability, we examined the ENSO-related ozone variation during 2004–2009 with that derived from the MLS/TES satellite instruments. The medium and high resolution simulations show an increase in tropospheric ozone (1 ppbv/K) in the tropical western Pacific, and a decrease (2–20 ppbv/K) in the tropical eastern Pacific. In the midlatitude lower stratosphere over the eastern Pacific, an increase (10–50 ppbv/K) is also found in the simulations. The results generally agree with the variation observed by the MLS/TES instruments.

For the evaluation of the ozone response to a change in the emissions, chapter 4 also evaluated the change in ozone during the 1980s and 2000s in the time-slice simulations. The simulated global and annual mean of total column ozone is decreased by $0.47 \pm 0.16\%$/decade in the medium resolution simulation during the 1980s and 2000s. The simulations underestimate the linear trend observed by TOMS/SBUV instruments ($-1.27 \pm 0.60\%$). The simulations also underestimate the observed trend in ozone (-230 ppbv/decade) in the lower stratosphere over the Antarctic. No

crucial difference is found in the medium and high simulations.

In chapter 5, we performed global simulation of ozone concentration for the 2100s. The simulation predicts an increase in global burden of stratospheric ozone (0.24 $\pm$ 0.01 %/decade in the medium resolution simulation) and a decrease in global burden of tropospheric ozone (0.82 $\pm$ 0.04%/decade in the medium resolution simulation). The change in global stratospheric ozone burden is controlled by stratospheric chemistry rather than transport (i.e. stratospheric circulation). Tropospheric chemistry reduces the global burden of tropospheric ozone by 1.07%/decade. However, transport (i.e. stratosphere–troposphere exchange (STE) and tropospheric circulation) causes an increase in the burden by 0.25%/decade. Transport of ozone of both stratospheric and tropospheric origin comparably contributes the increase, suggesting that not only STE but also tropospheric circulation is important. Additionally we test the sensitivity of the ozone changes to increased horizontal resolution through transport apart from chemistry using medium and high resolution models. No crucial difference is found in the simulations. This suggests that increased horizontal resolution has a minor impact on the ozone changes through transport process.

This study, however, has remaining problems. The model used in this study show some biases. As for tropospheric ozone, the CHASER version 3 model has slight positive biases within 10%, although the MIROC-ESM-CHEM model shows negative biases larger than 20%. This difference is probably caused by the update of radiative transfer scheme (see section 2.2), which highlights a potential bias of the tropospheric photo-chemistry in the model. We need to re-evaluate photolysis rates and/or kinetic chemical reaction velocities. In the lower stratosphere, the MIROC-ESM-CHEM model shows positive biases of ozone larger than 30%. Possible causes of the biases are stratospheric photo-chemistry and the treatment of PSCs in the model. It is necessary to evaluate stratospheric ozone and its related chemical species (e.g. HO_x, NO_y, ClO_y, BrO_y) with observation data, and to address the possible causes.

This study has focused on the interannual variability of tropospheric ozone and the long-term change in the mean state of stratospheric and tropospheric ozone, although we have not investigated interannual variability of tropospheric ozone under a future climate. However, meteorological variability under the future climate can differ among climate models. We need to perform an analysis using multiple models such as Atmospheric Chemistry and Climate Model Intercomparison Project (ACCMIP) and Coupled Model Intercomparison Project Phase 5 (CMIP5). Christensen et al. [2014] reported that future changes in El Niño intensity depend on climate models and do not distinguish from natural modulation, although the future climate change can alter ENSO-related variability of tropospheric ozone through chemical process.

Acknowledgements

I sincerely appreciate Prof. Kengo Sudo at Graduate School of Environment Studies (GSES), Nagoya University for his instruction and encouragement on my doctoral thesis. I also would like to special thanks to Prof. Hiroshi Kanzawa and Prof. Takashi Shibata at GSES, and Prof. Hirohiko Masunaga at Hydrospheric Atmospheric Research Center (HyARC), Nagoya University for reviewing this thesis and giving their informative comments. I would like to thank Dr. Shingo Watanabe at Japan Agency for Marine-Earth Science and Technology (JAMSTEC) for his help in implementing simulation with MIROC-ESM-CHEM model. I am also grateful to Dr. Yoshio Kawatani at JAMSTEC for providing helpful information about high horizontal resolution simulation. Dr. Tatsuya Nagashima at National Institute for Environmental Studies (NIES) is appreciated for his encouragement. The all staff and student of Hydrospheric-Atmospheric Science, Department of Earth and Environmental Studies, GSES are also appreciated for their encouragements. I wish to thank the all member of Sudo-lab. for their many comment and encouragement. I am grateful to Ms. Mami Toyama for her help in various aspects.

For this study, NCEP/NCAR reanalysis from Web site at http://www.esrl.noaa.gov/psd/. The data sets were provided by the NOAA/OAR/ESRL PSD, Boulder, Colorado, USA. TES and MLS instruments data were obtained from Earth Observing System Data and Information System (EOSDIS). I acknowledge the network of WOUDC and SHADOZ for providing ozonesode dataset. TOMS/SBUV MOD was respectively obtained from NASA Goddard Space Flight Center web site (http://acdb-ext.gsfc.nasa.gov/Data_services/merged/index.html). Stratospheric Processes And their Role in Climate (SPARC) data center provides an updated global ozone data set derived from SAGE I+II data, plus polar ozonesondes (http://www.sparc.sunysb.edu/html/RefData.html) The simulations in this thesis were performed using the NIES supercomputer system (NEC SX-8R and SX-9).

References

Akiyoshi, H., T. Sugita, H. Kanzawa, and N. Kawamoto, (2004) : Ozone perturbations in the Arctic summer lower stratosphere as a reflection of NO_X chemistry and planetary scale wave activity. *J. Geophys. Res.*, **109 (D3)**, doi:10.1029/2003JD003632.

Allen, R. J., S. C. Sherwood, J. R. Norris, and C. S. Zender, (2012) : Recent Northern Hemisphere tropical expansion primarily driven by black carbon and tropospheric ozone. *Nature*, **485 (7398)**, 350–354.

Aquila, V., L. D. Oman, R. Stolarski, A. R. Douglass, and P. A. Newman, (2012) : The Response of Ozone and Nitrogen Dioxide to the Eruption of Mt. Pinatubo at Southern and Northern Mid-latitudes. *J. Atmos. Sci.*, **70 (3)**, 894–900, doi:10.1175/JAS-D-12-0143.1.

Avnery, S., D. L. Mauzerall, J. Liu, and L. W. Horowitz, (2011) : Global crop yield reductions due to surface ozone exposure: 1. Year 2000 crop production losses and economic damage. *Atmos. Environ.*, **45 (13)**, 2284 – 2296, doi:http://dx.doi.org/10.1016/j.atmosenv.2010.11.045.

Baldwin, M. P., et al., (2001) : The Quasi-Biennial Oscillation. *Rev. Geophys.*, **39 (2)**, 179–229, doi:10.1029/1999RG000073.

Beer, R. T., T. A. Glavich, and D. M. Rider, (2001) : Tropospheric Emissions Spectrometer for the Earth Observing System Aura satellite. *Appl. Opt.*, **40**, 2356–2367, doi:10.1364/AO.40.002356.

Bowman, K., et al., (2006) : Tropospheric emission spectrometer: retrieval method and error analysis. *Geoscience and Remote Sensing, IEEE Transactions on*, **44 (5)**, 1297–1307, doi: 10.1109/TGRS.2006.871234.

Brasseur, G. P., M. Schultz, C. Granier, M. Saunois, T. Diehl, M. Botzet, E. Roeckner, and S. Walters, (2006) : Impact of Climate Change on the Future Chemical Composition of the Global Troposphere. *J. Clim.*, **19 (16)**, 3932–3951, doi:10.1175/JCLI3832.1.

Butchart, N., A. A. Scaife, J. Austin, S. H. E. Hare, and J. R. Knight, (2003) : Quasi-biennial oscillation in ozone in a coupled chemistry-climate model. *J. Geophys. Res.*, **108 (D15)**, doi: 10.1029/2002JD003004.

Calvo, N., R. R. Garcia, W. J. Randel, and D. R. Marsh, (2010) : Dynamical Mechanism for the Increase in Tropical Upwelling in the Lowermost Tropical Stratosphere during Warm ENSO Events. *J. Atmos. Sci.*, **67 (7)**, 2331–2340, doi:10.1175/2010JAS3433.1.

Chandra, S., J. R. Ziemke, P. K. Bhartia, and R. V. Martin, (2002) : Tropical tropospheric ozone: Implications for dynamics and biomass burning. *J. Geophys. Res.*, **107 (D14)**, ACH 3–1–ACH 3–17, doi:10.1029/2001JD000447.

Chandra, S., J. R. Ziemke, B. N. Duncan, T. L. Diehl, N. J. Livesey, and L. Froidevaux, (2009) : Effects of the 2006 El Niño on tropospheric ozone and carbon monoxide: implications for dynamics and biomass burning. *Atmos. Chem. Phys.*, **9 (13)**, 4239–4249, doi:10.5194/acp-9-4239-2009.

Chandra, S., J. R. Ziemke, W. Min, and W. G. Read, (1998) : Effects of 1997–1998 El Nino on tropospheric ozone and water vapor. *Geophys. Res. Lett.*, **25 (20)**, 3867–3870, doi:10.1029/98GL02695.

Christensen, J. H., et al., (2014) : Climate Phenomena and their Relevance for Future Regional Climate Change. *CLIMATE CHANGE 2013: THE PHYSICAL SCIENCE BASIS*, T. Stocker, Q. Dahe, and G.-K. Plattner, Eds., Cambridge University Press, Cambridge, United Kingdom and New York, NY, USA, chap. 14.

Cionni, I., et al., (2011) : Ozone database in support of CMIP5 simulations: results and corresponding radiative forcing. *Atmos. Chem. Phys.*, **11 (21)**, 11 267–11 292, doi:10.5194/acp-11-11267-2011.

Colella, P. and P. R. Woodward, (1984) : The Piecewise Parabolic Method (PPM) for gas-dynamical simulations. *Journal of Computational Physics*, **54 (1)**, 174–201, doi:http://dx.doi.org/10.1016/0021-9991(84)90143-8.

Collins, W. J., R. G. Derwent, B. Garnier, C. E. Johnson, M. G. Sanderson, and D. S. Stevenson, (2003) : Effect of stratosphere-troposphere exchange on the future tropospheric ozone trend. *J. Geophys. Res.*, **108 (D12)**, doi:10.1029/2002JD002617.

Creilson, J. K., J. Fishman, and A. E. Wozniak, (2005) : Arctic Oscillation–induced variability in satellite-derived tropospheric ozone. *Geophys. Res. Lett.*, **32 (14)**, doi:10.1029/2005GL023016.

Dee, D. P., et al., (2011) : The ERA-Interim reanalysis: configuration and performance of the data assimilation system. *Q. J. R. Meteorol. Soc.*, **137 (656)**, 553–597, doi:10.1002/qj.828.

Doherty, R. M., D. S. Stevenson, C. E. Johnson, W. J. Collins, and M. G. Sanderson, (2006) : Tropospheric ozone and El Nino?Southern Oscillation: Influence of atmospheric dynamics, biomass burning emissions, and future climate change. *J. Geophys. Res.*, **111 (D19)**, doi: 10.1029/2005JD006849.

Doherty, R. M., et al., (2013) : Impacts of climate change on surface ozone and intercontinental ozone pollution: A multi-model study. *J. Geophys. Res.*, **118 (9)**, 3744–3763, doi:10.1002/jgrd. 50266.

Eyring, V., T. Shepherd, and D. Waugh, (2010a) : SPARC report on the evaluation of chemistry-climate models. *SPARC Rep*, **5**.

Eyring, V., et al., (2010b) : Multi-model assessment of stratospheric ozone return dates and ozone recovery in CCMVal-2 models. *Atmos. Chem. Phys.*, **10 (19)**, 9451–9472, doi:10.5194/ acp-10-9451-2010.

Eyring, V., et al., (2013) : Long-term ozone changes and associated climate impacts in CMIP5 simulations. *J. Geophys. Res.*, **118 (10)**, 5029–5060, doi:10.1002/jgrd.50316.

Farman, J. C., B. G. Gardiner, and J. D. Shanklin, (1985) : Large losses of total ozone in Antarctica reveal seasonal ClOx/NOx interaction. *Nature*, **315 (6016)**, 207–210, doi:10.1038/315207a0.

Fiore, A. M., J. J. West, L. W. Horowitz, V. Naik, and M. D. Schwarzkopf, (2008) : Characterizing the tropospheric ozone response to methane emission controls and the benefits to climate and air quality. *J. Geophys. Res.*, **113 (D8)**, doi:10.1029/2007JD009162.

Fiore, A. M., et al., (2009) : Multimodel estimates of intercontinental source-receptor relationships for ozone pollution. *J. Geophys. Res.*, **114 (D4)**, doi:10.1029/2008JD010816.

Fusco, A. C. and J. A. Logan, (2003) : Analysis of 1970–1995 trends in tropospheric ozone at Northern Hemisphere midlatitudes with the GEOS-CHEM model. *J. Geophys. Res.*, **108 (D15)**, doi:10.1029/2002JD002742.

Gillett, N. P., et al., (2011) : Attribution of observed changes in stratospheric ozone and temperature. *Atmos. Chem. Phys.*, **11 (2)**, 599–609, doi:10.5194/acp-11-599-2011.

Guenther, A., et al., (1995) : A global model of natural volatile organic compound emissions. *J. Geophys. Res.*, **100 (D5)**, 8873–8892, doi:10.1029/94JD02950.

Hamid, E. Y., Z.-I. Kawasaki, and R. Mardiana, (2001) : Impact of the 1997–8 El Niño Event on lightning activity over Indonesia. *Geophys. Res. Lett.*, **28 (1)**, 147–150, doi:10.1029/2000GL011374.

Hess, P. and N. Mahowald, (2009) : Interannual variability in hindcasts of atmospheric chemistry: the role of meteorology. *Atmos. Chem. Phys.*, **9 (14)**, 5261–5280, doi:10.5194/acp-9-5261-2009.

Hess, P. G. and J.-F. Lamarque, (2007) : Ozone source attribution and its modulation by the Arctic oscillation during the spring months. *J. Geophys. Res.*, **112 (D11)**, doi:10.1029/2006JD007557.

Houweling, S., F. Dentener, and J. Lelieveld, (1998) : The impact of nonmethane hydrocarbon compounds on tropospheric photochemistry. *J. Geophys. Res.*, **103 (D9)**, 10 673–10 696, doi:10.1029/97JD03582.

Hsu, J., M. J. Prather, and O. Wild, (2005) : Diagnosing the stratosphere-to-troposphere flux of ozone in a chemistry transport model. *J. Geophys. Res.*, **110 (D19)**, doi:10.1029/2005JD006045.

Hudman, R. C., A. R. Russell, L. C. Valin, and R. C. Cohen, (2010) : Interannual variability in soil nitric oxide emissions over the United States as viewed from space. *Atmos. Chem. Phys.*, **10 (20)**, 9943–9952, doi:10.5194/acp-10-9943-2010.

Johnson, C. E., D. S. Stevenson, W. J. Collins, and R. G. Derwent, (2001) : Role of climate feedback on methane and ozone studied with a Coupled Ocean-Atmosphere-Chemistry Model. *Geophys. Res. Lett.*, **28 (9)**, 1723–1726, doi:10.1029/2000GL011996.

Jones, D. B. A., H. R. Schneider, and M. B. McElroy, (1998) : Effects of the quasi-biennial oscillation on the zonally averaged transport of tracers. *J. Geophys. Res.*, **103 (D10)**, 11 235–11 249, doi:10.1029/98JD00682.

K-1 model developers, ., (2004) : K-1 Coupled GCM (MIROC) Description. Tech. rep., Center for Climate System Research (Univ. of Tokyo), National Institute for Environmental Studies, and Frontier Research Center for Global Change. URL `http://ccsr.aori.u-tokyo.ac.jp/~hasumi/miroc_description.pdf`.

Kalnay, M., E.and Kanamitsu, et al., (1996) : The NCEP/NCAR 40-Year Reanalysis Project. *Bulletin of the American Meteorological Society*, **77 (3)**, 437–471, doi:10.1175/1520-0477(1996)077⟨0437:TNYRP⟩2.0.CO;2.

Kang, S. M., L. M. Polvani, J. C. Fyfe, and M. Sigmond, (2011) : Impact of Polar Ozone Depletion on Subtropical Precipitation. *Science*, **332 (6032)**, 951–954, doi:10.1126/science.1202131, `http://www.sciencemag.org/content/332/6032/951.full.pdf`.

Kawase, H., T. Nagashima, K. Sudo, and T. Nozawa, (2011) : Future changes in tropospheric ozone under Representative Concentration Pathways (RCPs). *Geophys. Res. Lett.*, **38 (5)**, doi:10.1029/2010GL046402.

Koumoutsaris, S., I. Bey, S. Generoso, and V. Thouret, (2008) : Influence of El Niño–Southern Oscillation on the interannual variability of tropospheric ozone in the northern midlatitudes. *J. Geophys. Res.*, **113 (D19)**, doi:10.1029/2007JD009753.

Kulawik, S. S., et al., (2006) : Implementation of cloud retrievals for Tropospheric Emission Spectrometer (TES) atmospheric retrievals: part 1. Description and characterization of errors on trace gas retrievals. *J. Geophys. Res.*, **111 (D24)**, doi:10.1029/2005JD006733.

Kurokawa, J., T. Ohara, I. Uno, M. Hayasaki, and H. Tanimoto, (2009) : Influence of meteorological variability on interannual variations of springtime boundary layer ozone over Japan during 1981–2005. *Atmos. Chem. Phys.*, **9 (17)**, 6287–6304, doi:10.5194/acp-9-6287-2009.

Lamarque, J.-F. and P. G. Hess, (2004) : Arctic Oscillation modulation of the Northern Hemisphere spring tropospheric ozone. *Geophys. Res. Lett.*, **31 (6)**, doi:10.1029/2003GL019116.

Lamarque, J.-F., et al., (2010) : Historical (1850–2000) gridded anthropogenic and biomass burning emissions of reactive gases and aerosols: methodology and application. *Atmos. Chem. Phys.*, **10 (15)**, 7017–7039, doi:10.5194/acp-10-7017-2010.

Lamarque, J.-F., et al., (2013) : The Atmospheric Chemistry and Climate Model Intercomparison Project (ACCMIP): overview and description of models, simulations and climate diagnostics. *Geoscientific Model Development*, **6 (1)**, 179–206, doi:10.5194/gmd-6-179-2013.

Lang, C., et al., (2012) : The impact of greenhouse gases on past changes in tropospheric ozone. *J. Geophys. Res.*, **117 (D23)**, doi:10.1029/2012JD018293.

Langford, A. O., T. J. O'Leary, C. D. Masters, K. C. Aikin, and M. H. Proffitt, (1998) : Modulation of middle and upper tropospheric ozone at northern midlatitudes by the El Niño/Southern Oscillation. *Geophys. Res. Lett.*, **25 (14)**, 2667–2670, doi:10.1029/98GL01909.

Li, F., R. S. Stolarski, and P. A. Newman, (2009) : Stratospheric ozone in the post-CFC era. *Atmos. Chem. Phys.*, **9 (6)**, 2207–2213, doi:10.5194/acp-9-2207-2009.

Li, J., P. Pochanart, Z. Wang, Y. Liu, K. Yamaji, M. Takigawa, Y. Kanaya, and H. Akimoto, (2008) : Impact of Chemical Production and Transport on Summertime Diurnal Ozone Behavior at a Mountainous Site in North China Plain. *SOLA*, **4**, 121–124.

Li, J., Z. Wang, H. Akimoto, C. Gao, P. Pochanart, and X. Wang, (2007) : Modeling study of ozone seasonal cycle in lower troposphere over east Asia. *J. Geophys. Res.*, **112 (D22)**, doi: 10.1029/2006JD008209.

Lin, S.-J. and R. B. Rood, (1996) : Multidimensional Flux-Form Semi-Lagrangian Transport Schemes. *Monthly Weather Review*, **124 (9)**, 2046–2070, doi:10.1175/1520-0493(1996) 124⟨2046:MFFSLT⟩2.0.CO;2.

Liu, J. J., D. B. A. Jones, S. Zhang, and J. Kar, (2011) : Influence of interannual variations in transport on summertime abundances of ozone over the Middle East. *J. Geophys. Res.*, **116 (D20)**, doi:10.1029/2011JD016188.

Livesey, N. J., et al., (2011) : Earth Observing System (EOS) Aura Micro-wave Limb Sounder (MLS) Version 3.3 Level 2 data quality and description document. Tech. rep., Jet Propulsion Laboratory California Institute of Technology, 162 pp., Pasadena, California.

Masui, T., et al., (2011) : An emission pathway for stabilization at 6 Wm^{-2} radiative forcing. *Climatic Change*, **109 (1-2)**, 59–76, doi:10.1007/s10584-011-0150-5.

McFarlane, N. A., (1987) : The Effect of Orographically Excited Gravity Wave Drag on the General Circulation of the Lower Stratosphere and Troposphere. *J. Atmos. Sci.*, **44 (14)**, 1775–1800, doi: 10.1175/1520-0469(1987)044⟨1775:TEOOEG⟩2.0.CO;2.

Meinshausen, M., et al., (2011) : The RCP greenhouse gas concentrations and their extensions from 1765 to 2300. *Climatic Change*, **109 (1-2)**, 213–241, doi:10.1007/s10584-011-0156-z.

Miyazaki, K. and T. Iwasaki, (2005) : Diagnosis of Meridional Ozone Transport Based on Mass-Weighted Isentropic Zonal Means. *J. Atmos. Sci.*, **62 (4)**, 1192–1208, doi:10.1175/JAS3394.1.

Miyazaki, K., T. Iwasaki, K. Shibata, and M. Deushi, (2005) : Roles of transport in the seasonal variation of the total ozone amount. *J. Geophys. Res.*, **110 (D18)**, doi:10.1029/2005JD005900.

Murray, L. T., J. A. Logan, and D. J. Jacob, (2013) : Interannual variability in tropical tropospheric ozone and OH: The role of lightning. *J. Geophys. Res.*, doi:10.1002/jgrd.50857.

Myhre, G., et al., (2014) : Anthropogenic and Natural Radiative Forcing. *CLIMATE CHANGE 2013: THE PHYSICAL SCIENCE BASIS*, T. Stocker, Q. Dahe, and G.-K. Plattner, Eds., Cambridge University Press, Cambridge, United Kingdom and New York, NY, USA, chap. 8.

Nagashima, T., T. Ohara, K. Sudo, and H. Akimoto, (2010) : The relative importance of various source regions on East Asian surface ozone. *Atmos. Chem. Phys.*, **10 (22)**, 11 305–11 322, doi: 10.5194/acp-10-11305-2010.

Nagashima, T., M. Takahashi, M. Takigawa, and H. Akiyoshi, (2002) : Future development of the ozone layer calculated by a general circulation model with fully interactive chemistry. *Geophys. Res. Lett.*, **29 (8)**, 3–1–3–4, doi:10.1029/2001GL014026.

Naik, V., et al., (2013) : Preindustrial to present-day changes in tropospheric hydroxyl radical and methane lifetime from the Atmospheric Chemistry and Climate Model Intercomparison Project (ACCMIP). *Atmos. Chem. Phys.*, **13 (10)**, 5277–5298, doi:10.5194/acp-13-5277-2013.

Nassar, R., J. A. Logan, I. A. Megretskaia, L. T. Murray, L. Zhang, and D. B. A. Jones, (2009) : Analysis of tropical tropospheric ozone, carbon monoxide, and water vapor during the 2006 El Niño using TES observations and the GEOS-Chem model. *J. Geophys. Res.*, **114 (D17)**, doi: 10.1029/2009JD011760.

Nassar, R., et al., (2008) : Validation of Tropospheric Emission Spectrometer (TES) nadir ozone profiles using ozonesonde measurements. *J. Geophys. Res.*, **113 (D15)**, doi:10.1029/ 2007JD008819.

Nozawa, T., T. Nagashima, T. Ogura, T. Yokohata, N. Okada, and H. Shiogama, (2007) : Climate change simulations with a coupled ocean–atmosphere GCM called the Model for Interdisciplinary Research on Climate: MIROC. Tech. Rep. 12, Center for Global Environmental Research, National Institude for Environmental Studies. URL `http://www.cger.nies.go.jp/publications/report/i073/I073.pdf`.

Olivier, J. G. J., J. A. van Aardenne, F. Detener, L. Ganzeveld, and J. A. H. W. Peters, (2005) : *Recent trend in global greenhouse gas emission: Regional trends and spatial distribution of key sources, in Non-CO2 Greenhouse Gases (NCGG-4)*. Millpress, Rotterdam, Netherlands., 325–330 pp.

Oltmans, S., et al., (2006) : Long-term changes in tropospheric ozone. *Atmos. Environ.*, **40 (17)**, 3156–3173, doi:http://dx.doi.org/10.1016/j.atmosenv.2006.01.029.

Oman, L. D., A. R. Douglass, J. R. Ziemke, J. M. Rodriguez, D. W. Waugh, and J. E. Nielsen, (2013) : The ozone response to ENSO in Aura satellite measurements and a chemistry-climate simulation. *J. Geophys. Res.*, **118 (2)**, 965–976, doi:10.1029/2012JD018546.

Oman, L. D., J. R. Ziemke, A. R. Douglass, D. W. Waugh, C. Lang, J. M. Rodriguez, and J. E. Nielsen, (2011) : The response of tropical tropospheric ozone to ENSO. *Geophys. Res. Lett.*, **38 (13)**, doi:10.1029/2011GL047865.

Parrish, D. D., et al., (2012) : Long-term changes in lower tropospheric baseline ozone concentrations at northern mid-latitudes. *Atmos. Chem. Phys.*, **12 (23)**, 11 485–11 504, doi:10.5194/acp-12-11485-2012.

Peters, W., M. Krol, F. Dentener, and J. Lelieveld, (2001) : Identification of an El Niño-Southern Oscillation signal in a multiyear global simulation of tropospheric ozone. *J. Geophys. Res.*, **106 (D10)**, 10 389–10 402, doi:10.1029/2000JD900658.

Pozzoli, L., G. Janssens-Maenhout, T. Diehl, I. Bey, M. G. Schultz, J. Feichter, E. Vignati, and F. Dentener, (2011) : Re-analysis of tropospheric sulfate aerosol and ozone for the period 1980–2005 using the aerosol-chemistry-climate model ECHAM5-HAMMOZ. *Atmos. Chem. Phys.*, **11 (18)**, 9563–9594, doi:10.5194/acp-11-9563-2011.

Price, C. and D. Rind, (1992) : A simple lightning parameterization for calculating global lightning distributions. *J. Geophys. Res.*, **97 (D9)**, 9919–9933, doi:10.1029/92JD00719.

Randel, W. J., R. R. Garcia, N. Calvo, and D. Marsh, (2009) : ENSO influence on zonal mean temperature and ozone in the tropical lower stratosphere. *Geophys. Res. Lett.*, **36 (15)**, doi:10.1029/2009GL039343.

Randel, W. J. and A. M. Thompson, (2011) : Interannual variability and trends in tropical ozone derived from SAGE II satellite data and SHADOZ ozonesondes. *J. Geophys. Res.*, **116 (D7)**, doi:10.1029/2010JD015195.

Randel, W. J. and F. Wu, (1996) : Isolation of the Ozone QBO in SAGE II Data by Singular-Value Decomposition. *J. Atmos. Sci.*, **53 (17)**, 2546–2559, doi:10.1175/1520-0469(1996)053⟨2546:IOTOQI⟩2.0.CO;2.

Randel, W. J. and F. Wu, (2007) : A stratospheric ozone profile data set for 1979–2005: Variability, trends, and comparisons with column ozone data. *J. Geophys. Res.*, **112 (D6)**, doi: 10.1029/2006JD007339.

Randel, W. J., F. Wu, J. M. Russell, J. W. Waters, and L. Froidevaux, (1995) : Ozone and temperature changes in the stratosphere following the eruption of Mount Pinatubo. *J. Geophys. Res.*, **100 (D8)**, 16 753–16 764, doi:10.1029/95JD01001.

Randel, W. J., F. Wu, and R. Stolarski, (2002) : Changes in Column Ozone Correlated with the Stratospheric EP Flux. *Journal of the Meteorological Society of Japan.*, **80 (4B)**, 849–862.

Ravishankara, A. R., J. S. Daniel, and R. W. Portmann, (2009) : Nitrous Oxide (N2O): The Dominant Ozone-Depleting Substance Emitted in the 21st Century. *Science*, **326 (5949)**, 123–125, doi:10.1126/science.1176985, `http://www.sciencemag.org/content/326/5949/123.full.pdf`.

Rayner, N. A., D. E. Parker, E. B. Horton, C. K. Folland, L. V. Alexander, D. P. Rowell, E. C. Kent, and A. Kaplan, (2003) : Global analyses of sea surface temperature, sea ice, and night marine air temperature since the late nineteenth century. *J. Geophys. Res.*, **108 (D14)**, doi:10.1029/2002JD002670.

Revell, L. E., G. E. Bodeker, P. E. Huck, B. E. Williamson, and E. Rozanov, (2012) : The sensitivity of stratospheric ozone changes through the 21st century to N_2O and CH_4. *Atmos. Chem. Phys.*, **12 (23)**, 11 309–11 317, doi:10.5194/acp-12-11309-2012.

Rodgers, C. D., (2000) : *Inverse methods for atmospheric sounding: Theory and Practice*. World Scentic, London, doi:10.1142/9789812813718.

Roelofs, G.-J. and J. Lelieveld, (2000) : Tropospheric ozone simulation with a chemistry-general circulation model: Influence of higher hydrocarbon chemistry. *J. Geophys. Res.*, **105 (D18)**, 22 697–22 712, doi:10.1029/2000JD900316.

Saji, N., B. N. Goswami, P. Vinayachandran, and T. Yamagata, (1999) : A dipole mode in the tropical Indian Ocean. *Nature*, **401 (6751)**, 360–363.

Sakazaki, T., et al., (2013) : Diurnal ozone variations in the stratosphere revealed in observations from the Superconducting Submillimeter-Wave Limb-Emission Sounder (SMILES) on board the International Space Station (ISS). *J. Geophys. Res.*, **118 (7)**, 2991–3006, doi:10.1002/jgrd.50220.

Sekiguchi, M. and T. Nakajima, (2008) : A k-distribution-based radiation code and its computational optimization for an atmospheric general circulation model. *Journal of Quantitative Spectroscopy and Radiative Transfer*, **109 (17–18)**, 2779–2793, doi:http://dx.doi.org/10.1016/j.jqsrt.2008.07.013.

Sekiya, T. and K. Sudo, (2012) : Role of meteorological variability in global tropospheric ozone during 1970–2008. *J. Geophys. Res.*, **117 (D18)**, doi:10.1029/2012JD018054.

Shapiro, M. A., H. Wernli, N. A. Bond, and R. Langland, (2001) : The influence of the 1997–99 El Niño Southern Oscillation on extratropical baroclinic life cycles over the eastern North Pacific. *Q. J. R. Meteorol. Soc.*, **127 (572)**, 331–342, doi:10.1002/qj.49712757205.

Shepherd, T. G. and C. McLandress, (2011) : A Robust Mechanism for Strengthening of the Brewer–Dobson Circulation in Response to Climate Change: Critical-Layer Control of Subtropical Wave Breaking. *J. Atmos. Sci.*, **68 (4)**, 784–797, doi:10.1175/2010JAS3608.1.

Son, S.-W., et al., (2008) : The impact of stratospheric ozone recovery on the Southern Hemisphere westerly jet. *Science*, **320 (5882)**, 1486–1489, doi:10.1126/science.1155939.

Spiegel, M. R., (1988) : *Schaum's Outline Series: Theory and Problems of Statistics, 2nd ed.* McGraw-Hill, 504 pp.

Stevenson, D. S., et al., (2006) : Multimodel ensemble simulations of present-day and near-future tropospheric ozone. *J. Geophys. Res.*, **111 (D8)**, doi:10.1029/2005JD006338.

Stevenson, D. S., et al., (2013) : Tropospheric ozone changes, radiative forcing and attribution to emissions in the Atmospheric Chemistry and Climate Model Intercomparison Project (ACCMIP). *Atmos. Chem. Phys.*, **13 (6)**, 3063–3085, doi:10.5194/acp-13-3063-2013.

Stolarski, R. S. and S. M. Frith, (2006) : Search for evidence of trend slow-down in the long-term TOMS/SBUV total ozone data record: the importance of instrument drift uncertainty. *Atmos. Chem. Phys.*, **6 (12)**, 4057–4065, doi:10.5194/acp-6-4057-2006.

Sudo, K. and H. Akimoto, (2007) : Global source attribution of tropospheric ozone: Long-range transport from various source regions. *J. Geophys. Res.*, **112 (D12)**, doi:10.1029/2006JD007992.

Sudo, K. and M. Takahashi, (2001) : Simulation of tropospheric ozone changes during 1997–1998 El Niño: Meteorological impact on tropospheric photochemistry. *Geophys. Res. Lett.*, **28 (21)**, 4091–4094, doi:10.1029/2001GL013335.

Sudo, K., M. Takahashi, and H. Akimoto, (2003) : Future changes in stratosphere-troposphere exchange and their impacts on future tropospheric ozone simulations. *Geophys. Res. Lett.*, **30 (24)**, doi:10.1029/2003GL018526.

Sudo, K., M. Takahashi, J. Kurokawa, and H. Akimoto, (2002) : CHASER: A global chemical model of the troposphere 1. Model description. *J. Geophys. Res.*, **107 (D17)**, ACH 7–1–ACH 7–20, doi:10.1029/2001JD001113.

Takemura, T., M. Egashira, K. Matsuzawa, H. Ichijo, R. O'ishi, and A. Abe-Ouchi, (2009) : A simulation of the global distribution and radiative forcing of soil dust aerosols at the Last Glacial Maximum. *Atmos. Chem. Phys.*, **9 (9)**, 3061–3073, doi:10.5194/acp-9-3061-2009.

Takemura, T., T. Nakajima, B. N. Dubovik, Olegand Holben, and S. Kinne, (2002) : Single-Scattering Albedo and Radiative Forcing of Various Aerosol Species with a Global Three-Dimensional Model. *J. Clim.*, **15 (4)**, 333–352, doi:10.1175/1520-0442(2002)015⟨0333:SSAARF⟩2.0.CO;2.

Takemura, T., T. Nozawa, S. Emori, T. Y. Nakajima, and T. Nakajima, (2005) : Simulation of climate response to aerosol direct and indirect effects with aerosol transport-radiation model. *J. Geophys. Res.*, **110 (D2)**, doi:10.1029/2004JD005029.

Takemura, T., H. Okamoto, Y. Maruyama, A. Numaguti, A. Higurashi, and T. Nakajima, (2000) : Global three-dimensional simulation of aerosol optical thickness distribution of various origins. *J. Geophys. Res.*, **105 (D14)**, 17 853–17 873, doi:10.1029/2000JD900265.

Takigawa, M., M. Takahashi, and H. Akiyoshi, (1999) : Simulation of ozone and other chemical species using a Center for Climate System Research/National Institute for Environmental Studies atmospheric GCM with coupled stratospheric chemistry. *J. Geophys. Res.*, **104 (D11)**, 14 003–14 018, doi:10.1029/1998JD100105.

Tanaka, H. L., N. Ishizaki, and A. Kitoh, (2004) : Trend and interannual variability of Walker, monsoon and Hadley circulations defined by velocity potential in the upper troposphere. *Tellus A*, **56 (3)**, 250–269, doi:10.1111/j.1600-0870.2004.00049.x.

Telford, P., P. Braesicke, O. Morgenstern, and J. Pyle, (2009) : Reassessment of causes of ozone column variability following the eruption of Mount Pinatubo using a nudged CCM. *Atmos. Chem. Phys.*, **9 (13)**, 4251–4260, doi:10.5194/acp-9-4251-2009.

Thompson, A. M., J. C. Witte, H. G. J. Smit, S. J. Oltmans, B. J. Johnson, V. W. J. H. Kirchhoff, and F. J. Schmidlin, (2007) : Southern Hemisphere Additional Ozonesondes (SHADOZ) 1998–2004 tropical ozone climatology: 3. Instrumentation, station-to-station variability, and evaluation with simulated flight profiles. *J. Geophys. Res.*, **112 (D3)**, doi:10.1029/2005JD007042.

Thompson, A. M., et al., (2003a) : Southern Hemisphere Additional Ozonesondes (SHADOZ) 1998–2000 tropical ozone climatology 1. Comparison with Total Ozone Mapping Spectrometer (TOMS) and ground-based measurements. *J. Geophys. Res.*, **108 (D2)**, doi:10.1029/2001JD000967.

Thompson, A. M., et al., (2003b) : Southern Hemisphere Additional Ozonesondes (SHADOZ) 1998–2000 tropical ozone climatology 2. Tropospheric variability and the zonal wave-one. *J. Geophys. Res.*, **108 (D2)**, doi:10.1029/2002JD002241.

Thompson, D. W., et al., (2012) : The mystery of recent stratospheric temperature trends. *Nature*, **491 (7426)**, 692–697.

Tilmes, S., et al., (2012) : Technical Note: Ozonesonde climatology between 1995 and 2011: description, evaluation and applications. *Atmos. Chem. Phys.*, **12 (16)**, 7475–7497, doi:10.5194/acp-12-7475-2012.

van Aardenne, J. A., F. J. Dentener, J. G. J. Olivier, C. G. M. K. Goldewijk, and J. Lelieveld, (2001) : A $1^\circ \times 1^\circ$ resolution data set of historical anthropogenic trace gas emissions for the period 1890–1990. *Global Biogeochem. Cycles*, **15 (4)**, 909–928, doi:10.1029/2000GB001265.

van der Werf, G. R., J. T. Randerson, L. Giglio, G. J. Collatz, P. S. Kasibhatla, and A. F. Arellano Jr., (2006) : Interannual variability in global biomass burning emissions from 1997 to 2004. *Atmos. Chem. Phys.*, **6 (11)**, 3423–3441, doi:10.5194/acp-6-3423-2006.

van Leer, B., (1977) : Towards the ultimate conservative difference scheme. IV. A new approach to numerical convection. *Journal of Computational Physics*, **23 (3)**, 276–299, doi:http://dx.doi.org/10.1016/0021-9991(77)90095-X.

van Noije, T. P. C., H. J. Eskes, M. van Weele, and P. F. J. van Velthoven, (2004) : Implications of the enhanced Brewer-Dobson circulation in European Centre for Medium-Range Weather Forecasts reanalysis ERA-40 for the stratosphere-troposphere exchange of ozone in global chemistry transport models. *J. Geophys. Res.*, **109 (D19)**, doi:10.1029/2004JD004586.

van Vuuren, D. P., et al., (2011) : The representative concentration pathways: an overview. *Climatic Change*, **109 (1-2)**, 5–31, doi:10.1007/s10584-011-0148-z.

Voulgarakis, A., P. Hadjinicolaou, and J. A. Pyle, (2011) : Increases in global tropospheric ozone following an El Niño event: examining stratospheric ozone variability as a potential driver. *Atmospheric Science Letters*, **12 (2)**, 228–232, doi:10.1002/asl.318.

Voulgarakis, A., et al., (2013) : Analysis of present day and future OH and methane lifetime in the ACCMIP simulations. *Atmos. Chem. Phys.*, **13 (5)**, 2563–2587, doi:10.5194/acp-13-2563-2013.

Wallace, J. M., R. L. Panetta, and J. Estberg, (1993) : Representation of the Equatorial Stratospheric Quasi-Biennial Oscillation in EOF Phase Space. *J. Atmos. Sci.*, **50 (12)**, 1751–1762, doi:10.1175/1520-0469(1993)050⟨1751:ROTESQ⟩2.0.CO;2.

Wang, C., (2002) : Atmospheric Circulation Cells Associated with the El Niño–Southern Oscillation. *J. Clim.*, **15 (4)**, 399–419, doi:10.1175/1520-0442(2002)015⟨0399:ACCAWT⟩2.0.CO;2.

Wang, P.-H., J. Fishman, V. L. Harvey, and M. H. Hitchman, (2006) : Southern tropical upper tropospheric zonal ozone wave-1 from SAGE II observations (1985–2002). *J. Geophys. Res.*, **111 (D8)**, doi:10.1029/2005JD006221.

Watanabe, S., K. Sudo, T. Nagashima, T. Takemura, H. Kawase, and T. Nozawa, (2011a) : Future projections of surface UV-B in a changing climate. *J. Geophys. Res.*, **116 (D16)**, doi:10.1029/2011JD015749.

Watanabe, S., et al., (2011b) : MIROC-ESM 2010: model description and basic results of CMIP5-20c3m experiments. *Geoscientific Model Development*, **4 (4)**, 845–872, doi:10.5194/gmd-4-845-2011.

Wesely, M., (1989) : Parameterization of surface resistances to gaseous dry deposition in regional-scale numerical models. *Atmos. Environ.*, **23 (6)**, 1293 – 1304, doi:http://dx.doi.org/10.1016/0004-6981(89)90153-4.

WHO, (2006) : *Air quality guidelines. Global update 2005. Particulate matter, ozone, nitrogen dioxide and sulfur dioxide*. WHO Regional Office for Europe, Copenhagen, Denmark.

Wilks, D., (2006) : *Statistical methods in the atmospheric sciences, 2nd ed.* Elsevier, Amsterdam, 627 pp.

WMO, (2011) : , *Scientific Assessment of Ozone Depletion: 2010*. Global Ozone Research and Monitoring Project-Report No. 52, Geneva, Switzerland, 516 pp. pp.

Worden, J., S. S. Kulawik, M. W. Shephard, S. A. Clough, H. Worden, K. Bowman, and A. Goldman, (2004) : Predicted errors of tropospheric emission spectrometer nadir retrievals from spectral window selection. *J. Geophys. Res.*, **109 (D9)**, doi:10.1029/2004JD004522.

Yamaguchi, K. and A. Noda, (2006) : Global Warming Patterns over the North Pacific: ENSO versus AO. *Journal of the Meteorological Society of Japan.*, **84 (1)**, 221–241.

Young, P. J., et al., (2013) : Pre-industrial to end 21st century projections of tropospheric ozone from the Atmospheric Chemistry and Climate Model Intercomparison Project (ACCMIP). *Atmos. Chem. Phys.*, **13 (4)**, 2063–2090, doi:10.5194/acp-13-2063-2013.

Zeng, G. and J. A. Pyle, (2003) : Changes in tropospheric ozone between 2000 and 2100 modeled in a chemistry-climate model. *Geophys. Res. Lett.*, **30 (7)**, doi:10.1029/2002GL016708.

Zeng, G. and J. A. Pyle, (2005) : Influence of El Niño Southern Oscillation on stratosphere/troposphere exchange and the global tropospheric ozone budget. *Geophys. Res. Lett.*, **32 (1)**, doi:10.1029/2004GL021353.

Zeng, G., J. A. Pyle, and P. J. Young, (2008) : Impact of climate change on tropospheric ozone and its global budgets. *Atmos. Chem. Phys.*, **8 (2)**, 369–387, doi:10.5194/acp-8-369-2008.

Zhang, L., D. J. Jacob, X. Liu, J. A. Logan, K. Chance, A. Eldering, and B. R. Bojkov, (2010) : Intercomparison methods for satellite measurements of atmospheric composition: application to tropospheric ozone from TES and OMI. *Atmos. Chem. Phys.*, **10 (10)**, 4725–4739, doi:10.5194/acp-10-4725-2010.

Zhang, L., et al., (2011) : Impacts of 2006 Indonesian fires and dynamics on tropical upper tropospheric carbon monoxide and ozone. *Atmos. Chem. Phys.*, **11 (21)**, 10 929–10 946, doi:10.5194/acp-11-10929-2011.

Ziemke, J. R. and S. Chandra, (1999) : Seasonal and interannual variabilities in tropical tropospheric ozone. *J. Geophys. Res.*, **104 (D17)**, 21 425–21 442, doi:10.1029/1999JD900277.

Ziemke, J. R., S. Chandra, and P. K. Bhartia, (1998) : Two new methods for deriving tropospheric column ozone from TOMS measurements: Assimilated UARS MLS/HALOE and

convective-cloud differential techniques. *J. Geophys. Res.*, **103 (D17)**, 22 115–22 127, doi: 10.1029/98JD01567.

Ziemke, J. R., S. Chandra, L. D. Oman, and P. K. Bhartia, (2010) : A new ENSO index derived from satellite measurements of column ozone. *Atmos. Chem. Phys.*, **10 (8)**, 3711–3721, doi: 10.5194/acp-10-3711-2010.